Journal of Volcanology and Geothermal Research 322 (2016) 76–104

Contents lists available at ScienceDirect

Journal of Volcanology and Geothermal Research

journal homepage: www.elsevier.com/locate/jvolgeores

Distribution of sulfur aerosol precursors in the SPCZ released by continuous volcanic degassing at Ambrym, Vanuatu

Jérôme Lefèvre [a,*], Christophe Menkes [b], Philipson Bani [c], Patrick Marchesiello [d], Gabriele Curci [e], Georg A. Grell [f], Robert Frouin [g]

[a] LEGOS/MIO, IRD (Institut de Recherche pour le Développement), 98800 Nouméa, New Caledonia
[b] LOCEAN, IRD (Institut de Recherche pour le Développement), 98800 Nouméa, New Caledonia
[c] LMV, IRD (Institut de Recherche pour le Développement), 63000 Clermont-Ferrand, France
[d] LEGOS, IRD (Institut de Recherche pour le Développement), Université de Toulouse, 31400 Toulouse, France
[e] CETEMPS, Department of Physics, University of l'Aquila, L'Aquila, Italy
[f] Earth Systems Research Laboratory of the National Oceanic and Atmospheric Administration (NOAA), Boulder, CO 80305-3337, USA
[g] Scripps Institution of Oceanography, University of California San Diego, La Jolla, CA 92093-0224, USA

ARTICLE INFO

Article history:
Received 20 October 2014
Accepted 14 July 2015
Available online 30 July 2015

Keywords:
Regional aerosol climatology
SPCZ dynamics
SO_2 dispersal
Aerosol modeling
Remote sensing
Volcanic plume impacts

ABSTRACT

The Melanesian Volcanic Arc (MVA) emits about 12 kT d^{-1} of sulfur dioxide (SO_2) to the atmosphere from continuous passive (non-explosive) volcanic degassing, which contributes 20% of the global SO_2 emission from volcanoes. Here we assess, from up-to-date and long-term observations, the SO_2 emission of the Ambrym volcano, one of the dominant volcanoes in the MVA, and we investigate its role as sulfate precursor on the regional distribution of aerosols, using both satellite observations and model results at 1° × 1° spatial resolution from WRF-Chem/GOCART. Without considering aerosol forcing on clouds, our model parameterizations for convection, vertical mixing and cloud properties provide a reliable chemical weather representation, making possible a cross-examination of model solution and observations. This preliminary work enables the identification of biases and limitations affecting both the model (missing sources) and satellite sensors and algorithms (for aerosol detection and classification) and leads to the implementation of improved transport and aerosol processes in the modeling system. On the one hand, the model confirms a 50% underestimation of SO_2 emissions due to satellite swath sampling of the Ozone Monitoring Instrument (OMI), consistent with field studies. The OMI irregular sampling also produces a level of noise that impairs its monitoring capacity during short-term volcanic events. On the other hand, the model reveals a large sensitivity on aerosol composition and Aerosol Optical Depth (AOD) due to choices of both the source function in WRF-Chem and size parameters for sea-salt in FlexAOD, the post-processor used to compute offline the simulated AOD. We then proceed to diagnosing the role of SO_2 volcanic emission in the regional aerosol composition. The model shows that both dynamics and cloud properties associated with the South Pacific Convergence Zone (SPCZ) have a large influence on the oxidation of SO_2 and on the transport pathways of volcanic species across the South Pacific atmosphere. For example, in the tropical cloudy air, the sulfate production in the aqueous phase is very efficient, resulting in the formation of a large cloud of highly scattering sulfate aerosols advected horizontally to Eastern Indonesia, in agreement with the AOD feature captured by MODIS/Aqua, but missed in CALIOP/CALIPSO (lidar) products. Model sensitivity experiments indicate that aerosol re-suspension due to evaporating droplets is a significant pathway for the supply of volcanic sulfur species in the remote marine boundary layer. By strongly modulating the irreversible loss due to wet scavenging, this aerosol process has a similar influence on the sulfur burden as natural emission from volcanoes or biogenic sources like dimethyl sulfate (DMS). The results emphasize the importance of MVA passive degassing and SPCZ dynamics on the aerosol background, and raise questions about potential impacts on the local climate and marine ecosystems.

1. Introduction

Despite the recognized impact of volcanic degassing on the environment and climate (see Robock, 2000 and Oppenheimer et al., 2011 for a review), knowledge of its contribution to greenhouse gases and aerosol burdens in the atmosphere remains incomplete. This is a consequence

* Corresponding author at: IRD, Nouméa Center, BP A5, 98848 Noumea Cedex, New Caledonia.
E-mail address: jerome.lefevre@ird.fr (J. Lefèvre).

http://dx.doi.org/10.1016/j.jvolgeores.2015.07.018
0377-0273/

of large uncertainties in the intensity and chemical composition of volcanic emissions. The most widely used inventory by Andres and Kasgnoc (1998) accounts for a global SO_2 emission rate of 36 kT d^{-1}, but recent advances in the monitoring of gas species from satellite supported by new ground observations suggest to double the SO_2 emission rate (69 kT d^{-1}, Dentener et al., 2006). However, without additional constraint from long-term ground field studies, satellite limitations may strongly affect the estimation of volcanic emission budget, as reported recently in McCormick et al. (2012) and Bani et al. (2012) for volcanoes forming the Melanesian Volcanic Arc. Uncertainties are largely related to the continuous (i.e. passive or non eruptive) volcanic degassing from craters, fissures and fumaroles occurring in silent (or quiet) phase. This source of aerosol precursors quietly and continuously released in the lower troposphere is less spectacular than the abrupt change in stratospheric aerosol burdens induced by explosive events, but the development of more sensitive top-down methods and extensive field studies converge to stress their key role in the global sulfur emission to Earth's atmosphere. For example, in the Melanesian Volcanic Arc, one of the most active volcanic regions on Earth, the release of sulfur gases from passive volcanic degassing is dominant, with a contribution to the regional volcanogenic budget estimated of about 96% (McCormick et al., 2012). At present, uncertainties in volcanic emissions but also in chemical processes and tropospheric transport of volcanic volatiles reduce our capacity to assess their precise role on the Earth's radiation balance and ecosystems.

There is a growing body of literature attesting to the global and regional impact of volcanic degassing on climate, aerosol composition and micro- and macrophysical properties of clouds and climate (see Schmidt et al., 2012, for a review). Changes in microphysical and reflectivity of clouds have been reported in context of tropospheric volcanic plumes too (Gassó, 2008; Yuan et al., 2011 and Ebmeier et al., 2014). Modeling studies suggest that up to 40% of the global tropospheric sulfate aerosols burden may originate from volcanoes (Graf et al., 1997). Despite difficulties in estimating the radiative impact of tropospheric aerosols in current model simulations (Haywood and Boucher, 2000), sulfur species passively released from volcanoes in the troposphere are believed to impact the Earth's radiation balance significantly (Graf et al., 1997; Schmidt et al., 2012). Since sulfate aerosol particles have sizes similar to visible wavelengths, i.e., a typical effective radius (r_e) of 0.2 μm, and since their single-scattering albedo is equal to 1 (i.e. no absorption), they strongly backscatter (solar) shortwave radiation. Thus, due to light scattering, this aerosol type induces a cooling of the atmosphere, called the Direct Radiative Effect (DRE). Such aerosol forcing explains the significant climatic perturbation after the release of stratospheric sulfate aerosols by explosive volcanic eruptions (Robock, 2000). In addition, sulfate aerosols exert an Aerosol Indirect Effect (AIE). By increasing the Cloud Condensation Nuclei (CCN) population, these water soluble aerosols have the capacity to affect cloud microphysics and radiative forcing (the "first indirect" or "cloud-albedo" effect; Twomey, 1977) and cloud lifetime (referred to as the "second indirect" effect; Albrecht, 1989 and Takemura et al., 2005). Schmidt et al. (2012) have estimated the AIE induced by tropospheric volcanic aerosols for pre-industrial conditions by assuming a −50%/+100% uncertainty range in the observed volcanic degassing flux. Their estimation for volcanic induced cooling for pre-industrial conditions is in the range [−1.56 to −0.77] W m^{-2}. While the volcanic AIE for present-day conditions is now smaller by a factor of two due to change in the aerosol background, the volcanic cloud-mediated cooling is of the same order of magnitude as the present-day anthropogenic cloud-albedo effect evaluated in the range [−1.80 to −0.30] W m^{-2} (Forster et al., 2007). The direct effects induced by volcanic and anthropogenic sulfur emissions are also similar in magnitude, estimated at about −0.15 W m^{-2} and −0.17 W m^{-2} respectively (Graf et al., 1997). These attempts are indicators of the capacity of both volcanic and anthropogenic AIE and DRE to balance global warming induced by greenhouse gases (between [+2.07 and +2.53] W m^{-2}), and they emphasize the need to reduce uncertainties in volcanic sulfur emission and improve our knowledge of their distribution and the processes at work in the atmosphere.

Recent observations in halogen-rich volcanic plumes suggest that continuous volcanic degassing acts as a source of halogen radicals (bromine, BrO and chlorine, ClO) that deplete O_3 (i.e., Bobrowski et al., 2003; Gerlach, 2004; von Glasow et al., 2004). O_3 is a primary source of hydroxyl radicals (OH) and its depletion may change the oxidizing capacity of the troposphere, with consequences on atmospheric chemistry near volcanic arcs (Vance et al., 2010; Boichu et al., 2011). Halogen-rich volcanic plumes may also act as an additional natural source of stratospheric halogen after convective transport, thus exerting a similar role in the natural stratospheric ozone depletion as the one signaled for very short-lived halocarbons emitted from the ocean (Liang et al. 2010). Reactive halogens and SO_2 are also suspected to exert a strong control on the oxidation of trace metals co-emitted in volcanic plumes. For example, using field- and model-based results, Von Glasow (2010) suggested that volcanogenic mercury (Hg) might have larger effects on health and environment than previously thought due to the rapid oxidation of Hg in the plume. Since SO_2 is generally used as a proxy to derive budgets of other volcanic volatiles, including halogens, (e.g., Bani et al., 2009; McCormick et al., 2012), improvement in our knowledge of volcanic SO_2 budget and our capacity to understand their transport pathways may more generally enlighten the potential impact of passive degassing on the atmosphere, climate and Earth's ecosystems.

Recent field studies dedicated to SO_2 emission budget for the Melanesian Volcanic Arc (MVA) confirmed the very strong continuous degassing rate due to the main volcanoes of Papua New-Guinea, the Solomon Islands and the Vanuatu archipelago, representing altogether nearly 20% of global emission (Bani et al., 2012; McCormick et al., 2012). However, since sporadic explosive phases or extreme degassing events (Bani et al., 2009) are not considered, the MVA contribution to global emission may still be easily underestimated. Together with volcanoes of the eastern maritime continent (Southeast Asia), the MVA region forms a sulfur-rich atmosphere, as previously shown in Jones and Christopher (2011). The main objective of our study is to describe aerosol distribution in the SW Pacific, including the MVA and eastern maritime continent. Using recent emission inventories for natural and anthropogenic sources, this work is more specifically dedicated to the role of volcanic passive degassing, aerosol processes and transport pathways in the observed tropospheric aerosol composition.

Our approach relies on numerical atmospheric modeling and satellite observations of SO_2 burden and aerosol properties by OMI (Ozone Monitoring Instrument), CALIOP and MODIS. The model is based on the Weather Research and Forecast (WRF) model coupled with Chemistry (WRF-Chem; Grell et al., 2005) including the aerosol schemes of the Goddard Chemistry Aerosol Radiation and Transport model (GOCART; Chin et al., 2000a,b). In previous studies, WRF has been successfully used to investigate the South Pacific cyclonic activity (Jourdain et al., 2011) and the weather regimes and mesoscale interactions with tropical islands of the same region (Lefèvre et al., 2010). For the present study, model adjustments were needed for improving the representation of aerosol sources and sinks. Some satellite measurement biases are also uncovered by cross-examination of aerosol optical properties.

The paper is organized as follows. In Section 2, we start with preliminary remarks on regional volcanic emissions and atmospheric dynamics. In Section 3, the satellite data and methods used to assess gas and aerosol compositions are presented. In Section 4, we provide a description of the modeling system, including details on the FlexAOD post-processor used to compute offline the aerosol optical depth with recent revisions for aerosol microphysics and optical properties. In Section 5, we evaluate the climate model through its cloud, precipitation and dynamical features that are known to control aerosol lifetimes and distributions, and we describe the adjustment of sea salt source function in the aerosol model. In Section 6, we investigate the influence of Ambrym volcanic degassing on the troposphere composition using satellite

observations and model results. In Section 7, we assess the respective role of sources, transport and sinks, using the model results and a budget equation for sulfur components. Here, we detail the South Pacific Convergence Zone (SPCZ) chemical and transport processes controlling the distribution of sulfur species released from Ambrym. We also conduct sensitivity experiments that provide error bars associated with uncertainties in model treatment of sources and removal processes. In the last section, we discuss the potential implications of passive volcanic degassing for the chemistry and climate of tropical regions and propose arguments to improve aerosol modeling.

2. Preliminaries

The Vanuatu volcanic arc, located in the southeastern part of the MVA (Fig. 1, inset), is a remote and pristine fragmented tropical archipelago. The Ambrym volcano was recently identified as the primary source of volcanic volatiles in Vanuatu. Using ground-based UV spectrometers supported by OMI survey, Bani et al. (2012) have characterized the huge and continuous SO_2 degassing of 5.4 kT d^{-1} from Benbows and Marum, two active craters at the summit of Ambrym (16.14°S; 168.0°E and 1270 m). Considering the global SO_2 volcanic emission of 69 kT d^{-1}, Ambrym is considered as one of the largest natural emitters, comparable to Etna. Recent studies have shown that Vanuatu's inhabitants are exposed to sulfur and halogen rich plumes emanating from Ambrym, with consequences on health, food crops and water supplies (Cronin and Sharp, 2002; Allibone et al., 2010). During the sporadic phase of extreme degassing in the 2004/2005 austral summer, Bani et al. (2009) measured prodigious degassing rates of 15–23 kT d^{-1} for SO_2 and 2–4 T d^{-1} for BrO. They suspected that a major release of volcanic volatiles in chemically active volcanic plumes would have a large impact on both the oxidants background and the regional radiative budget. Our investigation is thus focused on Ambrym as a necessary step toward understanding of air and land pollution by volcanic species in the SW Pacific.

2.1. Volcanic degassing inventory in the MVA

The geographic location of the main sources of volcanic SO_2 in the SW Pacific is displayed in Fig. 1 and their emission rate is summarized in Table 1. Emission rates are provided by the AeroCom inventory (Aerosol Comparisons between Observations and Models, Dentener et al., 2006), with the exception of Ambrym whose emission rate is taken from Bani et al. (2012). Table 1 indicates that continuous degassing from volcanoes in the MVA and eastern maritime continent may account for 17.2 kT d^{-1}. Compared with the original AeroCom budget of 14.05 kT d^{-1}, the present increase of 22.5% due to updated Vanuatu emissions is significant. Note that the total MVA SO_2 emission budget for non-eruptive activity is greater than the total anthropogenic sources from industrial countries in the region, including Indonesia, Philippines, Australia and New-Zealand. Furthermore, in the region, SO_2 degassing from volcanoes also exceeds the natural SO_2 emission resulting from oxidation of DiMethyl Sulfide (DMS), a volatile biogenic sulfur compound emitted from marine organisms, known to exert forcing on climate and atmospheric chemistry (Ayers and Gillett, 2000). However, like volcanic emission, this SO_2 source is subject to large uncertainties, depending on the choice of air–sea exchange parameterization and climatological data (Boucher et al., 2003; Faloona, 2009; Lana et al., 2011).

2.2. The South Pacific Convergence Zone

A detailed description of the climate features and large-scale flow patterns in the South Pacific is given in Fuelberg et al. (1999) in the context of the Pacific Exploratory Mission in the Tropics (PEM-Tropics A and B), while Fenn et al. (1999) discussed the aerosol (and Ozone) distributions in the SPCZ in relation with the convective activity during PEM-Tropics A. Continuous degassing from MVA volcanoes occurs in the SPCZ, the largest convective area of the South Pacific. The SPCZ is associated with deep convective clusters and intense surface precipitation (Fig. 1). This major regional atmospheric feature plays a key role in the Earth climate system (Cai et al., 2012). It also affects aerosol processes and makes aerosol observations difficult. More specifically, thick clouds in the SPCZ may strongly impair the retrieval of volcanic emission by interfering with satellite sensing of trace gases and enhance the rate of SO_2 depletion by oxidation and scavenging (McCormick et al., 2012). Moreover, the dispersion and vertical motion of volcanic volatiles in plumes due to convection and turbulent mixing introduce additional errors in the retrieval of emission budgets. Clearly, the MVA environment makes a challenge for accurate measurements of volcanic species. The modeling of meteorological and aerosol processes is equally difficult (Textor et al., 2007). Matthijsen et al. (1997) have shown that the SO_2 lifetime is strongly dependent on the model representation of chemical weather, through accurate simulation of cloud macrophysical properties. In the tropics, the fate of passive tracers is also very sensitive to the model treatment of turbulent mixing by convective transport (Hoyle et al., 2011). For reliable results, these authors further recommend to accurately model both the location of convective transport and the spatial patterns of pollutant emission. Therefore, particular attention has been given in this study to provide accurate volcanic sources, including fluxes and plume heights, and representation of meteorological parameters involved in chemistry, transport and removal processes. Such preconditions are not systematically met in global

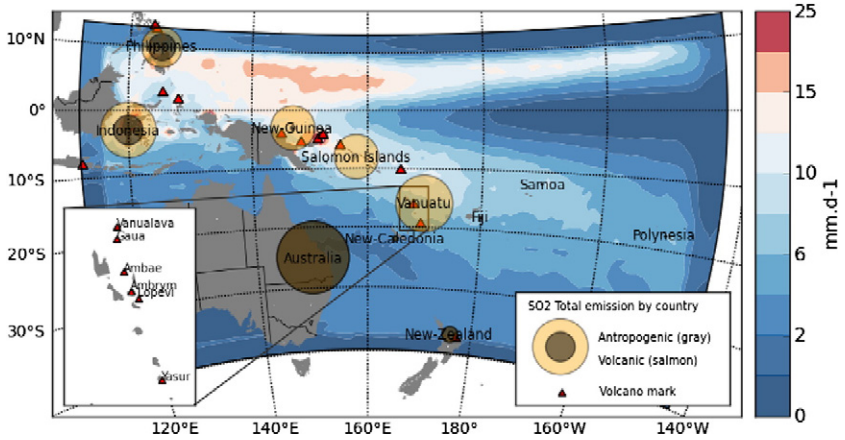

Fig. 1. Model domain and 3-year (2006–2008) mean precipitation (mm d^{-1}) emphasizing the model representation of convergence zones (SPCZ and ITCZ). The main sources of SO_2 are symbolized as circles, with size according to emission rates of volcanic degassing (salmon) and anthropogenic sources (gray). SO_2 emissions by country and origin are given in Table 1. The inset zooms in on the Vanuatu island arc, including the Ambrym volcano characterized by continuous SO_2 degassing.

Table 1
Daily emission for natural and anthropogenic SO_2 and yearly emission for carbonaceous aerosol specified in the regional model. Anthropogenic emissions are constrained using the EDGAR database, while non-erupting volcanic emissions are given by the AeroCom database, after revision using the last volcanic degassing budget for Vanuatu (Bani et al., 2012). The oceanic biogenic SO_2 (DMS) production is given by our model using various DMS flux schemes and oceanic DMS databases. For information, a global model SO_2 source budget is also given.

	SO_2 emissions [kT(SO_2) d^{-1}]				Carbonaceous emissions [kT(BC) $year^{-1}$]	
	Anthropogenic	Volcanic degassing	Oceanic (DMS)	Biomass burning	Anthropogenic	Biomass burning
Australia	8.8	–			27.1	
New-Zealand (North)	0.4	–			3.3	
Philippines	1.2	1.5			63.2	
Indonesia	1.4	3.7			124.9	
Total	***11.8***	***5.2***			***218.5***	
Pacific island countries *(see details below)*	***0.1***	***12.0***			***2.8***	
New-Caledonia	0.050	–			>0.1	
Fiji	0.009	–			0.3	
Papua New-Guinea[a]	0.037	6.5			2.1	
Polynesia	0.007	–			>0.1	
Solomon Islands	0.002	0.1			0.2	
Samoa	0.003	–			>0.1	
Vanuatu[b]	>0.001	5.4			>0.1	
SW Pacific	***11.9***	***17.2***	***9.2–18.7***[c]	Not specified	***221.3*** *(OC not specified)*	Not specified
Global[d]	*300–530*	*20–80*	*58–153*	*11–16*		

[a] Including Bougainville Island. Source: non-eruptive volcanic emission from the AeroCom database.
[b] Only Ambrym, source Bani et al. (2012). This new rate associated with the largest persistent source, Ambrym, is more than twice the AeroCom estimation for the Vanuatu group (11 volcanoes, total emission: 2.15 ktons(SO_2) d^{-1}, mean [09-2005:10-2008]).
[c] Range of oceanic biogenic SO_2 flux using respectively: the Kettle et al. (1999) oceanic DMS database with flux parameterization of Liss and Merlivat (1986); and the Lana et al. (2011) DMS database with flux parameterization of Nightingale et al. (2000).
[d] SO_2 budget range given by Faloona (2009) using data from Textor et al. (2006).

models with coarse horizontal and vertical resolution or with poor model treatment of aerosol processes interacting with meteorological parameters (Textor et al., 2007) leading to a misrepresentation of the environmental impact of tropospheric volcanic plumes.

3. Satellite data

3.1. Volcanic SO_2 mass burden and emission rate

The Dutch–Finnish OMI sensor, onboard the National Aeronautics and Space Administration (NASA) Aura satellite since July 2004, is an hyperspectral UV/Visible spectrometer dedicated to the daily, contiguous monitoring of SO_2 and other trace gases with a nadir spatial resolution of 13 × 24 km (Levelt et al., 2006; see sensors details in Table 2). The gas detection capability exploits the SO_2 UV absorption feature at 230–330 nm (Krotkov et al., 2006). Improvements in the SO_2 retrieval algorithm and its detection limit of about 0.6 Dobson Units (D.U.) now allow the retrieval of SO_2 emission from both passive volcanic degassing and high eruptive plumes injected into the stratosphere (e.g., Carn et al., 2007; Bani et al., 2012; McCormick et al., 2012). OMI SO_2 Level 2, Version 3 products provide together sensor information, quality flag, cloud radiance fraction and four retrievals of SO_2 Vertical Column Density (VCD). Each OMI SO_2 VCD is given for an a-priori SO_2 vertical profile with distinct center of mass altitude (see Krotkov et al., 2006, for details). The center of mass altitude of lower troposphere (TRL) SO_2 VCD is located at 2.5 km and is used in this study to derive the volcanic SO_2 burden due to Ambrym. The center of mass altitude of TRL VCD is within the range of previous reported plume altitudes (Bani et al., 2012) with a plume top capped by the trade inversion at 2.5–3 km in the region (see Fig. 2 in Lefèvre et al., 2010). Since January 2009 onward, the OMI sensor has suffered from the occurrence of erratic instrumental errors (called "row anomalies"; see McCormick et al., 2012), restricting our study with OMI to the prior period.

For each daily image, the SO_2 burden in a regional box centered on the source of emission is calculated by summing all OMI pixels with SO_2 VCDs above 0.6 DU (labeled with "*fi*" in Eq. (1), "*nofi*" stands for pixel below that limit) after excluding sensor anomalies and pixels with low Sensor Zenith Angle (<70°) and cloud or glint contamination (Bani et al., 2009, 2012). For each OMI pixel above the threshold, the SO_2 mass calculation is performed through Eq. (1) (see Pinardi et al., 2010):

$$Mass_{SO2}[Kg] = \left(VCD_{fi} - mean\left(VCD_{nofi}\right)\right).AirPix_{fi}.\frac{M_{SO2}}{N_A} \quad (1)$$

where M_{SO2} (=64 g/mol) and N_A are the SO_2 molar mass and the Avogadro number respectively, *AirPix* is the pixel area (m^2), and *VCD* is the SO_2 column amount expressed in molecules m^{-2}. The term $mean(VCD_{nofi})$ is computed by averaging all OMI pixels in the regional box with value below 0.6 DU. This value is representative of the SO_2 background contaminated by noise. Later in Section 6.1, Eq. (1) will be used with the model SO_2 VCD outputs to derive the simulated OMI top-down estimate of SO_2 mass burden. Since the model has larger "pixel" cells in comparison with OMI, the simulated sensor detection limit is scaled down to 0.017 DU against 0.6 DU in OMI. That factor of 35 is given by the surface area ratio between model and OMI pixels (105 × 105 km^2 and 13 × 24 km^2, respectively).

Table 2
Description of the satellite sensors and products used in this study.

Sensor/satellite	Operational lifetime, spatial resolution, equatorial crossing time,	Geophysical products	Product/collection	Reference
MODIS/Aqua	Since 7-2002, daily contiguous 2330-km swath 13:30 p.m. LT	Total AOD 550 nm, FC	MOD08_D3, collection 5.1	Remer et al. (2005)
CALIOP/CALIPSO	Since 6-2006 100 m footprint size 13:31 p.m. LT and 1:30 a.m. LT, with a repeat cycle of 16 days (twice a day at 1° spatial resolution)	Aerosol layer altitude, thickness and AOD aerosol subtype total AOD 532 nm cloud optical depth	Level 2 Version 3.0 aerosol layer	Winker et al. (2009)
OMI/Aura	Since 7-2004, daily contiguous 2600 km swath,13 × 24 km (nadir) 1:38 p.m. LT	SO_2 cloud radiance fraction	OMI SO_2 Level 2 Version 3	Torres et al. (2007)

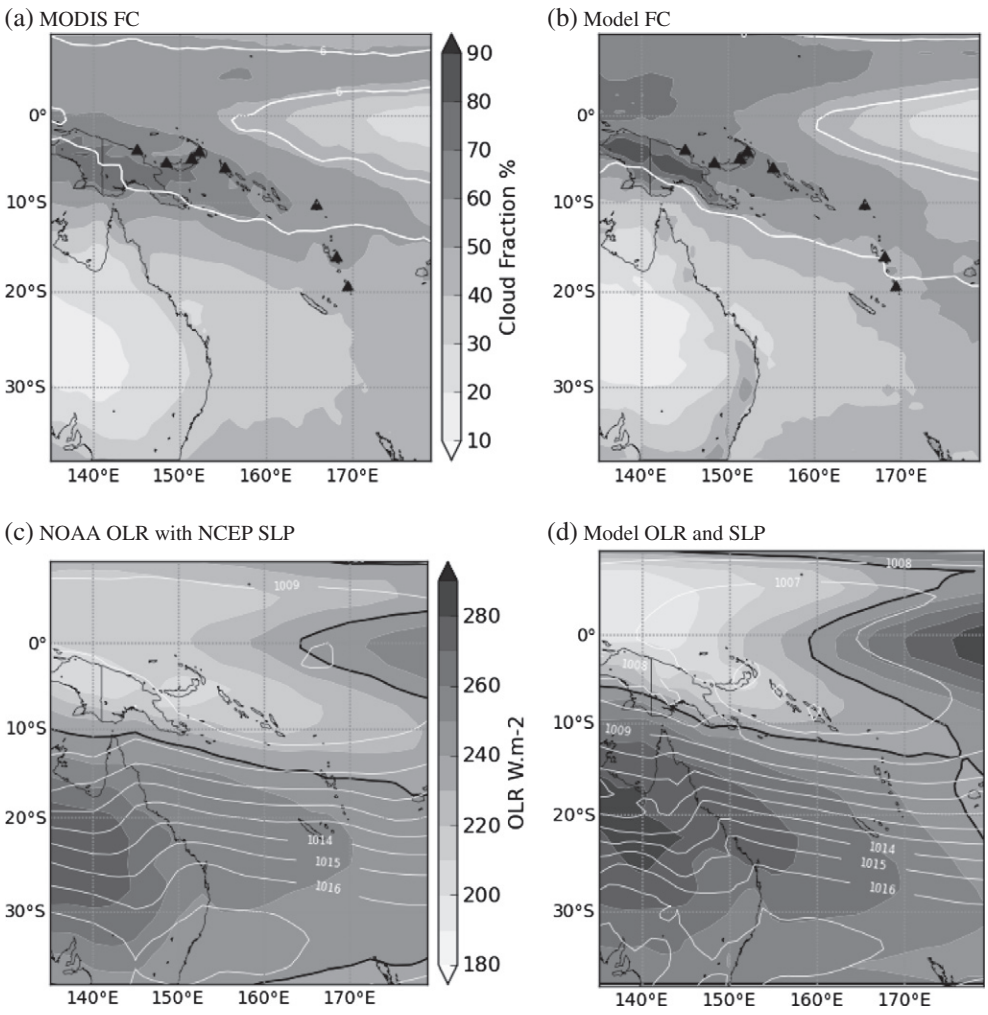

Fig. 2. Mean state (01-Oct-2005 to 01-Oct-2008) of total fractional cloudiness (FC) from (a) Aqua/MODIS and (b) the model; Outgoing Longwave Radiation (OLR) and sea level pressure (SLP) from (c) NOAA (SLP in shades of gray) and NCEP (SLP in white contours) and (d) the model. To highlight regions of heavy convective rainfall, the 6 mm d^{-1} isohyet from AMSRE precipitation and model are displayed in heavy white contour in panels (a) and (b) respectively. From OLR, the 240 W m^{-2} contour is used to outline regions of high cloudiness. The main volcanoes from the Melanesian volcanic arc are also symbolized with triangles.

From Eq. (1), one can derive the SO_2 emission rate Q of the source:

$$Q = \frac{Mass_{SO2}}{t} \quad (2)$$

where t is an estimate of SO_2 lifetime within the plume that varies with the local climate and is accessible through field studies (McCormick et al., 2012). Ground or aircraft based observations close to the source are commonly required to constrain top-down estimates of SO_2 emission rate (Spinei et al., 2010; Bani et al., 2012). In the absence of such observation, estimations are not straightforward. The accuracy of OMI SO_2 burden is not only limited by swath sampling, detection limit and sensor errors but also by cloud contamination, removal and dilution mechanisms occurring in the plume. Moreover, the reported SO_2 lifetimes in volcanic plumes are generally shorter than the delay between successive OMI swaths (<1 d) and strongly rely on the environment (ambient humidity) and oxidizing nature of the plume (Oppenheimer et al., 2011). Clearly, inappropriate SO_2 lifetimes may result in systematic underestimation of SO_2 fluxes (McCormick et al., 2012). To evaluate such error, we compare the simulated volcanic SO_2 burden with the quantity derived from OMI using Eq. (1) applied to Ambrym volcano. Knowing its emission rate and using Eq. (2), we will show how dilution, removal processes, cloud and swath screening combine together to reduce the top-down estimate of SO_2 emission rate.

3.2. Aerosol burden comparisons using AOD

Flying within NASA's A-Train, in concert with Aura/OMI within a 15-min time window, MODIS/Aqua (passive radiometer) and CALIOP/CALIPSO (lidar) probe the aerosol and cloud optical properties of the same air mass. The aerosol Level 3 product (MYD08_D3 Collection 5.1, see Table 2) provides a daily estimation of the total aerosol optical depth (AOD or τ). Referred to as the extinction of solar radiation by aerosols, this quantity integrates the nature of the aerosol (i.e. the aerosol type defined in regard of its absorption and scattering properties) and their respective mass concentration and size, with changes due to hygroscopic growth (see Chin et al., 2002 and details in Appendix B.). MODIS AOD are derived using improved algorithms detailed in Remer et al. (2005). They operate by matching six observed reflectances in the solar spectrum (0.47–2.1 μm) to lookup tables build using a Radiative Transfer Model that simulates spectral reflectance for expected aerosols conditions. Along track MODIS AOD retrievals with a spatial size of 10 × 10 km^2 are binned to provide the daily 1 × 1° AOD dataset in MYD08_D3. To remove cloud artifacts and sun-glint contamination, only 10 × 10 km^2 AOD retrievals having a confidence flag ≥ 1 are considered in this processing. Extensive validations against AERONET observations state that the AOD uncertainty is $\tau_{error} = \pm (0.03 \pm 0.05\tau)$ over the ocean (Remer et al., 2006) and that the product can be used quantitatively for aerosol model validation (e.g., Chin et al., 2002). As a

valuable surrogate for the total aerosol burden, both MODIS and simulated AOD are combined to derive the distribution of aerosol over the SW Pacific, while differences are interpreted in relation with sources and model treatments for aerosol processes.

3.3. Structure of the aerosol composition

The Cloud-Aerosol LIdar with Orthogonal Polarization (CALIOP) provides supplemental details on the structure of the aerosol composition that are overlooked in Visible-IR imagers like MODIS. CALIOP data version 3 products provide six aerosol types classified by the cloud-aerosol discrimination (CAD) algorithm (Liu et al., 2009; Winker et al., 2009). These types are clean marine particles, polluted dust, dust, clean continental, polluted continental and biomass burning particles (or smoke). They are associated with each aerosol layer identified by the CAD along the vertical laser beam, as detailed in Appendix A. CALIOP gives additional information: the vertical profile of the aerosol extinction coefficient ($\sigma_{aer,}$ unit m^{-1}; see Eq. (B.1)) at $\lambda = 532$ nm and the altitude and thickness of the aerosol layer. They are useful in documenting the vertical distribution of aerosols and tracking polluted air masses, like volcanic plumes (e.g., Spinei et al., 2010). The CALIOP $AOD_{\lambda = 532\ nm}$ is calculated by vertically summing for each aerosol layer its specific σ_{aer}.

In this study, the structure of the aerosol composition is given by computing the contribution of each aerosol type to total AOD, both in the model and CALIOP observations. The simulated AOD is computed at $\lambda = 550$ nm to be consistent with MODIS AOD, neglecting the wavelength dependence of AOD between 532 nm and 550 nm (the error is small between 2 and 4%; Kittaka et al., 2011). However, it is worth noting that the definition of aerosol types between CALIOP and GOCART differs. The aerosol type defined in CALIOP represents typical atmospheric mixtures of components as observed by AERONET (Omar et al., 2005; Winker et al., 2009). These components are comprised of dust like substances (DU), carbonaceous component (CC) formed by soot and burnt biomass substances, sea salt (SS) and water soluble aerosols (dominated by sulfate SU and nitrate substances). Therefore, CALIOP σ_{aer} represents the volume-averaged extinction coefficient due to the aerosol mixtures, while GOCART provides single-component effects. This point will be considered in Section 6.2, when comparing model results with satellite observations.

4. The Regional Climate and Chemistry Model: Wrf-Chem/Gocart

4.1. Description of WRF-Chem

Simulations of gas and aerosol concentrations are made with Version 3.3.1 of the WRF-Chem meteorological model (Skamarock et al., 2008) coupled online with chemistry (Grell et al., 2005). The model has multiple choices for gas-phase chemistry and aerosol modules, with some tied to cloud microphysics and radiation modules, allowing investigations of aerosol forcing (e.g. Fast et al., 2006). In the present study, the GOCART sulfur chemistry and aerosol model (Chin et al., 2000a,b) is used to simulate the emission, transport and removal of five major tropospheric aerosol types introduced above (DU, SS, SU and CC composed of Organic Carbon, OC, and Black Carbon, BC) and the chemical transformation of sulfate gas precursors, i.e., DMS, emitted from the marine biological activity, and SO_2, released from anthropogenic and natural sources (e.g., volcanoes). Methane Sulfonic Acid (MSA), a by-product salt from the oxidation of DMS, is also simulated in GOCART. This computationally inexpensive sulfur chemistry and aerosol model is known to deliver global results with good skills (Chin et al., 2000a,b and Textor et al., 2007).

4.2. Model configuration and physical setup

The WRF-Chem model is implemented over the SW Pacific domain between [40°S–13°N] and [112°E–142°W], centered on Vanuatu, with a 1° horizontal spacing. The main difference with our past configurations (Jourdain et al., 2011) is the use of a suite of physical packages adapted from the Community Atmosphere Model version 5 (CAM, Collins et al., 2004). The physics configuration includes the use of the moist turbulence Planetary Boundary Layer (PBL) and shallow convection unified parameterizations from the University of Washington (Bretherton and Park, 2009 and Park and Bretherton, 2009, respectively), the Zhang and McFarlane (1995) convective bulk mass flux scheme for deep convection, the Purdue Lin microphysics scheme (Lin et al., 1983) and the CAM radiation module for both longwave and shortwave radiation (details in Table 3). The physics package and interaction with chemistry are also displayed in Fig. C1. After careful validation (Section 5), we found the selected physics and cloud microphysics package appropriate to our aerosol problem. WRF-Chem is run with the GOCART bulk aerosol model that has no aerosol-cloud and radiation interaction or ozone chemistry. To accurately capture the tropical tropospheric meteorology and chemical processes, the vertical column is discretized into 35 terrain-following σ-levels, with 20 levels below 500 hPa. The model top is fixed at 50 hPa and the surface layer is approximately 15–25 m thick, with a mid-point close to 10 m. According to Hoppel et al. (2005), our surface refinement is sufficient to model the process of generation and sedimentation of sea salt aerosols without applying a correction term. This is an improvement from global models that have coarser vertical resolution in the boundary layer (see Fan and Toon, 2011). Note that a horizontal resolution of 1° is too coarse to capture the wide range of processes associated with mesoscale dynamics, especially around high tropical islands (Lefèvre et al., 2010 and Jourdain et al., 2011, for details) and they are here assumed unimportant to large-scale transports. This assumption should be checked in further studies.

Surface emission, vertical distribution, chemical transformation and scavenging of atmospheric species are strongly dependent on the model representation of regional climate (see Matthijsen et al., 1997; Textor et al., 2006, 2007; Faloona, 2009; George and Wood, 2010). With a grid spacing of 1°, the subgrid vertical motion of species particularly depends on the performance of the convection scheme and treatment of associated tracer transport (Hoyle et al., 2011). A large effort was thus devoted to validate the meteorology, cloud macrophysics, and surface fluxes, conducting diagnostic studies of SPCZ properties, including AMSRE rain, cloud, and water content, MODIS cloud fraction, Outgoing Longwave Radiation from NOAA and scatterometer winds (Section 5).

4.3. Aerosol processes in WRF-Chem/GOCART

Original features of GOCART for aerosol treatments and sulfur chemistry are detailed in Chin et al. (2000a,b and 2002). GOCART is a bulk aerosol model that provides only the total mass within each size

Table 3
Physics parameterization selected in WRF-ARW V3.3.1.

Physical models	Parameterization	Reference
Land-surface model	Unified Noah	Chen and Dudhia (2001)
Oceanic surface layer	Monin–Obukhov scheme	Jiménez et al. (2012)
Microphysics	Purdue Lin (one moment)	Lin et al. (1983)
PBL and shallow convection	UW CAM5 moist turbulence with explicit entrainment at the top of the PBL and shallow convection, unified parameterization	Bretherton and Park (2009) Park and Bretherton (2009)
Deep convection	Zhang–McFarlane	Zhang and McFarlane (1995)
Longwave and shortwave radiation	CAM3 scheme	Community Atmospheric model Version 3 (Collins et al., 2004). *(With cloud fraction computed from* Xu and Randall (1996)*)*

bin. There are five size bins for DU (details in Zhao et al., 2010) and four size bins for SS (details in Appendix B), while others aerosols are simply represented by their total mass. Aerosol processes are implemented through several specific modules in the WRF-Chem/GOCART system (Fig. C1). They include (1) surface emission, with magnitude controlled by meteorology for dust, sea salt and DMS, (2) gravitational sedimentation and dry deposition, (3) vertical turbulent mixing, (4) convective tracer transport, and (5) grid- and sub-grid scale wet deposition. Advection and lateral diffusion of tracers are computed using the monotonic advection scheme implemented in the Advanced Research Weather dynamic core (Wang et al., 2009). Compared with the original features of GOCART (Chin et al., 2000a, 2000b, 2002), successive improvements, including our own modifications and their integration within WRF-Chem, have led to significant changes. In Appendix C and Fig. C1 we give a description of the current modeling system based on WRF-Chem/GOCART and detail the nature of our changes. We also provide details about the major physical processes affecting the tracer fate in Appendix C.

Since the mass flux and altitude reached in deep convective updrafts are quite large in the tropics, we used the vertical transport of tracers from the Zhang and McFarlane convection scheme (see details in Appendix C and Fig. C2). In WRF-Chem current public releases, the tracer redistribution by shallow convection is not implemented within the University of Washington physical suite. Therefore, in this study the lower troposphere transport associated with subgrid-scale shallow convection is discarded (Appendix C). A second limitation is the underestimation of wet scavenging, only represented by grid-scale precipitation, not by convective (subgrid-scale) precipitation. Since large uncertainties remain on the parameterization of convective wet deposition (Textor et al., 2006; Croft et al., 2012), this aerosol process was not included in our setup (Appendix C). Sensitivity to this missing sink process will be addressed in Section 7.3. On the other hand, the grid-scale wet deposition scheme has been made more complex, by implementing the microphysical treatment of Giorgi and Chameides (1986) and Balkanski et al. (1993) for in-cloud scavenging of tracers (or rainout by nucleation), below-cloud scavenging (or washout by impaction) and re-suspension of evaporating rain droplets (Appendix C). Aerosol microphysical processes influencing the distribution of tracers will be discussed in Sections 7.2 and 7.3. Other considerations for vertical turbulent mixing and known limitations are given in Appendix C.

4.4. The GOCART sulfur chemistry module

The original sulfur module is described in Chin et al. (2000a). The chemical production of SO_2 occurs via DMS oxidation within the marine boundary layer, while the chemical loss of SO_2 is represented by two main transformations: the reaction with radicals OH and NO_3 in the gas-phase and with H_2O_2 in the aqueous-phase, the latter being most efficient in the presence of cloudy air. The SO_2 depletion by heterogeneous reactions on the surface of aerosols (Gray et al., 2010) or by oxidation with O_3 in the aqueous-phase (Liang and Jacobson, 1999) is currently not included in GOCART. In addition to these simplifications, pH variations in cloud droplets are neglected and pH is fixed at 4.5, which avoids dealing with SO_2 lifetime dependency on pH (Matthijsen et al., 1997; Liang and Jacobson, 1999).

The in-cloud reactions are diagnosed using the cloud liquid water content (CLW) and fractional cloudiness (FC) provided by the Purdue Lin et al. (1983) bulk microphysics module and the CAM radiation module respectively. FC is diagnosed according to the scheme of Xu and Randall (1996; see Table 3). In cloudy cell and within the cloud fraction, the formation of SU is governed by the concentration of the limiting reagent, i.e., the lesser amount between SO_2 and H_2O_2 (Chin et al., 2000a). Chemical species are considered well mixed in the aqueous phase, and Henry's law at equilibrium governs the dissolution of the gas-phase species into the cloud water. Table 4 reports rates of gas- and aqueous-phase reactions, and the dissociation rate of species and their gas-water partitioning coefficients.

In the absence of Ozone chemistry in our model setup, concentrations of short-lived radicals OH, NO_3 and H_2O_2 molecules are prescribed using three-dimensional, monthly averaged fields from the Global Modeling Initiative (GMI, Douglass et al., 2004). Diurnal variations of these oxidants are included following the same method applied in Chin et al. (2000a). The fast in-cloud reaction $SO_2 + H_2O_2$ is a sink for H_2O_2, which we replenish with an e-folding time of 3 h like in Chin et al. (2000a).

4.5. Natural and anthropogenic emissions

Ground sources of natural and anthropogenic trace gases and aerosols are specified using the pre-processor PREP-CHEM-SRC (Freitas et al., 2011). Although the pre-processor provides a diversity of emission databases, we chose to include only inventory fields commonly indicated with the GOCART package (Freitas et al., 2011), i.e., emissions of OC, BC, and anthropogenic SO_2 (excluding those from ships). All emissions are taken for year 2006 (see Table 1), a year characteristic of passive volcanic degassing over the Vanuatu volcanic arc. They are provided on a $1° \times 1°$ grid and merge fossil fuel and bio-fuel combustions and transportations from the EDGAR database. Seasonal biomass burning emissions from Duncan et al. (2003a) are not applied. Finally, the original non-erupting (i.e. passive) volcanic SO_2 emission inventory originates from the AeroCom program, and volcanic sources are prescribed using PREP-CHEM-SRC (e.g. Stuefer et al., 2012). At $1° \times 1°$ horizontal resolution, the representation of the volcanic plume remains crude: the mass flux is assumed instantaneously diluted within the grid cell, but with a vertical injection following a parabolic form. The year

Table 4
Reaction rates used in the GOCART sulfur chemistry module.

Reaction	Rate	Reference
Gas chemistry (unit: $cm^3\ molec^{-1}\ s^{-1}$)		
DMS + OH^- > SO_2 + …	K1 = $1.2.10^{-11} e^{-260.0/T}$(OH abstraction channel)	DeMore et al. (1997)
DMS + OH^- > 0.75SO_2 + 0.25MSA	K2 = $1.7.10^{-42} e^{7810/T}[O_2] / (1 + \alpha)\ \alpha = 5.5.10^{-31} e^{7460/T}[O_2]$(OH addition channel)	DeMore et al. (1997)
DMS + NO_3^- > SO_2 + …	K3 = $1.9.10^{-13} e^{-500/T}$	DeMore et al. (1997)
SO_2 + OH − > sulfate + …	K4 = $K_0 \times K_\infty / (K_0 + K_\infty) 0.6^{\beta}\ K_0 = 3.3.10^{-31}\ (300 / T)^{4.3}$[M] $K_\infty = 1.6.10^{-12}\ \beta = 1 / (1 + [\log(K_0 / K_\infty)]^2)$	DeMore et al. (1997)
Aqueous chemistry (unit: $l\ molec^{-1}\ s^{-1}$)		
HSO_3^- + $H_2O_2^-$ > sulfate	K5 = $6.31.10^{14}\ e^{(-4760/T)}$	Jacob (1986)
Solubility constants (unit: $molec\ l^{-1}\ atm^{-1}$)		
SO_2(g) <-> SO_2(aq)	$1.22e^{3145.5(1/T\ -\ 1/298.15)}$	Jacobson (2005)
H_2O_2(g) <-> H_2O_2(aq)	$7.45.10^4\ e^{6621(1/T\ -\ 1/298.15)}$	Jacobson (2005)
Dissociation constant (unit: $molec\ l^{-1}$)		
H_2SO_3 <-> HSO_3^- + H+	$1.30.10^{-2}\ e^{2013(1/T\ -\ 1/298.15)}$	Jacob (1986)
HSO_3^- <-> SO_3^{2-} + H+	$6.31.10^{-8}\ e^{1505(1/T\ -\ 1/298.15)}$	Jacob (1986)

[M] = air density (molec air cm^{-3}).

2006 inventory of ground emission is repeated throughout the simulation period.

Natural fluxes for DMS, sea salt and dust depend on the local meteorology. For DMS, we use the original WRF-Chem/GOCART scheme, i.e., biogenic emission of DMS is parameterized using the air–sea transfer function of Liss and Merlivat (1986; with surface wind and SST dependency) in concert with ocean data from Kettle et al. (1999). It is well known, however, that DMS emission is sensitive to both the emission scheme and the DMS climatology, as shown by Boucher et al. (2003) and in Table 1 (column DMS). A sensitivity study is therefore conducted in Section 7 using the most recent parameterization in the literature and DMS climatology from Lana et al. (2011; Appendix C). Regarding dust, since Australia is a large source of dust for the remote South Pacific (Savoie and Prospero, 1989), their emission is included using the original scheme from Ginoux et al. (2001) implemented in the GOCART dust emission module. As sea salt aerosols and their effect on AOD strongly rely on sea spray parameterization (Fan and Toon, 2011; Jaeglé et al., 2011), we test two source functions (Appendix C). One is the original Gong (2003) scheme already in GOCART sea salt module (Eq. (C.1)), the other (Eq. (C.2)) is adapted from Jaeglé et al. (2011). Eq. (C.2) was designed in GEOS-Chem to better represent AOD and sea salt surface concentrations in the tropics. It differs from Eq. (C.1) by the SST dependence of sea salt emissions.

4.6. Computation of aerosol optical properties

While WRF-Chem includes a radiative transfer module to compute the AOD online (Chapman et al., 2009), we made the choice off computing it offline. This allows us (1) to use the Optical Properties of Aerosol and Clouds (OPAC) database (Hess et al., 1998) with recent revisions for particle-size distributions (PSDs) and aerosol optical properties, and (2) to examine the high sensitivity of computed AOD to PSD assumptions for each aerosol type and to humidity effect on their hygroscopic growth rates. To this end, we use the mass extinction efficiency $ß$ (i.e., the aerosol extinction regardless of effects due to simulated aerosol mass concentrations; unit $m^2\ g^{-1}$; see Eq. (B.7) in Appendix B) previously introduced and discussed in Chin et al. (2002). This sensitivity to PSDs is well illustrated in Fig. B1, where the use of lower particle sizes in WRF-Chem GOCART results in larger value for $ß$ (Eq. (B.7)) that enhances the simulated AOD (Eq. (B.6)). By contrast, larger particle sizes, like those used in Chin et al. (2002), decrease significantly $ß$ (compare $ß$ plots in Fig. B1). Furthermore, small biases in the top range of *RH* values would skew the AOD.

To retrieve the aerosol optical properties offline, we use the post-processor FlexAOD (http://pumpkin.aquila.infn.it/flexaod/; see also Appendix B). In the calculation, PSDs for each aerosol type are approximated by a gamma distribution for dust and lognormal distributions for the other aerosols. PSDs for SS are assumed to follow a bimodal lognormal distribution, with accumulation (SSA) and coarse mode (SSC) for the first and second modes respectively (Chin et al., 2002). Since two source functions for the generation of SS are evaluated based on AOD (Section 5.2), Appendix B provide details on our choice of geometric parameters for PSD of SSA and SSC (Table B1). We also specify in Appendix B how the four sea salt size bins computed in GOCART are partitioned between SSA and SSC in the AOD computation.

4.7. WRF-Chem/GOCART experiment protocol

Since our objective is to isolate the role of Ambrym on the regional aerosol composition, we focus on a time period with typical non-eruptive activity in the Vanuatu volcanic arc. One difficulty is that explosive and extreme degassing events determine the natural variability in this archipelago. This is well illustrated in Bani et al. (2009) and in Fig. 9 showing monthly means of OMI SO_2 burdens (solid black line). One sees a continuous and quiet degassing period due to Ambrym from September 2005 to January 2010. Thus, our study focuses on the period of October 2005–October 2008, when Ambrym dominates the Vanuatu SO_2 emissions. This period starts after the extreme Ambrym degassing event of the 2004/2005 austral summer (Bani et al., 2009) and ends before the increasing occurrence of row anomalies in OMI products. However, we discard the short 8–11 October 2006 period corresponding to a high SO_2 spike (Fig. 9) related to the eruption of Rabaul in PNG. Transported in the upper troposphere by the subtropical Jet Stream, the SO_2 cloud extended over Vanuatu during that period (Carn et al., 2009).

The initial and boundary meteorological conditions are provided by the National Center for Environmental Prediction final analysis (NCEP-FNL) available at $1° \times 1°$ spatial resolution every 6 h. Chemical initial and lateral conditions are specified from 6 hourly data of the Model for OZone And Related chemical Tracers MOZART4, with NCEP data for meteorological forcing (Emmons et al., 2010). The model was initialized at 00 UTC 01-SEP-2005 and integrated up to 01-OCT-2008, using the same time step of 300 s for meteorology and chemistry. 6-hourly model outputs are analyzed, including meteorological and chemical variables and tendency terms of budget equations for SU and SO_2. The simulation is performed without nudging to large-scale data, implying that the model can freely develop its own internal variability. The first model year is discarded due to spin up, as indicated by fluctuations of the simulated SO_2 burden time series in the first year (Fig. 9, lines 3 or 4).

As detailed in Table 5, a set of six model experiments is conducted to address the sensitivity of sulfur burden to sources (and sinks) of sulfate precursors. Two model experiments (CTRL and RUN1) are designed to address the impact of passive volcanic degassing due to Ambrym on tropospheric composition: in CTRL, we allow passive degassing from all volcanoes using the up-to-date AeroCom volcano database for non-eruptive degassing. Since the AeroCom inventory underestimates the release of SO_2 by Vanuatu volcanoes (~2.15 kT d^{-1}), we adopt the degassing rate of 5.4 kT d^{-1} indicated by Bani et al. (2012) for Ambrym. In RUN1 we investigate the role of volcanic emission due to Ambrym by suppressing this volcanic source. Four others experiments are designed to address the model sensitivity to the parameterization of aerosol processes, including the adjustment of the source function for sea salt (RUN2), the influence of DMS source (RUN3) and loss processes related to wet deposition and aerosol re-suspension (RUN4 and RUN5).

It is worth noting that the volcanoes located in northern MVA and eastern Indonesia are also included in our six experiments, using SO_2 volcanic fluxes given in the AeroCom inventory. They are for example

Table 5
Description of sensitivity experiments.

Experiment	Physics	Wet deposition scheme	Tracer resuspension	DMS sea–air transfer scheme	Oceanic DMS climatology	Sea-salt source function	Volcanic sources
CTRL	Table 3	Jacob et al. (2000)	Yes	Liss and Merlivat (1986)	Kettle et al. (1999)	Gong (2003)	Table 1
RUN1	Table 3	Jacob et al. (2000)	Yes	Liss and Merlivat (1986)	Kettle et al. (1999)	Gong (2003)	As in Table 1, but with Vanuatu volcanic degassing shut down
RUN2	Table 3	Jacob et al. (2000)	Yes	Liss and Merlivat (1986)	Kettle et al. (1999)	Jaeglé et al. (2011)	Table 1
RUN3	Table 3	Jacob et al. (2000)	Yes	Nightingale et al. (2000)	Lana et al. (2011)	Gong (2003)	Table 1
RUN4	Table 3	No	No	Liss and Merlivat (1986)	Kettle et al. (1999)	Gong (2003)	Table 1
RUN5	Table 3	Jacob et al. (2000)	No	Liss and Merlivat (1986)	Kettle et al. (1999)	Gong (2003)	Table 1

volcanoes in PNG and Solomon islands in the northern MVA, which are known to experience strong passive degassing, but our study is not dedicated to their accurate model representation. However, the last top-down non-eruptive budget for PNG (McCormick et al., 2012) is roughly similar to past estimates from McGonigle et al. (2004), which are incorporated in the AeroCom inventory.

5. Model verification and adjustments

Parameterizations related to the hydrological cycle may cause large variability in cloud macrophysical properties (i.e. cloud liquid water content, fractional cloudiness and rain rate), having deep impact on chemical processes and tracer lifetime (Matthijsen et al., 1997). Another common source of uncertainty is the modeling of sea salt aerosols, having large impact on the aerosol burden (Jaeglé et al., 2011). Model verification and adjustments are detailed in this section.

5.1. Simulated rainfall and cloud properties

The Inter-Tropical Convergence Zone (ITCZ) and SPCZ are major features of the tropical western Pacific dictating the local climate of tropical islands (Lefèvre et al., 2010). Uncertainties in their representation may alter the source (e.g., in cloud oxidation) or sink (e.g., wet deposition) of tracers, impairing their fate along the MVA.

The typical ITCZ-SPCZ asymmetry commonly observed in satellite precipitation fields (Schumacher and Houze, 2003; Vincent et al., 2011), a key feature not easily simulated by GCMs that tend to develop the "double-ITCZ" pathology (Song and Zhang, 2009), is well reproduced in the mean state of the simulated rainfall patterns (Fig. 1). The model captures the permanent convective belt associated with the ITCZ, separated from the SPCZ by a region of dry air over the Pacific equatorial cold tongue. The SPCZ exhibits the typical northwest-southeast tilt, aligned with the MVA. Overall the model simulates reasonably well the mean tropical SW Pacific climate, as seen in comparisons of model annual fractional cloudiness (FC), outgoing longwave radiation (OLR), and sea level pressure fields against observations in the MVA region (Fig. 2). However, the model overestimates the cloudiness associated with permanent convection within the ITCZ North of PNG, as indicated by lower than observed OLR (Fig. 2d) and higher than observed FC (Fig. 2b). In the SPCZ, simulated FC is slightly lower than observed and the region of high cloudiness indicated with OLR below 240 W m^{-2} is smaller than observed (compare Fig. 2d and c), meaning that the model introduces dryer air conditions over the southern MVA. This is also true in regions of large-scale subsidence in general. Furthermore, in relation with weak cloudiness conditions in the SPCZ, the area of heavy rainfall larger than 6 mm d^{-1} expands toward the tropics in the model (Fig. 2b), implying that the model does not exactly capture the observed balance between cloud and rain formation in the SPCZ and places like Vanuatu.

The existence of seasonal biases in the Vanuatu region in precipitation, total atmospheric water vapor and cloud liquid water (CLW) is documented in Fig. 3, using zonal averages from 160°E to 174°E. The model estimates the total vapor reasonably well (Fig. 3a,b), both spatially and seasonally, with simulated total vapor of about 10% higher than observed, slightly above the AMSRE RMS error of about 6% (Fetzer et al., 2006). This reflects a slight intensification of the simulated hydrological cycle, due to stronger evaporation and precipitation in the model (Trenberth, 1998). In agreement with the moderate cloudiness bias (Fig. 2), the model generates weaker than observed CLW in the SPCZ in summer and winter (Fig. 3a and b), but this quantity remains high, i.e., above 100 g m^{-2} (150 g m^{-2} in AMSRE) and 80 g m^{-2} respectively. Toward the subtropics, south of 17°S where thin non-raining clouds prevail (Schumacher and Houze, 2003), the model results agree better with observations. In austral summer, higher surface precipitation relative to AMSRE are also found in the SPCZ region between 5°S and 25°S including Vanuatu with up to 55% more than observed, while winter

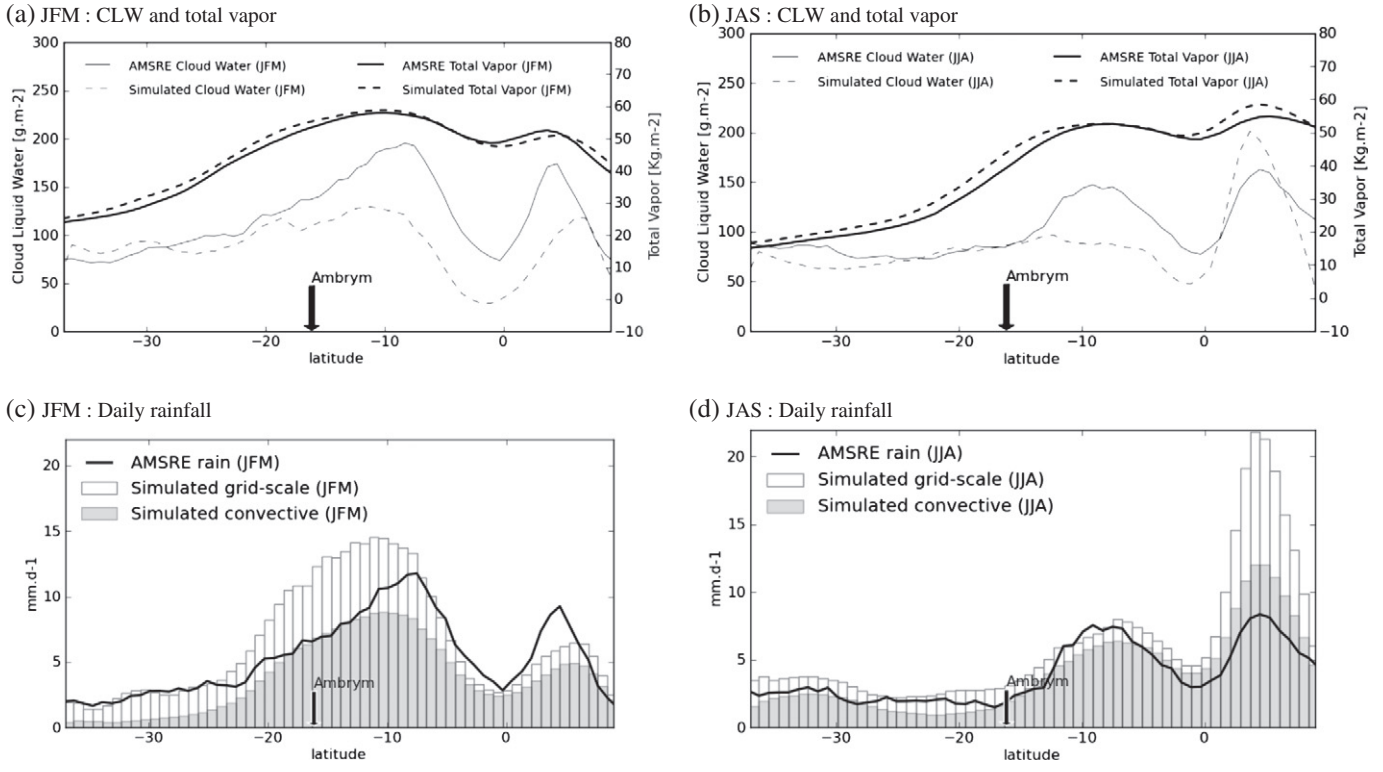

Fig. 3. Zonal mean (160°E–174°E) and seasonal mean (2006–2008) hydrological quantities. (a) and (b) total vapor and cloud liquid water (CLW) content from model and AMSRE observations in austral and boreal summer (JFM January–February–March and JAS July–August–September respectively); (c) and (d) daily mean surface precipitation from model and AMSRE observations in JFM and JAS respectively, with partitioning of grid-scale and convective precipitation.

precipitation agrees better with observations. In the ITCZ, the strongest rainfall bias occurs during boreal summer, with predicted rainfall as large as twice that observed.

Partitioning the simulated precipitation into grid-scale and sub-grid scale (Fig. 3c and d) reveals that the fraction of rain resolved by the microphysics scheme (referred to as "grid-scale") increases sharply up to 40 % in the warm season, both in ITCZ and SPCZ. The increase of grid-scale precipitation in summer is due to higher occurrence of mesoscale convective systems (Jourdain et al., 2011). The seasonal precipitation bias, as evidenced in Fig. 3c and d, may have multiple origins. To our knowledge, such bias in summer may be related to (1) too strong moisture supply coming from low-level convergence, (2) too strong conversion to rain in the deep cumulus scheme (hereafter CU), and (3) too much conversion due to the grid-scale bulk microphysics scheme.

Overall, since simulated precipitation is biased high in summer, wet deposition of tracers in the southern SPCZ should be overestimated in summer as well. But, since wet deposition is diagnosed using the grid-scale scheme only (Section 4.3), which has lesser contribution to total precipitation, this loss process may finally be underestimated in the model. The issue of uncertainties in wet deposition will be investigated further in Section 7.3. It is worth noting that the slight underestimation in simulated FC and CLW may also slightly reduce the oxidation efficiency of dissolved SO_2 to sulfate aerosols in cloud droplets, as documented in Matthijsen et al. (1997).

5.2. Simulated winds

Wind speed 10 m above the sea surface (U_{10}) is a key parameter used in parameterization for SS and DMS emission. The DMS transfer velocity at the sea–air interface is roughly proportional to U_{10} while SS emissions are proportional to $U_{10}^{3.41}$, meaning that small error in wind speed can impact the production of marine aerosols. Distributions of the observed and simulated surface wind speed in the Vanuatu archipelago are compared in Fig. 4. Overall, the simulated wind speed is in reasonable agreement with observation, but the model tends to underpredict moderate wind speed in the range of 8–12 m s^{-1} and overpredict low wind speed. Thus, this small bias in the simulated wind speed distribution may reduce the source strengths of natural aerosols. However, common uncertainties in both emission parameterizations and particle size distributions can lead to higher discrepancies in the simulated aerosol budgets and aerosol optical properties (Textor et al., 2006), as we investigate now.

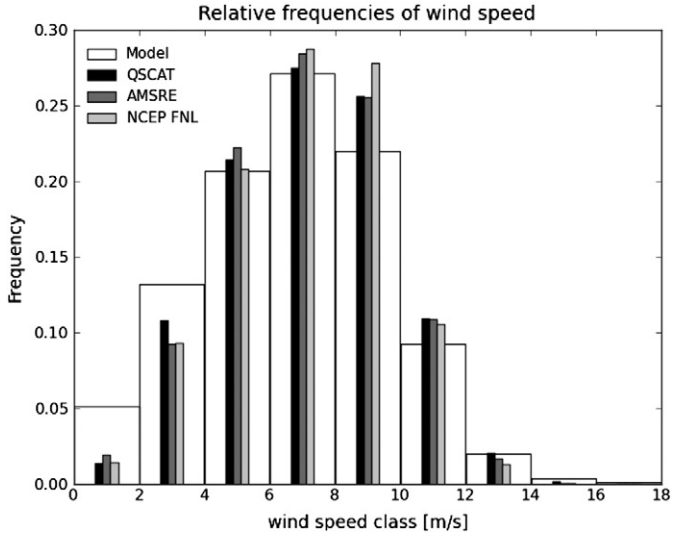

Fig. 4. Normalized distribution of simulated surface wind speed compared with measurements from AMSRE and QSCAT (QuikSCAT swath product at 12.5 km; Lefèvre et al., 2010) and surface winds from NCEP/FNL (assimilating QSCAT winds). Number of coincident observations and model data: 91,045. These statistics are given for the time period 01-Oct-2005 to 01-Oct-2008 and regional box [160E:174E; 21S:11S].

5.3. Sensitivity of sea salt properties to generation scheme and size distributions

In the remote marine boundary layer, SS aerosols are significant players and have a large contribution to total AOD in visible wavelengths (Shinozuka et al., 2004). They provide also additional surface for heterogeneous reactions and greatly impacts the chemistry in the troposphere (Athanasopoulou et al., 2008). Yet, they remain one of the most poorly constrained aerosols in GCMs (Textor et al., 2007). Despite a large body of literature, it is not clear whether their contribution to AOD relies on their mass burden (which depends on the generation scheme and model physics; see Jaeglé et al., 2011 and Textor et al., 2007, respectively) or their microphysical properties entering the radiative transfer calculations (e.g., their size distribution; Li et al., 2008). To better constrain the SS burden and their optical properties in GCMs, various parameterizations were developed and tuned (Fan and Toon, 2011; Jaeglé et al., 2011). Alternatively (and more radically), scaling factors were applied to simulated SS concentrations in order to fit the observations (Saide et al., 2012).

Here, we explore the sensitivity of SS simulation to their source parameterization using CTRL and RUN2. In CTRL, the standard Gong (2003) sea spray formulation (Eq. (C.1)) is used in the GOCART SS emission module, whereas in RUN2 the source function with SST dependence (Eq. (C.2)) from Jaeglé et al. (2011) is used instead. It is worth noting that the same SST (the NOAA Optimum Interpolation V2 SST) is applied in Jaeglé et al. (2011) and our model setup. For the calculation of their optical extinction with FlexAOD (Section 4.6 and Appendix B), the SS size distributions for accumulation (SSA) and coarse modes (SSC) are similar in the two experiments: GOCART SS mass size bins [0.1–0.5 μm] and [0.5–1.5 μm] are assumed to follow SSA and SSC size distributions respectively, while the two others GOCART mass size bins, i.e., [1.5–5 μm] and [5–10 μm] are treated like giant and ultra-giant SS respectively, following Jaeglé et al. (2011). The effective radius r_{eff} (Table B1, gray shaded rows) is reduced to 0.25 μm for SSA and 1.1 μm for SSC. This revision for SSA and SSC size parameters is supported by recent observations (Jaeglé et al., 2011) and their values contrast with those used in Chin et al. (2002) or in OPAC (Table B1).

Fig. 5 displays the mass concentration of SSC as a function of surface wind speed for the two SS generation schemes tested. SSC observations from PMEL cruises and a semi-empirical SSC function, both referenced in Jaeglé et al. (2011), are superimposed. Observed and predicted SSC concentrations agree reasonably well in the range of 1–5 m s^{-1}, but both formulations overestimate the SSC mass concentration at wind speeds greater than 6 m s^{-1}. Note that the Jaeglé source function shows the largest bias, leading us to conduct further verifications.

The aerosol collection of the University of Miami Aerosol Group (Savoie and Prospero, 1989, hereafter referred to as the Miami Collection) is dedicated to assess the aerosol composition and role of sources in the remote tropical Pacific atmosphere, and includes SS observations. Whatman-41 filters with mass collection efficiency greater than 95% for SS (Savoie et al., 1989) have been used for their collection. Mean surface concentrations at six sites across the South Pacific are reported in Table 7, column 8, gray shaded rows. Note that only half of the sites included in the SS comparison (American Samoa, New-Caledonia, and Norfolk Island) are not contaminated by local surf conditions (Dr. Prospero's personal communication). The results show that predictions of surface SS concentrations using the Gong scheme have the best skill, with mean values very close to measurements. In contrast, surface SS concentrations are overestimated by about 80% in the tropical band using the Jaeglé source function (Table 7, column 9), which is surprising since this scheme was designed for improvement in that band (Jaeglé et al., 2011). The difference, however, is less than 5% in the subtropics where the Jaeglé et al. scheme mimics the Gong scheme.

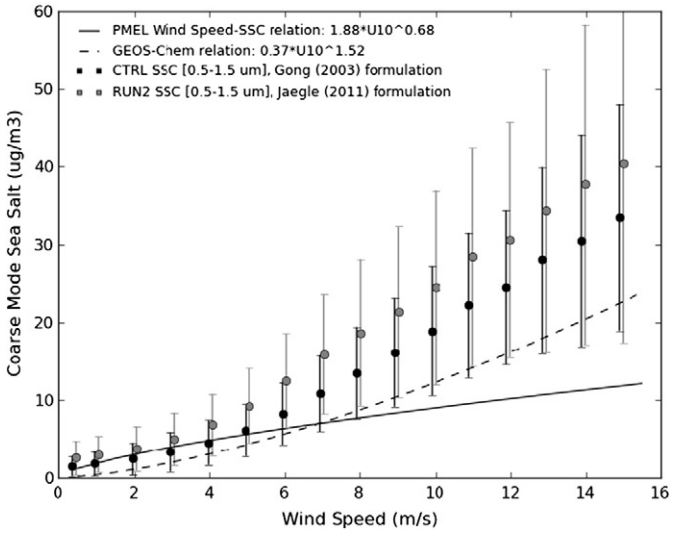

Fig. 5. Simulated wind speed dependence of coarse mode sea-salt (SSC) mass concentration using source functions from Gong et al. (2003, Eq. (C.1)) and Jaeglé et al. (2011, Eq. (C.2)); error bars given by the standard deviation. Model statistics are constructed using periods of stable wind conditions as defined in Mulcahy et al. (2008), i.e. daily standard deviation of simulated U_{10} is less than 2 m s^{-1}; we consider the time period 01-Oct-2005 to 01-Oct-2008 and regional box [154E:179.5E; 37S:5S]. For comparison, the empirical law given by the PMEL in-situ observations and the simulated relation given by GEOS-Chem are superimposed in dashed and solid black curves respectively. These relations are given in Jaeglé et al. (2011).

To further test the two SS generation schemes and evaluate our assumptions in SSA and SSC particles size distributions, the SS AOD is now computed offline with the FlexAOD postprocessor and the results compared to empirical functions (O'Dowd, et al., 2010; Fan and Toon, 2011). The SS AOD includes the contribution of both SSA and SSC, while giant and ultra giant SS are not included since they are less optically active (Appendix B). In Fig. 6, two power-law empirical functions

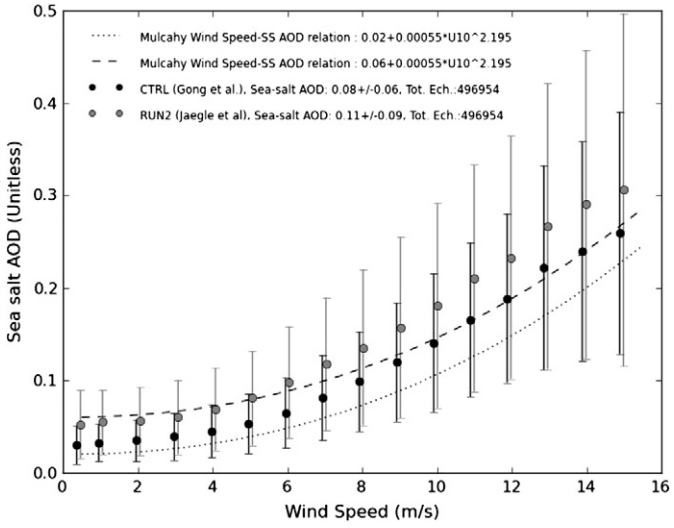

Fig. 6. Wind speed dependence of sea-salt optical depth at λ = 550 nm (including SSA and SSC modes) according to WRF-Chem using source functions from Gong et al. (2003; Eq. (C.1); black spots) and Jaeglé et al. (2011; Eq. (C.2); gray spots); the error bar is given by the standard deviation. The original Mulcahy et al. (2008) law of optical depth versus wind speed for clean marine aerosols is represented by the black dashed curve, while the dotted curve displays the same law but with minimum value (at $U_{10} = 0$) reduced from 0.06 to 0.02, as suggested by Fan and Toon (2011). The model statistics are constructed using simulated SS AOD for stable wind conditions as defined in Mulcahy et al. (2008): daily standard deviation of simulated U_{10} must be less than 2 m s^{-1}. The number of model data considered in the statistics are: 496,954; time period 01-Oct-2005 to 01-Oct-2008; regional box [154E:179.5E; 37S:5S].

of SS AOD versus wind speed from Mulcahy et al. (2008) are used for comparison. The results in Fig. 6 show that SS AOD predictions obtained using the Gong source function are well bounded by the two empirical power-laws, but not when using that of Jaeglé et al. (2011). Overall, the model results are in reasonable agreement with observations with (1) our choice of SS source function based on the Gong scheme; and (2) our settings for particle size distributions applied to both SSA and SSC.

6. Aerosol distribution and composition: role of the passive volcanic degassing

Using WRF-Chem and satellite observations, we now investigate the impact of Ambrym volcano on the regional aerosol composition. First, the sulfate precursor volcanic source is assessed, by comparing the SO_2 burden in CTRL results with OMI trace gas products. Second, a cross-examination of simulated and observed aerosol optical properties is performed to retrieve the regional air composition and isolate the influence of Ambrym.

6.1. Assessment of sulfate precursors emitted from Ambrym

6.1.1. Gas spreading associated with volcanic degassing

Fig. 7 displays the mean column-integrated SO_2 VCD from CTRL outputs and OMI observations (inset) for the period 01-Oct-2006 to 01-Oct-2008; Fig. 8 displays their meridional average along a band centered on Ambrym (depicted by a gray shading on Fig. 7). In the vicinity of the Vanuatu archipelago, the spatial distribution and range of SO_2 VCD values are similar in the model and observations. Since we have imposed Ambrym as the sole SO_2 volcanic source for the Vanuatu arc (Section 4.7), the good agreement between model and data confirms the key role played by this volcano on the local SO_2 budget.

The observed gas spreading is rather isotropic around Ambrym (inset), a feature also represented in the model, even though the model under-predicts the observed eastward spreading (Fig. 8). That eastward SO_2 spreading seen in OMI is likely linked to the eastward advection of gases by westerlies above the trade-wind inversion, indicating that, the model may underestimate gas exchanges from the lower to the free troposphere. In addition, the model misses mesoscale patterns due to its relatively coarse resolution of island-scale dynamics including diurnal heating effects (Lefèvre et al., 2010). Nevertheless, the model captures the right range of SO_2 VCD spatial variability, as depicted by the error bars in Fig. 8.

6.1.2. Accuracy of volcanic SO_2 burden observation

OMI SO_2 observations have proven useful to evaluate the volcanic budget (Bani et al., 2012; McCormick et al., 2012). They have also provided top-down constraints on global SO_2 emissions through inverse modeling (Lee et al., 2011). But the accuracy of SO_2 burden inferred from space using near daily, cloud contaminated, noisy and subsampled satellite data is questionable and may impair the actual SO_2 budget evaluation, as pointed out in the aforementioned studies.

To assess the error made in top-down methods, we sample the simulated SO_2 VCD from CTRL (Table 5) as if they were observations. Eq. (1) is applied to the model outputs to evaluate the impact of satellite sampling and integration area on the retrieval of the SO_2 mass burden due to Ambrym. To help in the comparison, we use the SO_2 VCD anomaly between CTRL and RUN1 (Table 5) to isolate the simulated SO_2 mass burden due exclusively to Ambrym. The results are displayed in Table 6 and also in Fig. 9.

First, the effect of satellite sampling on the retrieval of SO_2 mass burden is evaluated using the 10° latitude by 14° longitude box depicted in Fig. 7 (a box similar to the domain of integration applied in Bani et al., 2012). With the model sampled using OMI swaths (Fig. 9, curve 2), the simulated top-down SO_2 mass burden agree remarkably well with OMI estimation displayed in curve 1 (2.43 and 2.24 kT(SO_2) respectively; relative difference: 7.5%) and their variances are similar. This very good

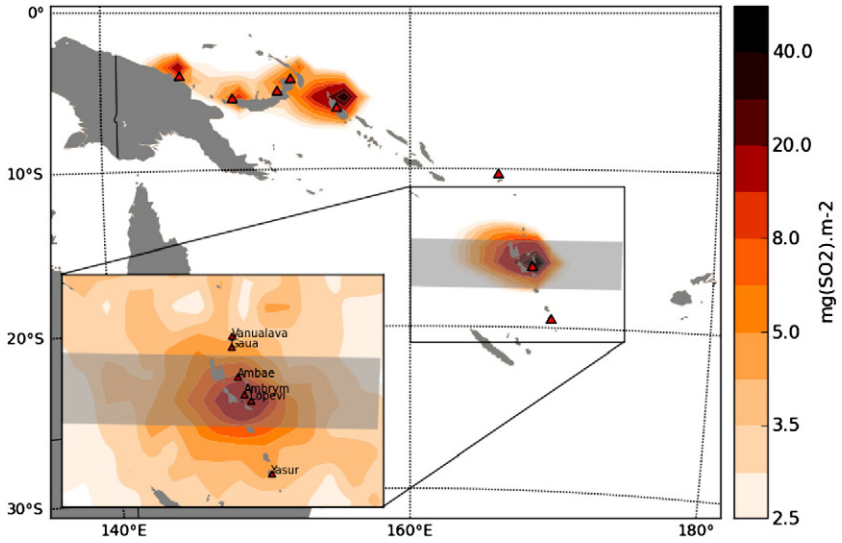

Fig. 7. Volcanic SO_2 vertical column density (VCD) in mg m^{-2} averaged between 01-Nov-2006 and 01-Oct-2008 from the model (main chart) and from OMI (map inset). Only valid OMI VCD (Section 2.1) with value above the 0.6 DU sensor detection limit are considered in the averaging process. Simulated SO_2 fields use the same OMI data reduction, i.e., data screening coherent with the OMI sensor overpass (Section 2.1). In the inset, active Vanuatu volcanoes are indicated. It is in that box that volcanic SO_2 mass burden is computed using Eq. (1) (see text). Light shaded gray strips show the region used for meridional averaging in Fig. 8.

agreement contrasts with the box-averaged value computed from the full model solution (Fig. 9, curve 3). The full SO_2 burden is 53% higher than that estimated from satellite sampling (compare rows 2 and 3, Table 6) and has much lower variance (std: 0.03 instead of 0.44). These results show that satellite swath sampling causes a clear underestimation of SO_2 VCD but large spurious signal variability. Note that the lack of correlation between curves 1 and 2 in Fig. 9 may be explained by the model's internal variability, which is stochastic in nature and reduces predictability (in the absence of data assimilation or nudging technique). Second, the box approach applied in OMI swaths to evaluate the volcanogenic budget (Bani et al., 2012; McCormick et al., 2012) causes additional reduction in budget estimate. This is apparent in the comparison between curves 2 and 4. The latter is the simulated SO_2 mass burden due to Ambrym without sampling or geographical constraint. We see that with the top-down method the SO2 volcanogenic budget is reduced by about half (compare also rows 2 and 4 in Table 6).

In summary, using the up-to-date SO_2 emission rate given by Bani et al. (2012), we find very good agreement between observed and simulated SO_2 mass burden when using the same sampling strategy. However, sampling biases appear to lower SO_2 burden by 50%, which is within the range [30%–70%] evaluated from field studies (e.g., Bani et al., 2012; McCormick et al., 2012). In addition Eq. (2) gives a simulated SO_2 lifetime of 20 h (Table 6), similar to values found in the tropical band by Lee et al. (2011). It is also in agreement with the value of 18 h in PNG evaluated using successive OMI overpasses by McCormick et al. (2012). These results provide additional confidence in our modeling approach for investigating the influence of Ambrym on air composition.

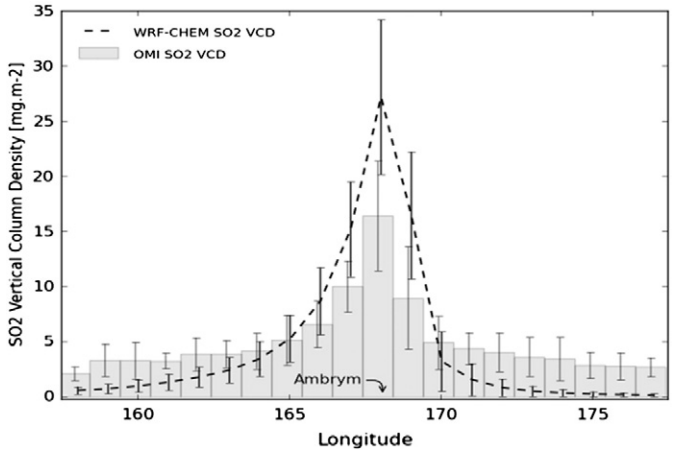

Fig. 8. Zonal structure of observed and simulated SO_2 VCD across Ambrym. Values are meridional averages in the shaded band shown in Fig. 7. Error bars are standard deviations of monthly-mean data.

6.2. Total AOD and Ambrym contribution

Fig. 10a and b displays 3-year average MODIS/Aqua and simulated AOD (CTRL run) at $\lambda = 550$ nm. Fig. 10d shows the AOD seasonal variability for both model and satellite estimates. Simulated AOD from the global GSFC/GOCART G4P0 science product distributed by the Giovanni Data Portal (http://disc.sci.gsfc.nasa.gov/gesNews/gocart_data_V006) is also shown for comparison (Fig. 10c). The GSFC/GOCART products are widely used in combination with satellite observations to assess the global aerosol composition (Colarco et al., 2010; Yu et al., 2010; Jones and Christopher, 2011) or to infer the aerosol impact on cloud properties (Koren et al., 2010).

Unlike with the GSFC/GOCART product, we find a quite close agreement between satellite and simulated AOD using WRF-Chem/GOCART over the SW Pacific (compare Fig. 10a and b). The only notable difference with MODIS AOD is some underestimation in southwestern PNG, the Indonesian Maritime Continent and northern Australia, where the

Table 6
Sensitivity of top-down SO_2 mass burden and SO_2 lifetime associated with Ambrym degassing to satellite subsampling and integration area. Calculations are made for the 2-year period 01-Oct-2006 to 01-Oct-2008.

SO_2 mass burden from	Domain size	Sampling	Mean [Ktons(SO_2)]	Std	Lifetime [h]
OMI	14° by 10°	OMI, original	2.26	0.47	10
Model	14° by 10°	Cells coincident with OMI pixels	2.43	0.44	11
Model	14° by 10°	Grid mesh	3.73	0.03	17
Model	WRF domain	Grid mesh	4.54	0.04	20

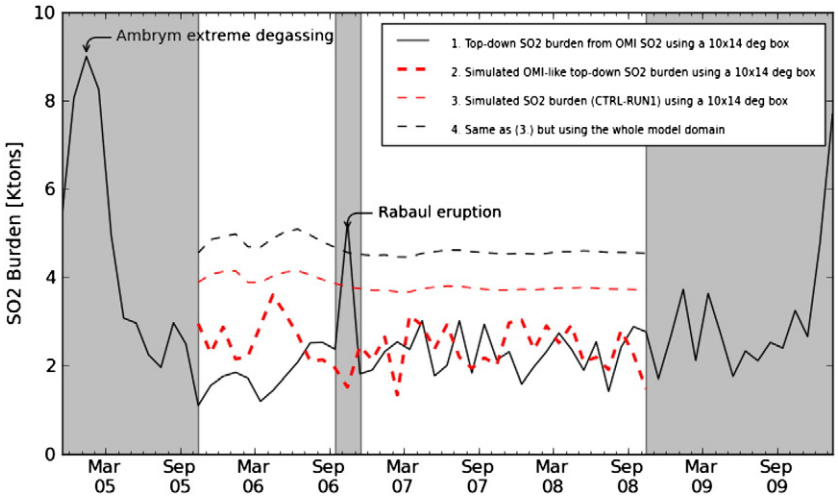

Fig. 9. Observed monthly-mean SO_2 burden retrieved from TRL OMI SO_2 vertical column density (VCD; solid black curve 1) between 2005 and 2009. Curves 2, 3 and 4 are the simulated top-down SO_2 burden used to test retrieval procedures in OMI observations. They reproduce the results of OMI subsampling and sensor detection limit (Curve 2), compared with unaltered model computation on the same subdomain (Curve 3) and on the whole computational domain (Curve 4). The regional 10° × 14° box used for SO_2 burden computation of curves 1–3 is depicted by the inset in Fig. 7 (160°E–174°E – 11°S–21°S). The whole model box used for the Curve 4 is displayed in Fig. 1. The simulation does not cover shaded regions and the noticeable Rabaul (PNG) eruptive event is excluded from analysis.

satellite instrument captures the effect of large biomass burning events (Duncan et al., 2003ab). Further investigations using satellite observations, for which details are beyond the scope of this study, show that the absence of Indonesian wildfire biomass burnt emissions (Table 1) explains this discrepancy. This error is also present in the GSFC/GOCART AOD (Fig. 10c).

In the remote marine boundary layer, east of PNG, the 3-year average maps show similar patterns (Fig. 10a and b). A clear feature is the strong AOD signal in the Ambrym volcanic degassing plume, due to the formation of SU aerosols. As for seasonal variability, observed and simulated AOD also exhibit strong similarities in the Vanuatu zonal band (Fig. 10d, the two upper seasonal diagrams). The wet and warm season (Jan–Apr) is characterized by low sea spray formation as trade winds relax during the seasonal strengthening of the SPCZ in the region. This strengthening also increases the wet removal of aerosols as convective rain forms over the SPCZ region, including Vanuatu. This leads to a sharp aerosol burden reduction both in model results and observations during that time period. Conversely, in austral winter, strong trade winds and drier conditions occur as the SPCZ moves northward resulting in larger AOD signal both in model values and satellite observations.

Contrasting with our results, there are large discrepancies between GSFC/GOCART AOD and observations, both in terms of AOD magnitude (Fig. 10c) and seasonal variability (Fig. 10d, lower panel). The origin of biases in the GSFC/GOCART AOD will be discussed later (Section 8). Subtle differences also exist (Fig. 10d) like a moderate overestimation of the aerosol burden in the southern side of the SPCZ (between 10°S and 20°S), and underestimation in the convective region between 0° and 10°S. These differences may be related to the absence of the subgrid-scale contribution to the total simulated aerosol wet removal or other misrepresentation of simulated precipitation anticipated in Section 5.1. In the 0°–10°S band, one could also argue that the weak simulated aerosol burden is due to low emission of volcanic SU precursors in PNG, since erupting volcanoes contribute to the SU cycle in this region, as indicated earlier in Section 3.7.

With model results, the impact of volcanoes to the aerosol burden can be determined. Fig. 10 b shows the contribution of Ambrym degassing to total AOD (reported with contour lines). Volcanic SU aerosols from Ambrym are contributing 15% of total AOD (i.e. ~0.025 AOD, close to the MODIS AOD detection limit) as far as 1500 km from the source. Again, these results give us great confidence in the present climate and aerosol model and allow us to explore the distribution of aerosol types that contribute to total AOD.

6.3. Aerosol type detection and contribution to total AOD

To estimate the contribution of aerosol types to the AOD, we rely on the model and the CALIOP aerosol subtyping scheme. Fig. 11a and b compare the structure of the aerosol composition explaining the total AOD using model results and CALIOP retrievals respectively. Because CALIOP observations are often contaminated by clouds in the SPCZ and have a low temporal resolution (Table 2), we use the whole 5 years of CALIOP data time series against the 3-year model results. The agreement is excellent between MODIS and simulated AOD (Fig. 11a) as already shown. The main difference between the CALIOP, MODIS and simulated AOD (Fig. 11b) is the weaker AOD signal associated with Ambrym degassing in CALIOP, which is evident at 15°S. This problem may be related to deficiencies in CALIOP CAD algorithm (see Appendix A), which could miss the identification of fresh SU aerosol layer and/or misclassify it as clean marine subtype (primarily composed of SS, mixed with water soluble components like SU). Such misclassification of components composing the mixture has additional consequences on the aerosol optical extinction profile of the layer, and may explain the discrepancy between CALIOP AOD and other co-located satellite observations, as reported by Kittaka et al. (2011) and Oo and Holz (2011). Algorithm deficiencies definitely limit the usefulness of CALIOP CAD for accurately retrieving aerosol composition in the context of strong passive volcanic degassing.

Despite the difference in aerosol mixture definition between the model and CALIOP (Section 4.1), and excluding the volcanic degassing band between 10°S and 20°S, useful information can be retrieved on aerosol composition by examining Fig. 11a and b. Here, we assume that SS and SU compose the clean marine aerosol mixture defined in CALIOP, and DU and CC (OC + BC) the other CALIOP mixtures (i.e. polluted dust, desert dust and smoke). In the equatorial belt, the clean marine contribution to AOD is dominant in CALIOP (about 94%; 89% in the model). Toward the subtropics off 20°S, the marine aerosol contribution decreases slightly from 91 to 85% (85 to 79% in model). As SS dominates the AOD signal (Fig. 11a), especially SSC representing nearly half the simulated AOD, it confirms that accurate representation of SS is essential in aerosol and troposphere chemistry modeling.

Polluted dust and continental aerosols constitute the second dominant mixture with larger contribution toward the subtropical belt off 20°S. Their mean altitude as indicated by CALIOP is 2 km (not shown), implying that the polluted continental material is mainly transported in the lower troposphere together with clean desert dust also retrieved

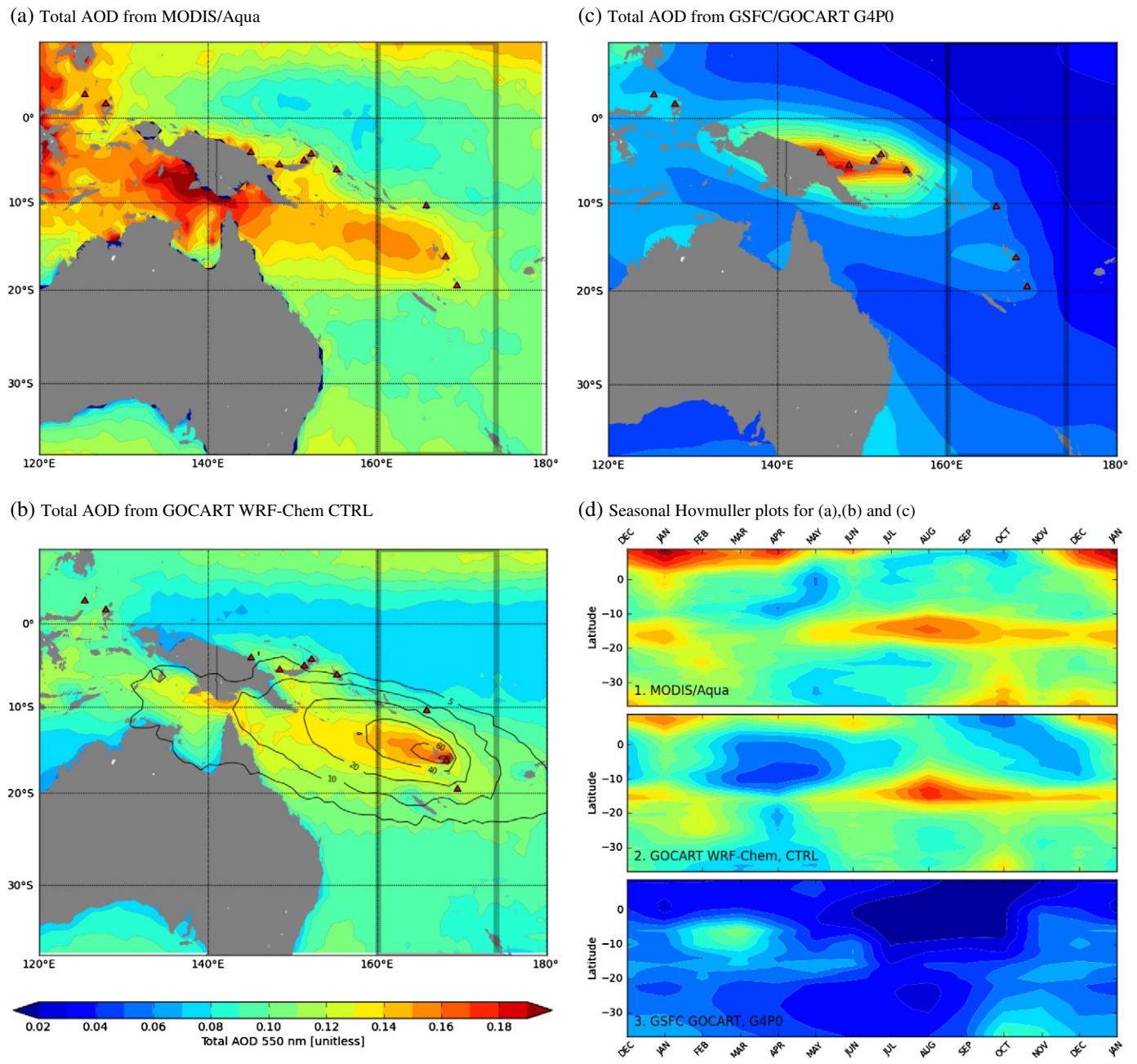

Fig. 10. Three-year average (01-Oct-2005 to 01-Oct-2008) of observed (MODIS/Aqua; panel a) and simulated AOD (panel b) at 550 nm using FlexAOD with CTRL outputs. The contribution (in percent) from Ambrym degassing to total AOD due the formation of high scattering SU aerosols is represented in contours of panel b. AOD at 550 nm from the GSFC/GOCART G4P0 science product is also presented for comparison (panel c). Panel d shows the seasonal cycle using y-t (-Hovmuller-) diagrams for each datasets. Here, the mean zonal AOD between 160°E and 174°E is displayed (as indicated with gray lines on each map). Note the simulated AOD is sampled in coincidence with valid MODIS observations. The main active volcanoes are displayed with red symbols.

in CALIOP (Fig. 11b). Aloft, smoke from biomass burning is transported in the middle troposphere (CALIOP mean layer altitude 5 km), with possible origin from South Africa (Singh et al., 2000) and Indonesia (Duncan et al., 2003b) wildfires. From their respective contribution to CALIOP AOD, these two mixtures (clean desert and smoke) appear to be minor contributors to the aerosol composition.

The model accurately retrieves the larger contribution of DU, a proxy for polluted continental mixture and desert dust, in the subtropical belt (Fig. 11a). Surface DU concentrations from the Miami Collection (Savoie and Prospero, 1989), displayed in Table 7 (column 7) are about four times higher in the subtropical belt than in the tropics, confirming the satellite and model patterns. But the Miami Collection is not exempt of errors. For example at Yaté, located on New-Caledonia's eastern coast, observed DU concentrations are surprisingly lower than in pristine and remote tropical stations. This is because aerosol collection was operated during offshore wind conditions only (Savoie and Prospero, 1989) and because the surrounding mountainous barrier isolates the station. These conditions are not suitable for the sampling of the Australia outflow, probably resulting in too small values of DU measurements.

On average, the structure of the aerosol composition given by CALIOP (Fig. 11.b) does not exhibit a dust signal in the Vanuatu region, suggesting that passive degassing plumes are ash-free. But, limitations in the CALIOP CAD signaled earlier may provide no definitive conclusion. However, during strong eruptive events, both CALIOP and MODIS AOD report an ash contribution to the AOD, with the detection of

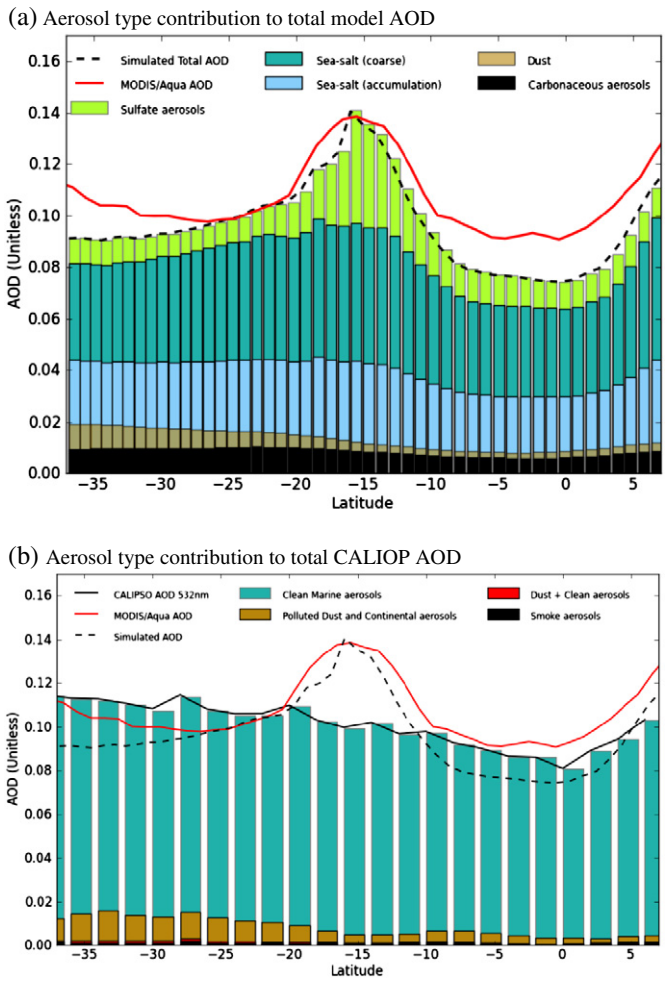

Fig. 11. Aerosol type contribution to total AOD in model and observations. Panel a: model result of 3-year average (01-Oct-2005 to 01-Oct-2008), zonal-mean AOD between 160°E and 174°E (dashed black curve). Panel b: CALIOP analysis of 5-year average (13-Jun-2006 to 26-Aug-2011) zonal-mean AOD between 160°E and 174°E (solid black curve). The aerosol type contribution to total AOD derived from the model and CALIOP aerosol subtyping scheme are displayed through cumulative bar plots in panels a and b, respectively. For comparison, MODIS/Aqua AOD is also reported in both panels by a red curve.

polluted and continental dust (see Appendix A). From pilot reports transmitted to the Wellington Volcanic Ash Advisory Centre, ash observations are more frequent during eruptions, but infrequent at other times. But, at close distance to some volcanoes (Mount Yasur on Tanna Island, summit 405 m), low level ash emissions are often detected by visitors (Dr. Bani's personal communication). In that respect, the presence of ash co-emitted with gas remains uncertain and needs further investigations.

7. The sulfur budget of the tropical Southwest Pacific

As stated in the previous section, volcanoes in MVA and especially Ambrym are key sources determining the aerosol composition of the remote marine boundary layer of the SW Pacific. Since the model gives a reliable representation of the regional climate and aerosol composition, we now use it to assess the influence of regional source, transport and sink processes on the distribution of sulfate aerosols.

7.1. Oceanic and volcanic sources in the sulfur cycle

The Miami Collection (Savoie and Prospero, 1989) includes non-sea salt sulfate (equivalent to model SU) and methanesulfonate (MSA) observations. Their mean surface concentrations at six sites across the SW Pacific are reported in Table 7, in gray shaded rows. The aerosol collection is extensively used in the community to address, among other topics, the role of DMS in the atmospheric sulfur cycle. If the contribution of volcanic sources to SU observations in the Miami Collection is still debated (Dr. Prospero's personal communication), model and field studies suggest that oceanic DMS remains the largest source of SU precursors in regions with pristine tropical air, like Samoa (Savoie and Prospero, 1989; Savoie et al., 1994). Here differences in SU surface concentrations between CTRL and RUN1 are used to investigate the impact of Ambrym on the SU distribution across the monitored stations in the Miami Collection.

As shown by Boucher et al. (2003) and Lana et al. (2011), using different air–sea transfer schemes and oceanic DMS climatology has a large incidence on the simulated sulfur cycle. We address that sensitivity by adding in the GOCART DMS module (Appendix C) a second DMS flux parameterization adapted from Nightingale et al. (2000), using the most recent oceanic DMS climatology described in Lana et al. (2011). Changes in MSA and SU surface concentrations between RUN3 and CTRL help us to evaluate the role of DMS flux parameterization on the Sulfur cycle. In addition to mean changes (Table 7), the seasonal evolution of SU and MSA is examined for three sites located close to the MVA, i.e., New-Caledonia, Norfolk Island and American Samoa (Fig. 12).

First, the new DMS flux parameterization doubles the MSA surface concentrations everywhere (compare RUN3 and CTRL, Table 7 column 3). Compared with CTRL results obtained using the original Liss and Merlivat's (1986) scheme with Kettle et al.'s (1999) database for oceanic DMS, RUN3 seems in better agreement with observations. Due to the increase of DMS, SU surface concentrations are slightly higher in RUN3, i.e., a 30% increase in the tropical belt and about 20% in the subtropics (column 6). CTRL and RUN3 both capture the seasonal cycle (Fig. 12), but RUN3 tends to overestimate summer MSA. By contrast in winter, both CTRL and RUN3 have lower MSA than observed, especially around Samoa suggesting a problem with the DMS source in that region. Running the alternative DMS flux parameterization from Nightingale et al. (2000) using the original Kettle et al.'s (1999) database accounts for only half the increase of DMS (not shown). Overall, the benefit for SU surface concentrations of using new DMS parameterizations is not clear (Table 7) and a large negative bias remains in RUN3 of 55% in Samoa and 39% in New Caledonia.

Turning off Ambrym degassing (RUN1) promotes a large reduction of 56% in SU surface concentrations in New Caledonia, but also a slight reduction in remote places, implying that volcanic species can influence the chemistry of the remote boundary layer in the SW Pacific (contribution of volcanic SU: 7.7% in Rarotonga, 5.5% in Samoa, and 8.5% in Norfolk; see Table 7, column 5). Furthermore, in New Caledonia, the inclusion of Ambrym degassing in CTRL and RUN3 tend to slightly decouple SU from the MSA seasonal cycle (Fig. 12, around April and October). This is also observed in the Miami Collection for that location, with a large decoupling in September and a slight one in April. As expected, by allowing volcanic passive degassing, intra-monthly variability is in much better agreement with measurements (compare monthly deviations in Fig. 12).

7.2. Transport and sinks of volcanic sulfate

As evidenced by the OMI SO_2 burden (Fig. 7, inset), New Caledonia's boundary layer is directly exposed to volcanic gases originating from Ambrym, which can promote the formation of volcanogenic SU aerosols directly over New Caledonia. But more complex processes are involved with volcanic species found in more remote places. There are detailed below.

Fig. 13a and b display respectively the mean SU concentration at the surface and its surface deposition rate including dry and wet deposition. Using the SU difference between CTRL and RUN1 (hereafter Ambrym SU), we can spatially evaluate the mean contribution due to Ambrym degassing (depicted by percent contours in Fig. 15a). Regions of large

Table 7
Observed and simulated mean surface concentrations of methanesulfonate (MSA), non-seasalt sulfate (SU), dust (DU) and sea-salt (SS) at six sites across SW Pacific. Observations from the University of Miami Aerosol Group are given in gray rows for various recording periods (column 2). Contaminated sites due to surf conditions are indicated with bold SS values. DU is derived from Aluminum concentrations using the relation DU = Al/0.08. Model surface concentrations are extracted from the first model level. Observations for low wind speed (<1.8 m/s) are excluded and this threshold value is also applied to the model (Savoie and Prospero, 1989). Model SS and DU concentrations are computed by summing the four and five size bins quantities given by the GOCART aerosol model respectively. Changes in surface concentrations for three sensitivity experiments are indicated in percent of the CTRL run values.

Location	Recording period	MSA [μg/m^3]	SU [μg/m^3]	SU Changes due to:		DU [μg/m^3] (Al/0.08)	SS [μg/m^3]	Changes due to SS scheme
				Ambrym degassing	DMS scheme			
Nauru 0.53°S 166.95°E	*16-Mar-1983 02-Oct-1987*	–	*0.154*			*0.100*	***153.837***	
CTRL		0.021	0.184			0.118	14.563 (Gong)	
RUN1		0.021	0.181	−1.6%		0.118	14.563 (Gong)	
RUN2		0.021	0.184			0.118	26.886 (Jaeglé)	+84.6%
RUN3		0.042	0.237		+28.8%	0.118	14.563 (Gong)	
Funafuti–Tuvalu 8.50°S 179.20°W	*08-Apr-1983 31-Jul-1987*	–	*0.167*			*0.196*	***195.348***	
CTRL		0.016	0.148			0.100	14.753 (Gong)	
RUN1		0.016	0.145	−2.0%		0.100	14.753 (Gong)	
RUN2		0.016	0.148			0.100	28.205 (Jaeglé)	+91.2%
RUN3		0.029	0.192		+29.7%	0.100	14.753 (Gong)	
American Samoa 14.25°S 170.58°W	*19-Mar-1983 31-Mar-1999*	*0.023*	*0.337*			*0.252*	*18.134*	
CTRL		0.011	0.114			0.120	19.980 (Gong)	
RUN1		0.011	0.108	−5.5%		0.120	19.980 (Gong)	
RUN2		0.015	0.127			0.120	35.321 (Jaeglé)	+76.8%
RUN3		0.023	0.152		+33.3%	0.120	19.980 (Gong)	
Rarotonga 21.25°S 159.75°W	*23-Mar-1983 23-Jun-1994*	*0.019*	*0.107*			*0.106*	***76.040***	
CTRL		0.012	0.098			0.246	23.290 (Gong)	
RUN1		0.012	0.091	−7.7%		0.246	23.290 (Gong)	
RUN2		0.012	0.098			0.246	31.768 (Jaeglé)	+36.4%
RUN3		0.021	0.124		+26.5%	0.246	23.290 (Gong)	
New Caledonia 22.15°S 167.00°E	*23-Aug-1983 23-Oct-1985*	*0.020*	*0.436*			*0.171*	*31.862*	
CTRL		0.013	0.223			0.636	30.155 (Gong)	
RUN1		0.013	0.143	−55.9%		0.636	30.155 (Gong)	
RUN2		0.013	0.223			0.636	38.577 (Jaeglé)	+4.2%
RUN3		0.028	0.264		+18.4%	0.636	30.155 (Gong)	
Norfolk Island 29.08°S 167.98°E	*27-May-1983 21-Feb-1997*	*0.025*	*0.273*			*0.841*	*25.998*	
CTRL		0.012	0.190			1.011	29.568 (Gong)	
RUN1		0.012	0.175	−8.5%		1.011	29.568 (Gong)	
RUN2		0.012	0.190			1.011	29.896 (Jaeglé)	+1.1%
RUN3		0.026	0.226		+18.9%	1.011	29.568 (Gong)	

surface amounts of SU are generally located close to sources of volcanic and anthropogenic origins. The fraction associated with Ambrym exhibits a typical pattern matching the SPCZ axis tilt (hatched box in Fig. 13b). The mean wind pattern and sulfate mixing-ratio at the trade wind inversion altitude (750 hPa) are also reported in Fig. 13d. The wind pattern reflects the low level convergence of moist tropical air along the SPCZ, and as evidenced by patterns of Ambrym SU in Fig. 13a, b and d, horizontal transports between the lower and free troposphere dictate the east-west elongated distribution of Ambrym volcanic species across the SW Pacific.

Furthermore, as evidenced in Fig. 13c, obtained using cross-averaged sink/source quantities of Ambrym SU along the SPCZ axis, wet deposition and oxidation in aqueous phase are definitely major processes determining (respectively) volcanic SU sinks and sources in the SPCZ. However, east of the date line, the in-air oxidation of SO_2 emitted from Ambrym remains one of the most important chemical pathway for the generation of Ambrym SU, indicating that SU production does not originate from the lower troposphere (where its moist and cloudy air provides the most efficient pathway for oxidation; see Section 4.4) but from the free troposphere with drier conditions. Therefore, the simulated Ambrym SU found in the remote boundary layer of tropical islands, like Rarotonga and Samoa, results from long-range transport of SO_2 above the trade inversion.

In contrast, downwind from the source toward the Maritime continent, the in-cloud oxidation of SO_2 dominates the formation of Ambrym SU in this region characterized by moist tropical air, while the in-air

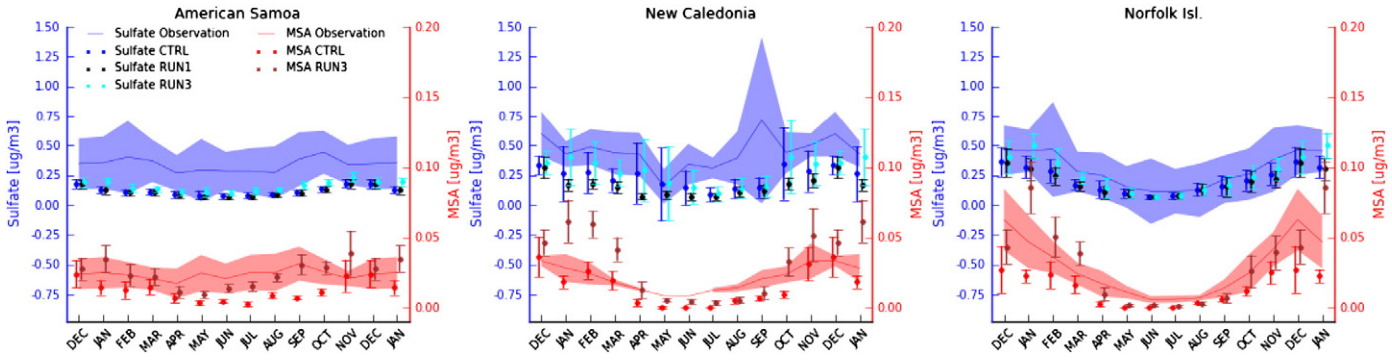

Fig. 12. Comparison of simulated and observed monthly-mean surface concentrations of non-seasalt sulfate (SU; blue curves) and methanesulfonic acid (MSA; red curves) at 3 sites monitored by the University of Miami Aerosol Group. Dots and error bars represent simulated means and standard deviations respectively. Observed means and standard deviations are shown with lines and filled curves respectively. Changes of sulfate surface concentrations due to changes in sources of DMS and volcanic sulfur are superimposed. They are given by the CTRL experiment, RUN1 (no Ambrym degassing) and RUN3 (revised parameterization and climatological data for DMS; see Table 5). Data, location and recording periods are summarized in Table 7.

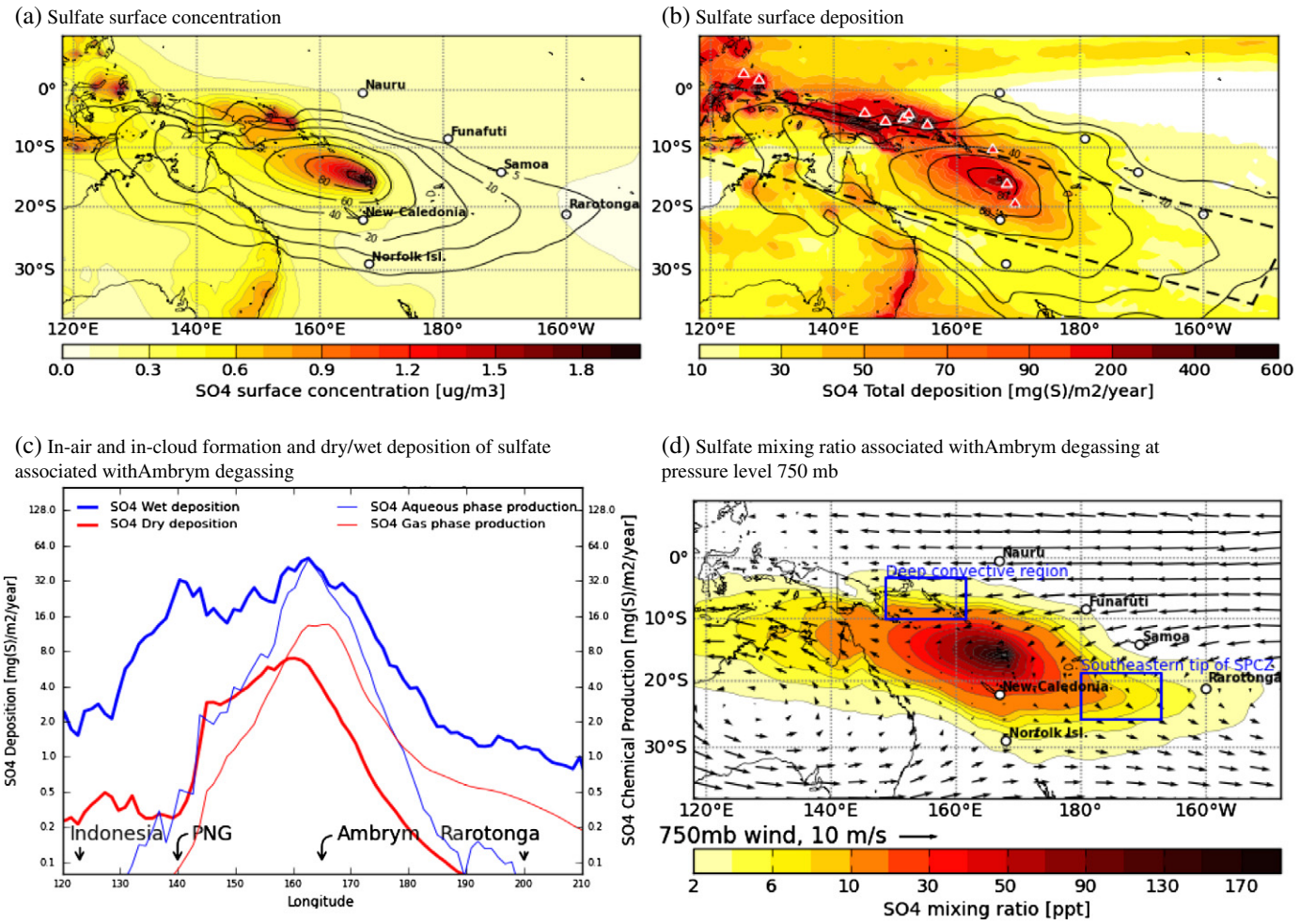

Fig. 13. Upper panels (a) and (b) respectively provide surface concentration and wet/dry deposition of SU aerosols, with contribution from Ambrym degassing in contours. Panel (c): sources and sinks of SU associated with Ambrym degassing along the SPCZ using cross-box averaged values in the box drawn on panel (b). Panel (d): mixing ratio of SU associated with Ambrym degassing and model horizontal wind vectors at 750 mb. Two regions defined in the budget analysis are displayed in blue, i.e., a deep convective region (Solomon Sea) and a more stable region in the southeastern tip of the SPCZ.

oxidation is four times less efficient. At the westernmost longitude of PNG (130°E), the Ambrym SO_2 is fully oxidized, but Fig. 13d indicates that part of Ambrym SU is advected farther into the Maritime continent by the large scale circulation on the northern side of the Australian anticyclone. This implies that the sulfate aerosol originating from passive volcanic degassing in the MVA is exported outside the South Pacific and may contribute (with Indonesian wildfires) to the SU budget over Southeast Asia. Yet, studies of this region have not considered the possibility of remote volcanic influence (e.g., Trivitayanurak et al., 2012). On the other hand, the Ambrym SU patterns in Fig. 13b also suggest that the sharp topography and wet climate of PNG mainland act to form an efficient barrier against the equatorward spreading of volcanic species originating from Vanuatu.

7.3. Closed sulfate budget

After describing how passive volcanic degassing sources, tropical dynamics and cloud processes mediate the distribution of Ambrym SU, we now turn to the driving tendencies of Ambrym SU in the vertical column. The sulfate evolution equation (the same applies for SO_2) can be expressed as:

$$\frac{\partial SU}{\partial t} = CHEM + ADV + DIFF + VMIX + CONV + WET, \quad (4)$$

where CHEM is the source-sink term due to chemical reactions implemented in GOCART; ADV the lateral and vertical advections; VMIX the vertical turbulent diffusion and dry deposition, CONV the sub-grid scale convective transport of tracers; DIFF the lateral diffusion; and WET the sink/source term due to rain scavenging (rainout + washout) and re-suspension after evaporation (Section 4.7). DIFF is relatively small and is neglected in the budget analysis. When averaged over the 2006–2008 period, the budget equation provides the climatological balance expressed as:

$$0 \approx \overline{CHEM} + \overline{ADV} + \overline{DIFF} + \overline{VMIX} + \overline{CONV} + \overline{WET}. \quad (5)$$

This budget is analyzed at two contrasted regions situated at near equal distance from the source and denoted by rectangle boxes in Fig. 13d. One is located over the Solomon Sea, a region characterized by deep convection (low OLR, see Fig. 2) and large in-cloud oxidation of Ambrym SO_2. The second is at the southeastern tip of the SPCZ, east of the date line, where the in-air oxidation drives the Ambrym SU production. Time and box averaged vertical profiles of SO_2 and SU concentrations are given in Fig. 14, while sources and sinks terms are shown in Fig. 15. Fig. 15 a confirms that advection is the largest source of SU within the lower troposphere in the SPCZ downwind from the volcano, but it is balanced by vertical mixing in the boundary layer and also convective transport. Just below the base of the free troposphere (750 hPa), turbulent vertical mixing is the primary mechanism involved in the venting of

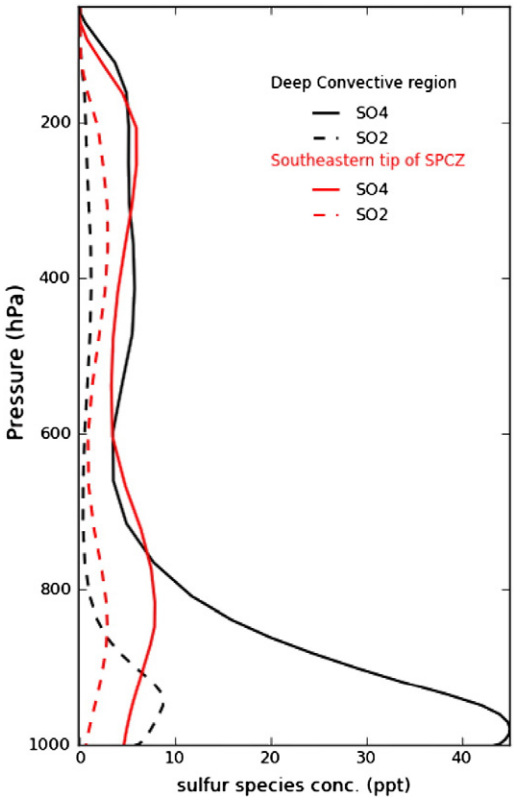

Fig. 14. Vertical profiles of box averaged SO_2 and SU concentrations over the deep convective region in the Solomon Sea (black lines) and the southeastern SPCZ region (red lines). The exact locations are given in Fig. 13d). Time averaging is done for the period 01-Oct-2006 to 01-Oct-2008.

SU, while in mid-troposphere deep convection accounts for the replenishment of SU, eroded by advection and by wet scavenging. As shown in Fig. 14, a small part of volcanic species (here SU) can reaches the tropopause. It follows that the passive degassing may influence the stratosphere composition. Over the Solomon Sea, at 1000 km from the source, chemical reactions still play a moderate role in the SU budget, specifically in the cloud layer at 900 hPa. Throughout the vertical column, aerosol wet removal processes by liquid and frozen hydrometeors (Appendix C) play a strong control in the depletion of SU.

In the southeastern box (Fig. 15b), SU advection (i.e., the lateral component; not shown) is dominant above the boundary layer up to mid-troposphere (this also applies to SO_2; not shown) and is balanced by wet deposition processes. Chemical production of SU (in the gas-phase) occurs in the upper troposphere (200 hPa) at the same rate than in the lower troposphere. This highlights a source of Ambrym SU precursors near the tropopause, fueled by the deep convection over warm waters and transported poleward in the upper troposphere by the Hadley Cell circulation. Indeed, SO_2 concentrations in the upper troposphere are twice those found in the convective box (compare the red and black curves for SO_2 in Fig. 14) and a similar budget analysis conducted on SO_2 highlights the upper source of SU precursors by lateral advection (not shown). Interestingly, and in contrast to the Solomon Sea region, wet deposition is the main mechanism explaining the replenishment of SU in the southeastern boundary layer. This is due to re-suspension of SU following the evaporation of thin rain droplets.

7.4. Aerosol microphysics

As pointed out by the budget equation (and also suggested in previous sections), the fate of chemical tracers critically relies on the distribution of modeled rainfall and on the treatment of wet deposition. As for subgrid-scale convective transport (Hoyle et al., 2011), it is unclear that wet deposition (at grid- and sub-grid scales) is adequately represented in global and regional climate models (Textor et al., 2006; Croft et al., 2012). Usually in global models, the wet scavenging efficiency of tracers (ranging from 0 to 100%) is tuned to adjust the tracer lifetime (e.g., Balkanski et al., 1993; Fan and Toon, 2011). In addition, the

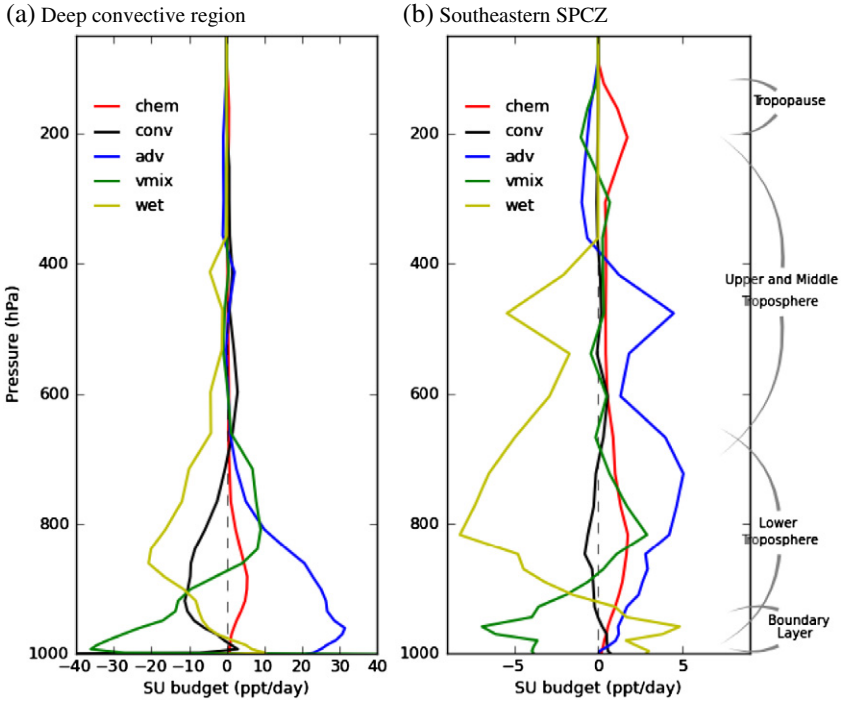

Fig. 15. Vertical profiles of box averaged SU budgets over (a) the deep convective region in the Solomon Sea and (b) the southeastern SPCZ region (exact locations in Fig. 13 d). Time averaging is done for the period 01-Oct-2006 to 01-Oct-2008.

re-suspension of soluble tracers due to evaporation of rain droplets is not included in WRF-Chem public releases (for resolved precipitation). This absence of reversibility in aerosol wet removal was recently invoked by Saide et al. (2012) to explain a model aerosol underestimation in the southeastern Pacific stratocumulus cloud deck.

Our implementation in WRF-Chem of a new wet removal treatment inherited from the work of Giorgi and Chameides (1986) and Balkanski et al. (1993), gives us the opportunity to address tracer sensitivity to wet deposition, including the debatable question of aerosol re-suspension. It should be emphasized that the wet deposition scheme only considers the washout, rainout and re-suspension of aerosols associated with grid-scale precipitation and uses a scavenging efficiency of 100% for soluble gases and aerosols (Appendix C).

The sensitivity of simulated total AOD to aerosol wet processes is investigated through two additional experiments. RUN4 and RUN5 are similar to CTRL but without wet deposition and without aerosol re-suspension respectively. The results are displayed in Fig. 16. MODIS AOD and simulated AOD for the other experiments are also shown for comparison. Table 8 summarizes SO_2 and SU budgets for each experiment. Fig. 16 reveals that the wet deposition treatment strongly controls the aerosol burden (compare AOD between RUN4 and CTRL) and exerts a larger impact than any improvement for sources like DMS for SU precursors (RUN3) or SS (RUN2). Furthermore, as indicated by the AOD difference between RUN5 and CTRL, the re-suspension of aerosols plays also a key role in the SU distribution both in the tropics and subtropics belts. However, the importance of re-suspension effect to AOD appears slightly larger toward the subtropics south of 10°S, as pointed out earlier using the budget equation. In terms of sulfur cycle, this source of SU released from evaporating droplets is equivalent to about twice the contribution due to Ambrym volcanic degassing (see in Table 8 the SU burden differences between RUN5/RUN1 and CTRL).

Table 8
WRF-Chem budgets for sulfur species (sulfur dioxide and sulfate) in each sensitivity experiments (01-Oct-2006 to 01-Oct-2008).

	CTRL	RUN1	RUN3	RUN4	RUN5
SO_2, Sources (kT S day^{-1})					
Emissions:					
Anthropogenic	6.1	6.1	6.1	6.1	6.1
Volcanic degassing	8.6	6.4	8.6	8.6	8.6
Biomass burning	0	0	0	0	0
DMS	4.6	4.6	9.3	4.6	4.6
Total SO_2 source	19.3	17.1	24.0	19.3	19.3
SO_2, Sinks (kT S day^{-1})					
Oxidation in gas phase	2.0	1.7	2.3	2.3	2.0
Oxidation in aqueous phase	3.1	2.6	3.6	4.4	3.1
Dry deposition	8.5	7.2	9.4	8.7	8.5
Wet deposition	1.9	1.6	2.2	0	1.9
Total SO_2 sink	15.5	13.1	17.4	15.4	15.5
SO_2, burden (kT S)	14.8	12.6	16.3	16.3	14.8
Difference relative to CTRL (kT S)	0	−2.3	1.5	1.5	0.0
SO_2, lifetime (day)	0.8	0.7	0.7	0.8	0.8
Sulfate, sources (kT S day^{-1})					
Production in gas phase	2.0	1.7	2.3	2.3	2.0
Production in aqueous phase	3.1	2.6	3.6	4.4	3.1
Wet resuspension	2.0	1.8	2.2	0	0
Total sulfate source	7.1	6.1	8.1	6.7	5.1
Sulfate, sink (kT S day^{-1})					
Dry deposition	0.6	0.6	0.7	1.0	0.5
Wet deposition	5.4	4.6	6.1	0	4.1
Total sulfate sink	6.1	5.2	6.8	1.0	4.6
Sulfate, Burden (kT S)	31.1	28.6	33.7	84.4	27.0
Difference relative to CTRL (kT S)	0	−2.5	2.6	53.3	−4.0
Sulfate, lifetime (day)	4.4	4.7	4.1	12.6	5.3

8. Discussion

8.1. On the distribution of volcanic species

The combination of satellite observations and WRF-Chem/GOCART solutions clarifies the role of passive volcanic degassing and SPCZ dynamics on the aerosol composition of the SW Pacific. Our results complete the works of Jones and Christopher (2011) on the origin of volcanic sulfur species in the region, but outline in great detail the fate of these species. Our assessment of the MVA passive degassing contribution to aerosol composition is based on a 2006–2008 study of Ambrym, characterized by a mean SO_2 emission rate of 5.4 kT d^{-1}. This source represents 30% of the regional SO_2 emission from volcanoes composing the MVA and eastern Indonesia and is equivalent to half of the regional anthropogenic emission, including that of Australia. Using simulated and MODIS AOD as a proxy for aerosol burden, it appears that the Ambrym SO_2 rich plume allows the formation of large amounts of acidic SU aerosols, giving rise to an elongated layer of scattering particles downwind of the volcano to Papua New Guinea (1500 km away) and farther into the Maritime Continent. Since the model provides a reasonable representation of the regional climate and aerosol distribution, we are able to expose the very strong link between distribution of volcanic species and SPCZ dynamics, in terms of chemical and transport pathways.

In the lower troposphere, vertical mixing by turbulence and deep convection governs the vertical motion of volcanic volatiles above the trade inversion. Aloft, the subtropical anticyclones located over Australia and the South Pacific dictates their long-range transport. The flow on the northern side of the Australian anticyclone transports SU and SO_2 through the moist tropical air with large cloudiness. There, the conditions are very efficient to totally deplete SO_2 through oxidation in the aqueous phase. By contrast and since conditions are drier and more favorable to delay the production of SU in the subtropical region, the southeastern branch of the South Pacific anticyclone transports larger proportion of SO_2 in the volcanic mixture. In addition, the very deep convection in the tropics directly supplies the upper branch of the Hadley Cell with surface volcanic volatiles. Some of the transport of volcanic species toward the southeast Pacific is thus achieved through the poleward motion of tracers in the Hadley Cell.

Finally, the chemical production of aerosols and their wet removal are also strongly linked to the microphysical and macrophysical properties of clouds in the SPCZ, which points out to the importance of adequately reproducing its features in model simulations (rain rate, hydrometeor phase and size, fractional cloudiness, etc.).

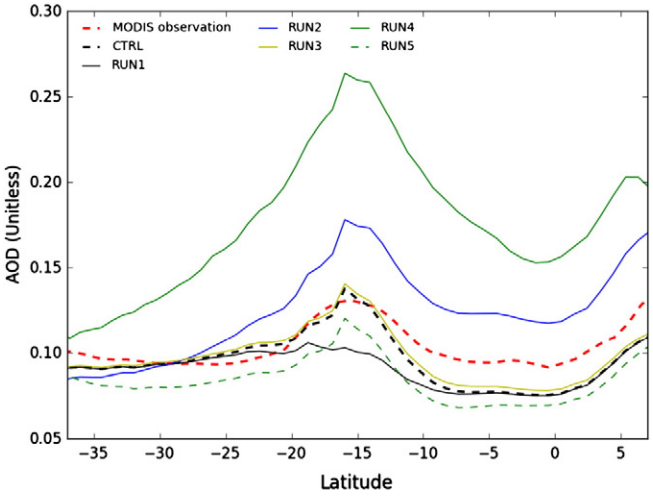

Fig. 16. Zonal and time mean AOD between 160°E and 174°E and 01-Oct-2005 and 01-Oct-2008, computed offline using FlexAOD with outputs from six experiments detailed in Table 5. The observed MODIS AOD (red line) is given for comparison. Note that all simulated AODs are subsampled in coincidence with valid MODIS observations.

8.2. Impacts of passive volcanic degassing

Our model results indicate that Ambrym volcano act as a remote source of volcanogenic species in neighboring countries, but also in remote places which might initially appear unlikely (East Indonesia, Norfolk Isl., Rarotonga). This is due to the large scale-circulation and dynamics of the SPCZ. The dispersion pattern detailed in this study for Ambrym is likely to be the same for others volcanoes of Vanuatu, but will likely differ for those of PNG located in the deep convective region, as the circulation pattern over PNG and Vanuatu are different (Fig. 13d).

As indicated by Fig. 14, significant amounts of sulfur species can be pumped up to the upper troposphere and lower stratosphere by active convections. Once lofted in the stable stratosphere, Ambrym's SU becomes a long-lived stratospheric aerosol, having the potential to provide more long lasting effect on the Earth radiative budget (Graf et al., 1997). Through this process, the passive volcanic degassing in the MVA may be another source of sulfur species for the stratosphere, which comes in addition to emissions from small and high erupting volcanoes (see Vernier et al., 2011).

Our cross-examination of the AOD in the cloudy SPCZ clearly indicates that the Ambrym's SO_2 source led to a significant and long-lasting perturbation of the tropospheric aerosol extinction, with AOD anomaly in the range [0.03–0.04] (see Fig. 11). Careful estimations of the direct (and indirect) aerosol radiative forcing due to Ambrym remain to be done (i.e. Yuan et al., 2011). One climatic feature of the region is its high cloudiness, which immediately raises the question of the perturbation of cloud properties by aerosols. With SO_2 emission flux twice compared to Kilauea (~5.4 kT d^{-1} against ~2 kT d^{-1} in quiescent period), Ambrym is expected to drive similar volcanic aerosols forcing on the local climate as investigated in Yuan et al. (2011) and Ebmeier et al. (2014) for the Hawaiian volcano.

Volcanic degassing also affects air chemistry as it supplies volcanic oxidants that change the natural oxidation capacity of the background air. As the Ambrym plume includes substantial amounts of reactive Bromine BrO (Bani et al., 2009), its venting and long-range transport in the upper troposphere (suggested by the simulated SO_2 fate) would likely affect the tropical ozone budget (Gerlach, 2004; von Glasow et al., 2004) and oxidation mechanisms of biogenic gases like DMS in the remote and pristine marine boundary layer (Faloona et al., 2010; Gray et al., 2010). Therefore, poor SPCZ representation and underestimation of volcanic degassing emissions for aerosol precursors and oxidants would limit the capacity of models, even with sophisticated volcanic plume chemistry, to predict the geochemical cycle of key atmospheric species in the SPCZ region.

In Vanuatu, Ambrym inhabitants are directly exposed to chemically active plumes, with health issues such as skin burning due to acid rain and dental fluorosis due to large exposure to deposited fluoride (Cronin and Sharp, 2002; Allibone et al., 2010). During the recent 2012 Pandora research cruise (Eldin et al., 2013), we measured acid rain in the Solomon Sea downwind from Ambrym that was consistent with our forecast (using WRF) of a volcanic plume reaching the region. The simulated plume also explained the occurrence of acid rain events in northern New Caledonia with pH reduced to 3.5 recorded near the Koniambo Nickel SAS industrial complex. Such scientific observations and anecdotal evidence substantiate the potential role of Ambrym degassing on the boundary layer chemistry of New Caledonia and in the remote ocean (see deposition maps Fig. 13). Environmental consequences and practical applications are diverse. The inclusion of volcanic aerosols in air quality surveys would help assessing the oxidizing capacity of air. It would also allow us to describe their potential contribution in forestry and agriculture damage or their role in biogeochemistry of surface waters, including their potential contribution to the natural acidification of exposed coral reefs.

In the larger Pacific region, the link between volcanic ashes and ocean fertilization has been established in the context of eruptive activity (Langmann et al., 2010). In the surrounding of the Vanuatu volcanic arc, a similar relation may exist, as evidenced by satellite observations during short erupting events (see Appendix A) and deserves ongoing research. But the mixture of volcanic gases in Ambrym plume may also impact ecology and the food chains, since recent studies have pointed out the key role of reactive halogen in enhancing the oxidation and deposition of volcanogenic Hg species near source (Von Glasow, 2010; Roberts et al., 2014). Across the SW Pacific, elevated MeHg (Methylmercury) concentrations were found in seafood products (Dr Anne Lorrain's personal communication from the Marine Environmental Sciences Laboratory (LEMAR-IRD)), pending further investigations on the role of the volcanic plume chemistry in the MVA.

8.3. Assessing observational needs and errors

In this study, we carefully identified some model flaws associated with horizontal resolution (e.g., smoothing of island-scale features), precipitation rate (summer overprediction), physics/chemistry coupling or sulfur chemistry (e.g., specified background fields of reactants, fixed pH, no heterogeneous chemistry, external mixing assumption). Nevertheless, the simulations produced by WRF-Chem/GOCART are compelling and promote the discussion on measurement issues.

Our capacity to understand the role of passive degassing is limited by the paucity of long-term observations of gas composition and fluxes. Uncertainties and accessibility issues impairing volcanic inventories have been recently reviewed (Oppenheimer et al., 2011). As a result of limited in-situ observations, top-down methods have become a valuable support to obtain reliable estimates. However, our study and several other investigations (Bani et al., 2012; McCormick et al., 2012) reveal serious issues of spurious variability and underestimation by satellite observation due to irregular sampling, cloud contamination and sensor detection limits. Therefore, long-term ground observations remain needed to adequately constrain top-down budgets.

Beside satellite sampling issues, the cross-evaluation of model and observations allowed us to pinpoint the poor inventory used for biomass-burning emission in southwest Indonesia. It evidenced deficiencies in satellite methods commonly used to retrieve aerosol compositions. A most outstanding example is the misclassification of sulfate aerosols by the CALIOP CAD algorithm. Obviously, the CAD algorithm fails to identify volcanic SU aerosols freshly released in the lower troposphere, probably as a consequence of inaccuracies in the look-up table based on AERONET observations (Appendix A). This result suggests that the characteristics of typical volcanic and sulfur-rich aerosol mixtures need to be further documented using Lidar, photometer instruments and aerosol sampling. Clearly, aerosol misclassification, cloud contamination, and sensor detection limits remain fundamental barriers to assess vertical aerosol distribution through satellite observation.

8.4. Improving aerosol parameterizations

8.4.1. Sea salt generation

As detailed, the volcanic degassing from MVA occurs in the MABL, where gases are in contact with SS particles. In future investigations addressing their environmental impact with volcanic plume chemistry models, accurate representation of SS particles warrant special attention since their surface may promote overlooked heterogeneous reactions. Conclusion of our tests of two SS generation schemes (CTRL and RUN2) is indicative of the weakness of aerosol models in reproducing SS mass burdens, as investigated by Textor et al. (2006, 2007). According to Jaeglé et al. (2011), the SS parameterization based on SST gives better prediction of the SS mass concentration in GEOS-Chem over warm waters. In contrast, we found larger SSC mass concentrations and quite larger SS AOD in the tropical belt with our model setup based on WRF-Chem, using the same SST as in Jaeglé et al. (2011).

A better agreement with observations and empirical laws is found with the original Gong (2003) source function (Fig. 6). Clearly, the sensitivity of SS burden and AOD to model physics and aerosol treatments needs to be investigated further, but this topic is beyond the scope of this study.

8.4.2. DMS flux and interaction with volcanic oxidants

The sulfur cycle sensitivity to the oceanic DMS climatology and DMS flux parameterization is also large in GCMs, as shown at global scale in Boucher et al. (2003). The default database for oceanic DMS and the current DMS scheme in WRF-Chem do not include the most recent oceanic DMS climatology (Lana et al., 2011) or recent advances in DMS flux parameterization (Nightingale et al., 2000). We included these updates and tested their influence on SU and MSA surface concentrations by comparing with the Miami Collection.

In the SW Pacific, the latest oceanic DMS climatology and DMS air–sea transfer function suggested by Lana et al. (2011) improve surface concentrations of MSA compared with observations, but seasonal biases remain. These biases are still unclear and may be due to the paucity of oceanic DMS observations in the region, as signaled in Lana et al. (2011). But model errors can contribute as well, through a wet deposition bias in warm summer (too low) for example. In addition, the model does not include the role of key oxidants involved in the fate of DMS, like reactive BrO released in volcanic plumes (Bani et al., 2009). Their potential role in DMS oxidation signaled by many authors (von Glasow et al., 2004; Faloona, 2009; Gray et al., 2010) may likely be exacerbated in remote regions polluted by volcanic species.

Finally, our new DMS flux parameterization doubles the SO_2 biogenic source strength, which becomes far larger than Ambrym emissions. However, the relative impact on SU burdens by DMS fluxes is weaker because of lower efficiency of sulphate formation. This is demonstrated by computing the formation efficiency of SU (i.e., relative SU burden divided by relative source strength; Graf et al., 1997). Specifically, the increase of SO_2 biogenic source from 4.6 to 9.3 kT(S) d^{-1} (Table 8) due to the new DMS flux parameterization produces an increase from 31.1 to 33.7 kT(S), i.e., a net increase of 2.6 kT(S) of SU burden in the model domain. This is similar to the 2.5 kT(S) SU burden due to Ambrym SO_2 degassing of 2.7 kT(S) d^{-1} (Table 8). Using the values, Ambrym volcanic efficiency is 1.1 compared with 0.5 for the DMS source. Volcanic passive degassing has thus a larger relative impact on air chemistry and climate than DMS, presumably due to the higher altitude of emissions (Graf et al., 1997).

8.4.3. Re-suspension in aerosol microphysics

Uncertainties in modeling the wet deposition of soluble tracers provide the largest source of error in simulated AOD (see Fig. 16, RUN4 and RUN5). Using SU and SO_2 budgets in WRF-Chem, we show that the absence of wet removal result in a very large SU burden of about 84.4 kT(S), 2.7 times the SU burden computed in CTRL, implying that improvement in the wet deposition of soluble tracers is crucial in the SPCZ.

An interesting result is the influence of aerosol re-suspension, which apparently plays a significant role in the vertical redistribution of soluble atmospheric species from the free troposphere to the marine boundary layer in regions of large-scale subsidence. As shown in the vertical profile of the wet deposition tendency term (Fig. 15b), this process provides a dominant source of volcanic SU in the southern tip of the SPCZ and drives the supply of volcanic SU in the remote marine boundary layer. Therefore, this complex aerosol microphysical process exerts a strong control on the cycling of sulfur species and explains the supply of volcanic SU in remote places like Samoa, Rarotonga or Norfolk. Similarly, it may affect the redistribution of volcanic oxidants, resulting in spatial heterogeneities in the remote marine boundary layer, in relation with rain and cloud properties. As suggested by Saide et al. (2012), such irreversibility of aerosol wet removal can no longer be dismissed. This is particularly important in the MVA region for SU burden, since we demonstrated that its omission is equivalent to neglecting a major SU source like passive volcanic degassing. This result confirms that more attention should be devoted in the future to the reliable representation of aerosol wet scavenging processes in global and regional model.

8.5. Correcting AOD estimation

Our study uses the original AeroCom inventory for non-eruptive degassing, but this database is significantly improved by adopting the degassing rate of 5.4 kT(SO_2) d^{-1} indicated by Bani et al. (2012) for Vanuatu. As a result, there is a significant improvement between WRF-Chem/GOCART and GSFC/GOCART for AOD (see Fig. 10). The global GSFC/GOCART model shows a large bias in volcanic sulfate distribution of the MVA, reducing our confidence in this model's radiative budget at regional and global scales for that version (G4P0). On the other hand, our regional model suffers from the non-inclusion of eruptive sources in PNG that appears to underestimate the SU burden downwind from PNG (this is also evidenced in the GSFC/GOCART seasonal cycle). This means that accurate emissions from both erupting and continuous degassing volcanoes need to be considered to give a more reliable picture of the distribution of volcanic species in the SW Pacific. This probably is a mandatory step before investigating their direct and indirect radiative forcing.

Regardless of the quality of aerosol source inventories, large uncertainties exist in present global aerosol simulations, due to the parameterization of atmospheric aerosol processes (Textor et al., 2007). AOD is a valuable proxy to evaluate the aerosol burden and is commonly used to assess the performance of aerosol simulations. But improvements in methods and assumptions of aerosol properties used to calculate AOD (online or offline) are crucial. This is a mandatory task for model-data comparison of optical properties.

While using a similar aerosol and chemistry module, our model AOD (Fig. 10b) sharply contrast with that of the global GSFC/GOCART model (Fig. 10c) using offline meteorological fields of the Goddard Earth Observing System (GEOS). Since sea salt particles dominate the aerosol mixture in the remote marine boundary layer (Fig. 11 a and b), their inaccurate representation of sea salt explains the large negative bias over the ocean, as seen by comparing Fig. 10c and a or b. The representation of sea salt properties, including mass concentrations, size distributions and optical properties is a major source of uncertainty as illustrated by the vast literature on this subject. By revising size parameters for the particle size distributions of SSA and SSC in the GOCART sea salt module (Table B1), we could identify the origin of discrepancies and correct some of the bias.

Specifically, GSFC/GOCART AOD for each aerosol type is calculated using a look-up-table of mass extinction efficiency ($ß$) by assuming that each aerosol type follows a size distribution with parameters given in Table B1. In GSFC/GOCART, dry effective radii (r_{eff}) values for SSA and SSC are consistent with the OPAC database but they remain larger than those suggested by recent observations (Jaeglé et al., 2011) and used in this study. Since assumptions for particle size distributions strongly determine the mass extinction efficiency $ß$ (Appendix B and Fig. B1 for SSA and SSC), larger values of r_{eff} for SSA and SSC produce lower $ß$ values, explaining why GSFC/GOCART AOD in G4P0 (calculated using Eq. (B.6)) is systematically low.

Another problem is the fractioning of SS mass concentrations given by GOCART for use in the SSA and SSC AOD calculation. Four mass size bins are considered in GSFC/GOCART (Chin et al., 2002). We show (see Fig. 6) that a more reliable AOD computation for SSA and SSC is obtained by discarding two size bins characterized by giant and ultra giant SS aerosols (dry effective radii $r_{eff} > 0.4$ μm and $r_{eff} > 5$ μm respectively). This is consistent with recent recommendations (Jaeglé et al., 2011) and also with the remarks made by several authors that AOD is too high for sea salt in WRF-Chem applications, which they usually correct using scale factors in the SS generation schemes (Saide et al., 2012).

Table B1
Particle density and dry size parameters (geometric mean radius r_g, standard deviation σ_g, effective radius r_{eff} and affective variance υ_{eff}) in lognormal dry size distributions for sulfate (SU), organic carbon (OC), black carbon (BC) sea-salt accumulation (SSA) and coarse mode (SSC). The parameters used in this study are in the gray shaded rows. Size parameters based on OPAC (Hess et al. 1998), used in GSFC/GOCART and those suggested by Chin et al. (2002) or Jaeglé et al. (2011) for sea-salt are given for comparison.

	Density	r_g	σ_g	r_{eff}	υ_{eff}
SU	1.70	0.069	1.60	0.12	0.25
OPAC	1.70	0.069	2.03	0.25	0.65
Chin et al., 2002	1.70	0.069	2.03	0.25	0.65
GSFC GOCART	1.70	0.069	2.03	0.25	0.65
OC	1.80	0.064	1.60	0.12	0.25
OPAC	1.80	0.021	2.24	0.11	0.92
Chin et al., 2002	1.80	0.021	2.20	0.09	0.86
GSFC GOCART	1.80	0.021	2.24	0.11	0.92
BC	1.00	0.020	1.60	0.04	0.25
Chin et al., 2002	1.00	0.012	2.00	0.04	0.62
OPAC	1.00	0.012	2.00	0.04	0.62
GSFC GOCART	1.00	0.012	2.00	0.04	0.62
SSA	2.20	0.166	1.50	0.25	0.18
OPAC	2.20	0.209	2.03	0.73	0.65
Jaeglé et al., 2011	2.20	0.085	1.50	0.13	0.18
Chin et al., 2002	2.20	0.228	2.03	0.80	0.65
GSFC GOCART	2.20	0.209	2.03	0.73	0.65
SSC	2.20	0.464	1.80	1.10	0.41
OPAC	2.20	1.750	2.03	6.13	0.65
Jaeglé et al., 2011	2.20	0.401	1.80	0.95	0.41
Chin et al., 2002	2.20	1.640	2.03	5.73	0.65
GSFC GOCART	2.20	1.750	2.03	6.13	0.65

9. Conclusion

The convective activity of the SPCZ covers the MVA, where the tropospheric emission of sulfate precursors due to passive volcanic degassing is larger than anthropogenic sources and similar to other natural sources (DMS emissions). In this study, simulations of sulfur gases and aerosol concentrations from emissions by the Ambrym volcano, a major MVA volcano, are made with WRF-Chem/GOCART, a coupled meteorological-chemistry model, and thoroughly evaluated using satellite and surface observations. Our sensitivity tests and cross-examination results provide a robust understanding of the role of both the Ambrym volcano and its environment in the regional atmospheric sulfur budget. Several key conclusions can be drawn:

1. SPCZ dynamics and its cloud and precipitation properties dictate the fate of volcanic sulfur species through advection, turbulent mixing, and chemical and aerosol microphysical interactions. The most noticeable effect of the Ambrym volcano degassing on the aerosol burden appears through a long-lasting enhancement of the aerosol extinction in the lower troposphere, with a mean regional AOD anomaly in the range [0.03–0.04],
2. Due to the combination of vertical convection in the Tropics and the large-scale horizontal circulation, a significant amount of volcanic species are dispersed across the South Pacific, with distinct transport pathways: the Ambrym volcano acts as a remote source for the aerosol background not only over PNG and East Indonesia, but also for the boundary layer over the Southeastern Pacific, due to the resuspension of volcanogenic sulfate aerosols from evaporating droplets. and
3. The Ambrym volcano is likely involved in the formation of long-lived stratospheric sulfate aerosols, since small amounts can reach the tropopause. The same could apply for the other passive degassing volcanoes in the Melanesian (and Indonesian) volcanic arcs.

The physical setting and new and adjusted model parameterizations implemented in WRF-Chem/GOCART provide an accurate chemical weather representation that allows the identification of biases both in model outputs and satellite data. We have used diagnostic tools for WRF-Chem/GOCART aerosol modeling, FlexAOD for AOD calculation and satellite observations for aerosol classification, which allowed us to investigate and sometimes correct model errors. Our model performance is limited by:

1. Poor source inventories for the regional context (DMS climatology and biomass-burning inventory),
2. Large sensitivity to model treatments for gas (DMS) and aerosol (sea salt) surface emission (fluxes depend critically on air–sea parameterizations and particles size distribution), and
3. Large uncertainty on aerosol removal mechanisms (sub-grid and grid-scale wet scavenging parameterization and aerosol resuspension).

Simulated and observed AOD provided a very valuable metrics, and we used them to determine the error bar of our results by conducting sensitivity experiments on specific model-treatments for sources and sinks. Assumptions in the AOD calculation for sea salt aerosols, key players in the aerosol extinction over the MVA, also limit the simulated AOD performance. As investigated by comparing our model results with those from GOCART/GSFC, inadequate size parameters for fine and coarse sea salt aerosols can lead to incorrect AOD levels.

Severe limitations were pointed out in satellite observations, limiting their use in tracking tropospheric volcanic plumes and in retrieving SO_2 fluxes. They are:

1. Too low sensor detection capability or weaknesses in aerosol identification algorithms for the CALIOP/CALIPSO (lidar). Obviously, incorrect AODs are reported from the CAD algorithm in context of sea salt mixed with (misclassified) fresh volcanogenic sulfate particles, but that problem still requires future investigations, and
2. OMI volcanic SO_2 fluxes are underestimated by 50% over the Vanuatu. The OMI bias has been identified in the study using similar OMI detection limit and irregular sampling in simulated SO_2 mass burden. This is consistent with ground field studies in the region.

Finally, by giving a more accurate picture of the fate of SO_2 in Ambrym's volcanic plume, we can ask ourselves what role the Ambrym volcano may play on its regional environment, through the perturbation of climate (direct and indirect forcing of sulfate aerosols), change in the oxidizing capacity of air (through the formation of BrO and ClO), deposition of acidic species (i.e. HCl) and highly toxic elements (i.e. Hg), or the release of key micronutrients at the ocean surface. All these overlooked environmental issues need further dedicated studies to specify the regional perturbation due to smooth or abrupt variations in volcanic emissions, as large fluctuations are a key feature of dominant volcanoes like the Ambrym volcano (Bani et al., 2009, 2012).

Acknowledgments

The authors appreciate the University of Miami Aerosol Group for providing surface aerosols measurement data over the South Pacific and thank J.M. Prospero for constructive comments on their data. We also thank S.R. Freitas, P.I. of the preprocessor PREP-CHEM-SRC and for providing various datasets compatible with the preprocessor used in this study. We also thank the Koninklijk Nederlands Meteorologisch Instituut (KNMI) OMI team and the NASA Goddard Earth Sciences Data and Information Services Center for producing L2 OMI SO_2 and MODIS Aerosol/Cloud products and the NASA CALIPSO team for the online free access to CALIPSO archives. We acknowledge the NCAR Earth System Laboratory team for the production of MOZART data used in the chemical forcing. Finally, we appreciate financial support from IRD and Agence National de la

Recherche (ANR MC VULN 0002) for the PC-Cluster of Noumea that was used for our model simulations. R. Frouin is supported by the NASA under various grants.

Appendix A. CALIOP aerosol type classification and uncertainties

Aerosol layers are first discriminated from clouds using the Cloud Aerosol Discrimination (CAD) algorithm (Liu et al., 2009) and then the aerosol type for each feature layer is retrieved using the particle extinction-to-backscatter ratio (S ratio) and the depolarization capability of the lidar at 532 nm (Winker et al., 2009). The aerosol type classification and the estimated aerosol extinction profile for an aerosol feature layer previously identified by the CAD is based on the selection of a 'best-match' S ratio from a lookup table of pre-computed S ratio. This look-up table was generated by an extensive clustering analysis of global AERONET measurements (Omar et al., 2005). CALIOP observables (depolarization and backscatter) are used to retrieve the best candidate for S ratio.

The level of confidence in the aerosol retrieval is reflected by a CAD score, which range from −100 to 0. Using recommendations from Yu et al. (2010), we use a CAD score between −100 and −20. Following this first data screening, applied to night time lidar profiles only (with higher signal-to-noise ratio due to the absence of solar background signal), suspicious measurements with cloud optical depth > 0.1 and for which the initial S ratio differs from the final one are removed, according to Yu et al. (2010) and Kittaka et al. (2011).

As synthesized in Oo and Holz (2011, their discussion) significant sources of uncertainty exist in the derived CALIOP AOD and layer aerosol properties, as a consequence of inaccuracies in the S ratio-retrieving scheme. For example, Oo and Holz (2011) showed that in some cases, the CALIOP version 3 algorithm misuses a S ratio of 20 steradian (clean marine, presence of coarse sea salt) rather than 40 steradian (presence of fine dust), inducing a misclassification of fine aerosols over the ocean and underestimation of AOD by a factor of about 2. Our intercomparison of AOD observations given by CALIOP and MODIS tends to confirm the reported errors, but for sea salt mixed with fresh volcanic sulfate particles (Section 6.3). The origin of the bias warrants further investigations. However, for particular eruptive events, aerosol optical features and similar AOD quantities in the Ambae (Vanuatu) eruptive plume of 11 April 2010 are well observed in both CALIOP and MODIS (not shown here) and provide useful examples of the CALIOP's ability to capture shallow ash plume.

Appendix B. FlexAOD: description and adjustments

1. Description of FlexAOD

Given the simulated distributions and composition of aerosols, AOD (or τ, dimensionless) can be calculated from the complex refractive

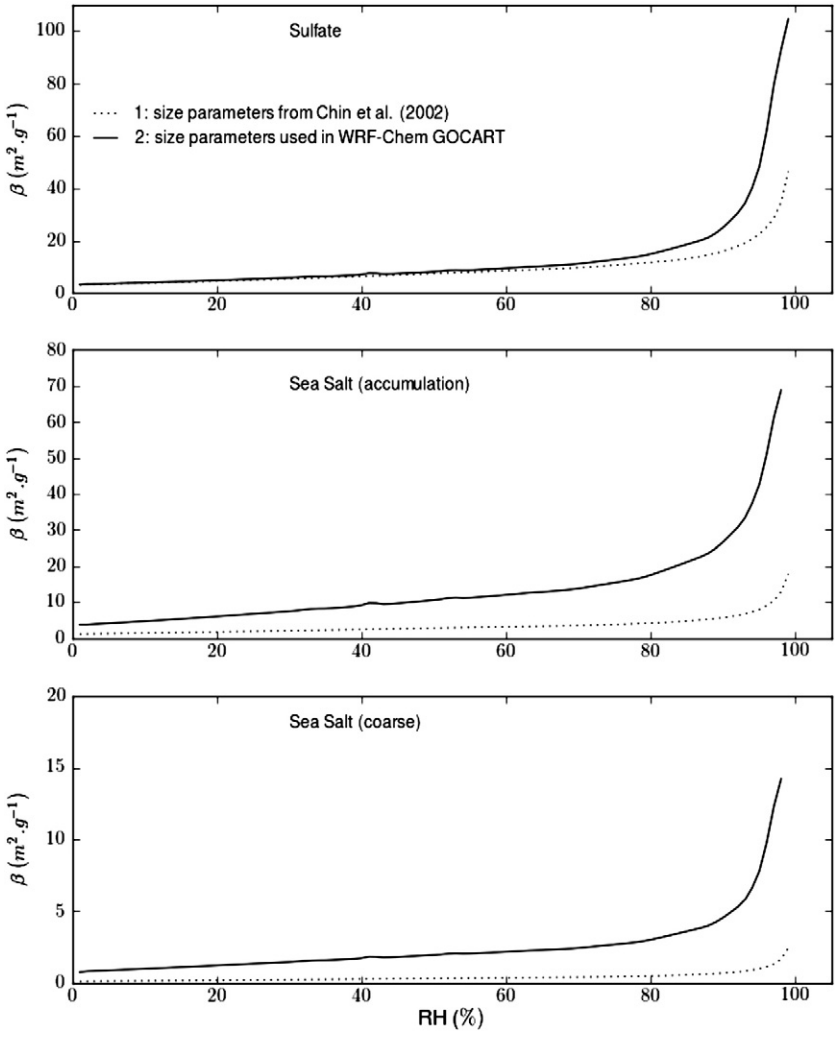

Fig. B1. Mass extinction efficiency ß at wavelength 550 nm as a function of RH for water-soluble aerosols (sulfate, sea-salt accumulation and coarse mode). ß-RH relations using the original particle-size distributions (PSDs) of GSFC/GOCART P4G0 are displayed with dotted curves. Solid curves represent ß-RH relations with new size parameters applied in our setup of GOCART/WRF-Chem (see Table B1 for the size parameters).

indices, particle-size distributions (hereafter PSD) and hygroscopic properties of aerosols. Originally developed as post-processing tool for the GEOS-Chem model, FlexAOD (http://pumpkin.aquila.infn.it/flexaod/) was adapted here to compute τ offline using WRF-Chem outputs. Before introducing FlexAOD, let us detail the relationship between simulated τ and aerosol optical and microphysical properties. These relations are helpful to highlight some current issues in τ calculation due to assumed dry PSD or to small errors in simulated moisture fields used to derive the hygroscopic growth. τ at a given wavelength is the vertical column integration of the specific aerosol extinction coefficient (σ_{aer}, unit m^{-1}); that is:

$$\tau = \int_Z \sigma_{aer} dz. \tag{B.1}$$

For a single-component aerosol population comprised of spherical wet particles following a size-resolved number concentration, its specific extinction coefficient σ_{aer} (Eq. (B.1)) is related to the dimensionless efficiency factor for extinction by the relation (Li et al., 2008):

$$\sigma_{aer} = \int_{r_w} \pi r_w^2 \frac{dN(r_w)}{dr_w} q_{ext(\lambda,r_w)} dr_w \tag{B.2}$$

where q_{ext} is the efficiency factor, function of wavelength λ, wet radius r_w and is also dependent on wet aerosol composition through its complex refractive indices. In FlexAOD, q_{ext} is calculated from Mie's scattering model developed by Mishchenko et al. (1999), with particles assumed spherical. Optical and microphysical properties of water soluble aerosols, like sea salt and sulfate, are very sensitive to the hygroscopic growth with *RH*, resulting in a mass and size change due to the uptake of water (hereafter the swelling effect). In the calculation of q_{ext} with the Mie code, the swelling effect for the size change is considered through r_w, while the change of optical properties due to the uptake of water is incorporated using the combination of the refractive indices of water and dry aerosols. In FlexAOD, wet aerosol optical properties are based on an assumed dry aerosol PSD for each aerosol component and by including the swelling effect using a set of hygroscopic growth factors at representative *RH* (Chin et al., 2002).

One key parameter for relating the radiative properties to a given dry PSD are the effective radius r_{eff}, which is the cross-section weighted mean radius (Chin et al., 2002) defined as:

$$r_{eff} = \frac{\int_0^\infty \pi r^3 n(r) dr}{\int_0^\infty \pi r^2 n(r) dr} \tag{B.3}$$

where $n(r)$ is the PSD expressing the size-resolved number concentration as a function of dry radius r. For sea salt or sulfate aerosols, their PSDs can be well approximated by a lognormal distribution (see Li et al., 2008):

$$n(r) = \frac{dN(r)}{dr} = \frac{N_0}{\ln\sigma_g \sqrt{2\pi} r} e^{\left[\frac{-(\ln r - \ln r_g)^2}{2(\ln\sigma_g)^2}\right]}, \tag{B.4}$$

where N_0 is the total number density, r_g and σ_g are the geometric mean radius and standard deviation respectively. Two parameters can be retrieved from the properties of lognormal distribution (Li et al., 2008). They are the effective radius r_{eff} defined above (Eq. (B.3)), and the effective variance v_{eff}:

$$r_{eff} = \sigma_g e^{2.5(\ln\sigma_g)^2}, \tag{B.5}$$

$$v_{eff} = e^{\left((\ln\sigma_g)^2\right)} - 1. \tag{B.6}$$

Finally, as shown by Chin et al. (2002), one convenient way to relate τ with the simulated dry aerosol mass loading M_d, r_{eff} and the swelling effect is the relation:

$$\tau = \sum_{i=(SU..BC)} \int_Z \sigma_{aer,i} dz = \sum_{i=(SU..BC)} \int_Z \beta_i M_{d,i} dz \tag{B.7}$$

where i is the aerosol type used in the GOCART model OC, BC, SU, SS and DU and β ($m^2\ g^{-1}$) the mass extinction efficiency with expression:

$$\beta_i = \frac{3}{4} \frac{q_{ext,i} M_i}{r_{eff,i} \rho_i M_{d,i}}, \tag{B.8}$$

where ρ_i is the component density, M_i the column aerosol mass in the grid-cell and $q_{ext,i}$ the aforementioned efficiency factor for extinction, with the swelling effect incorporated in these two quantities. It is worth noting that in global aerosol models based on GOCART (for example GSFC/GOCART), lookup tables of precomputed values of βs are used to derive the wavelength aerosol optical extinction for each aerosol type. Such precomputed and hardcoded values are strongly dependent on assumed aerosol properties, including their size parameters. Indeed, as shown above, since σ_{aer} is proportional to the square of wet radius (Eq. (B.2)), simulated AOD is very sensitive to the assumed aerosol dry PSD, with parameters given in Eqs. (B.4), (B.5) and (B.6). Then, as shown in Eq. (B.7), since all the humidification effects detailed above are embodied in the value of β, this quantity will be very useful later to investigate how assumptions on PSD or model *RH* errors can influence the simulated AOD.

2. Adjustments and sensitivity

In FlexAOD, AOD calculation follows the methodology developed by Martin et al. (2003), by assuming external mixing of different aerosol types. Hygroscopic properties and refractive indices of individual aerosol types are taken from the Optical Properties of Aerosol and Clouds (OPAC, Hess et al., 1998) for eight relative humidity bins (RH = 0, 50, 70, 80, 90, 95, 98 and 99%), but refractive indices for dust are taken from Sinyuk et al. (2003). Aerosol properties at the eight *RH* bins are used to calculate a lookup table of aerosol optical properties, including q_{ext} and r_{eff} modified by the swelling effect, using the Mie code. Vertical profiles of simulated *RH* are then used to interpolate the specific optical properties at each model level. GOCART is a bulk (mass only) aerosol model that only gives M_d for each dry size bin, without any additional information on their specific PSD. Therefore, each aerosol mass size bin is assumed to have a PSD with geometric parameters defined in Table B *1*, gray shaded row. These geometric parameters for SU, OC and BC have been recently adjusted following results from Drury et al. (2010).

AOD changes due to modified SSA and SSC dry PSDs

As shown by Li et al. (2008) and recently by Jaeglé et al. (2011), AERONET observations in remote islands and field studies show that the dry sea salt effective radius for SSA (0.73 μm) and SSC (6.13 μm) are unreasonably large in OPAC. Jaeglé et al. (2011) suggest new values for these parameters, with 0.13 μm and 0.95 μm for SSA and SSC respectively, at present used in GEOS-Chem. Inspired by these remarks, dry effective radius for SSA and SSC are also reduced in our study to 0.25 μm and 1.1 μm respectively. In the GOCART sectional scheme for sea salt, SS are represented with four mass size bins with dry size bins: 0.1–0.5, 0.5–1.5, 1.5–5, and 5–10 μm, and dry effective radii 0.3, 1.0, 3.2 and 7.5 μm respectively. Our changes on SSA and SSC imply that the first and second mass size bins in GOCART now have a similar dry PSD to that of SSA and SSC respectively. According to Jaeglé et al. (2011), short-lived giant SS with dry radius above 4 μm are optically less important and could be neglected in the AOD computation. This suggestion implies considering GOCART SS concentrations for 1.5–5 and 5–10 size

bins as giant and ultra-giant sea salt respectively. Consequently, they are excluded from the AOD computation.

As stressed above, modified dry PSD values of water-soluble SU, SSA and SSC are expected to produce large changes in mass extinction efficiencies ß. For example, in Table B *1*, the effective radii r_{eff} are reduced by factors of 2, 3 and 5.5 for SU, SSA and SSC respectively in comparison with GSFC/GOCART. The response on ß at $\lambda = 550$ nm is shown in Fig. B1 for SU, SSA and SSC and shows a strong increase for these components. Larger size parameters result in lower AOD values and the sea salt AOD is biased low in GSFC/GOCART, as discussed in Section 8.5. But Fig. B1 also shows the strong *RH* dependence of ß, as discussed by Chin et al. (2002). Contrasting with dryer regions, the swelling of water-soluble aerosols in the saturated tropical belt is promoted and ß becomes very sensitive to even minor errors in *RH*. Those errors may be artificially introduced by using wrong meteorological moisture fields, which is common in GCMs as investigated by John and Soden (2007).

Appendix C. New and revised aerosol processes in WRF-Chem/GOCART

Here, distributions of aerosols and gases are simulated using the WRF-Chem V3.3.1 public release coupled online with GOCART. Due to ours choices of physics and recent advances in aerosol modeling for source and sink mechanisms, we revised some of the proposed schemes and implemented new modules in the modeling system. Details of the revised modeling system are given in Fig. C1, with revised parts highlighted by cross-hatching. The most relevant changes are detailed in points (1), (2), and (3) below. Points (4) and (5) give further details about the turbulent vertical mixing of tracers and known limitations.

(1) Natural emission as a function of wind and SST
The GOCART emission module computes the generation of DU and SS as a function of wind speed and gaseous DMS exchange at the ocean surface as a function of both wind and SST. Details for DU emission using the source function from Ginoux et al. (2001) are given in Zhao et al. (2010) and their implementation in WRF-CHEM V3.3.1 are kept unchanged for our study. The biogenic emission of DMS is parameterized using the semi-empirical scheme of Liss and Merlivat (1986) with DMS data from Kettle et al. (1999). To test the sensitivity of DMS to both the air–sea gas exchange parameterization and the database, we added in the GOCART DMS emission module an alternate scheme from Nightingale et al. (2000). In addition, updated climatological DMS fields from Lana et al. (2011) are preprocessed using PREP-CHEM-SRC (Freitas et al., 2011). As for sea salt, which is a key aerosol in the marine boundary layer, only the Gong (2003) source function is proposed in the GOCART emission module. In there, the SS particle number density function (unit: particles $m^{-2}\ s^{-1}\ \mu m^{-1}$) is expressed as:

$$\frac{dF}{dr_{80}} = 1.373 u_{10m}^{3.41} r_{80}^{-A} (1 + 0.057 r_{80}^{3.45}) \times 10^{1.607 e^{-B^2}} \quad (C.1)$$

with $A = 4.7(1 + \Theta r_{80})^{-0.017 r_{80}{}^{-1.44}}$ and $B = [0.433 - \log_{10}(r_{80})]/0.433$. r_{80} is the particle radius at $RH = 80\%$ and $U_{10\,m}$ the 10-m wind speed. The parameter $\Theta\ (=30)$ is an adjustable parameter, which controls the shape of the particle-size distribution of submicron SS aerosols (Gong, 2003). To test the sensitivity of SS mass concentrations and SS AOD to the SS source function, we implemented another source function from Jaeglé et al.'s (2011). Like in Gong (2003), it is based on the original whitecap coverage function defined by Monahan et al. (1986) that varies with wind speed, but the SS generation process here is limited by SST, as follows:

$$\frac{dF}{dr_{80}} = \left(0.3 + 0.1 \times SST - 0.0076 \times SST^2 + 0.00021 \times SST^3\right) .1.373 u_{10m}^{3.41} r_{80}^{-A} \times (1 + 0.057 r_{80}^{3.45}) \times 10^{1.607 e^{-B^2}} \quad (C.2)$$

with A and B are parameters defined above and SST is in °C.

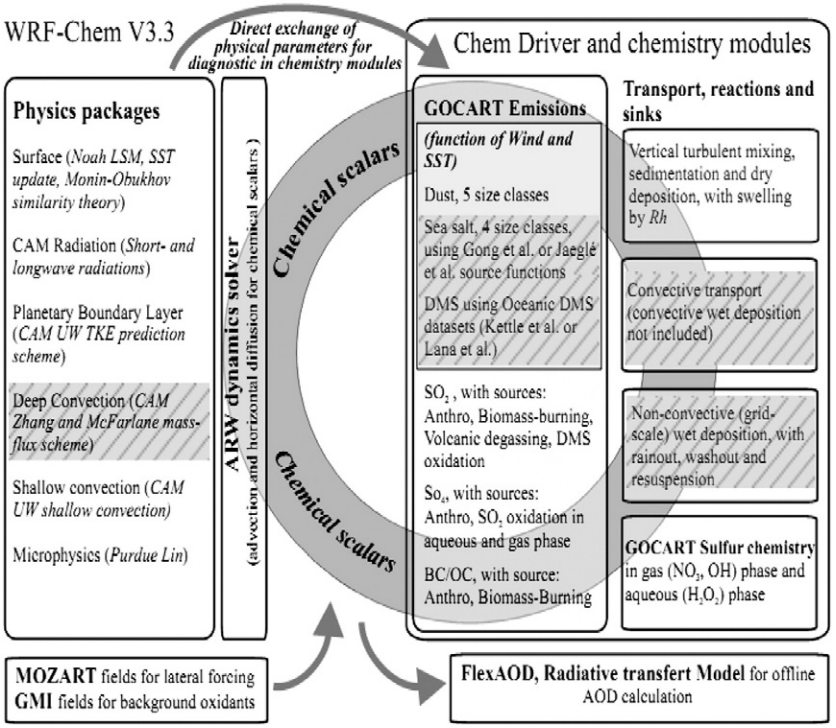

Fig. C1. Diagram of the meteorology-chemistry modeling system composed of WRF-Chem V3.3, coupled online to GOCART for aerosol fate and transport, and offline to FlexAOD for aerosol optical properties. The ring symbolizes the exchange of arrays with chemical species (including aerosols and gases). New or revised physical and chemistry modules involved in aerosol processes are identified with cross hashing (see text for details).

(2) Grid-scale wet deposition and tracer re-suspension
In WRF-Chem/GOCART, only a simple first-order loss process for grid-scale wet deposition is proposed. This scheme only includes in-cloud scavenging (or rainout by nucleation), but do not include below-cloud scavenging (or washout by impaction) of tracers. In addition, tracer re-suspension of soluble species following the evaporation of rain droplets was not implemented for grid-scale wet deposition. Therefore, we added these new capabilities in the model using the algorithm described in Jacob et al. (2000) and Liu et al. (2001), with rainout, washout and grid-scale re-suspension parameterized according to Giorgi and Chameides (1986) and Balkanski et al. (1993).
The description of the new wet deposition scheme, tied to the Purdue Lin bulk microphysics (Table 3), is briefly summarized here. Within cloud, cloud- and ice-crystal-borne aerosols and gases dissolved in cloud water are collected by hydrometeors using the first order loss rate of cloud to precipitation given by the Purdue Lin scheme. Currently, only grid cells including hydrometeors in liquid phase are activated in wet deposition, which is an acceptable assumption in the tropics and subtropics. In the absence of a more realistic but computationally-expensive cloud-aerosol microphysics scheme, the scavenging efficiency of soluble gases (including SO_2) and aerosols is fixed to 100% (solubility = 1) and the fraction f_{scav} of tracer experiencing rainout is inferred from the Purdue Lin scheme parameters, according to Jacob et al. (2000):

$$fscav = \frac{Q}{k(L+W)} \tag{C.3}$$

where Q ($cm^3_{H2O}\ cm^{-3}_{air}\ s^{-1}$) is the rate of new precipitation formation in the gridbox, L and W are the cloud condensed and ice water content, respectively ($cm^3_{ICEorH2O}\ cm^{-3}_{air}$), and k (s^{-1}) is the conversion of cloud water to precipitation (or autoconversion rate, including accretion of cloud water by falling liquid and frozen hydrometeors). Below cloud, aerosols are also removed by washout, i.e., wet deposition by falling droplets. But part of it can be released back to the atmosphere as rain droplets evaporate, SO_2 being then totally converted to sulfate aerosol.

(3) Convective tracer transport
WRFV3.3.1 includes the deep convection parameterization inspired from Zhang and McFarlane (Zhang and McFarlane, 1995) scheme, with algorithm's details given in the CAM3 documentation (Collins et al., 2004 and http://www.cesm.ucar.edu/models/atm-cam/docs/description). In WRF-Chem, the convective transport of chemical tracers was not tied with the ZM mass-flux scheme. In this study, we consistently used for chemical tracers the vertical mass fluxes and entrainment/detrainment rates given by ZM deep convection. This implementation based on the original convective tracer transport treatment for CAM3 (See CAM3 documentation, 4.1.5 Deep Convective Tracer Transport) is part of a new WRF-Chem module now available to the WRF-Chem community.

(4) Subgrid-scale turbulent vertical mixing
The subgrid scale vertical mixing of aerosols is made outside the WRF PBL module but it remains tied to the choice of PBL scheme as it uses its eddy diffusion coefficients for heat *Kh*. This limits the choice of PBL scheme available in WRF-Chem, as pointed out by Pleim (2011). In WRFV3.3.1, only the YSU scheme (Hong et al., 2006) and Mellor-Yamada based schemes, both the MYJ (Janjić, 2002) and MYNN (Nakanashi and Niino, 2004) are available. But, for our choice of UW-CAM5 PBL, *Kh* was not readily available. Nevertheless, it can be retrieved from the scheme's turbulence quantities, and in our study this quantity is used to derive the vertical diffusion of aerosols.

(5) Known limitations
Absence of aerosol transport related to shallow convection
It is worth noting that the aerosol vertical mixing and transport needs to account for shallow convection in UW-CAM5, which is currently not provided within WRF-Chem. To assess the relevance of this missing ingredient, mean updraft mass fluxes associated with deep and shallow convection are compared in Fig. C2, for the convective box and the southeastern tip of the SPCZ defined in Fig. 13d. Looking at mass transport and altitude

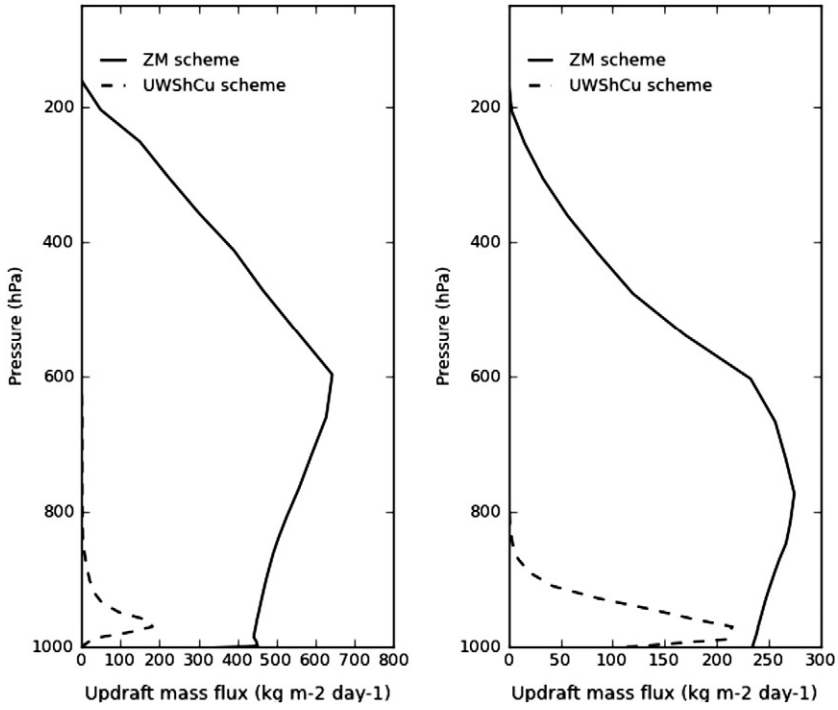

Fig. C2. Vertical profiles of time-averaged (Oct-2006 to Oct-2008) updraft mass fluxes given by the deep convection scheme (Zhang and McFarlane, 1995) and shallow convection scheme (Park and Bretherton, 2009) used in this study. Left and right panels present the deep convection and southeastern SPCZ regions, respectively, defined in Fig. 13 d.

reached, the convective transport by the Zhang and MacFarlane deep convection scheme is clearly more efficient than shallow convection.

Convective wet deposition not included

Furthermore, the convective transport described in (3) implies that aerosols are lofted upward without wet removal. To balance the convective tracer venting, empirical scavenging treatments tied with the mass flux and cloud scheme for deep convection are commonly applied in climate models with coarse resolution. Herein, the solubility factor is used like a tunable parameter to adjust the tracer lifetime, as detailed in Fan and Toon (2011). Moreover, using a global climate model with different treatments for the convective tracer transport, Croft et al. (2012) show that the introduction of sophisticated explicit aerosol-cloud microphysical processes affects strongly the aerosol burden, with a factor of two compared to the standard model without sophisticated parameterization for convective wet scavenging. This complements the Textor et al. (2006) remarks about the large sensitivity of convective wet scavenging to the convection scheme. In our model setup, the convective wet scavenging of tracers is not included. The sensitivity to this will be explored in future simulations.

References

Albrecht, B.A., 1989. Aerosols, cloud microphysics, and fractional cloudiness. Science 245 (4923), 1227–1230.

Allibone, R., Cronin, S.J., Charley, D.T., Neall, V.E., Stewart, R.B., Oppenheimer, C., 2010. 2010: Dental Fluorosis Linked to Degassing of Ambrym Volcano, Vanuatu: A Novel Exposure Pathway. Environ Geochem Health.

Andres, R., Kasgnoc, A., 1998. A time-averaged inventory of sub-aerial volcanic sulfur emissions. J. Geophys. Res. 103 (19), 25251–25261.

Athanasopoulou, E., Tombrou, M., Pandis, S.N., Russell, A.G., 2008. The role of sea salt emissions and heterogeneous chemistry in the air quality of polluted coastal areas. Atmos. Chem. Phys. 8, 5755–5769.

Ayers, G.P., Gillett, R.W., 2000. DMS and its oxidation products in the remote marine atmosphere: implications for climate and atmospheric chemistry. J. Sea Res. 43, 275–286.

Balkanski, Y., Jacob, D., Gardner, G., Graustein, W., Turekian, K., 1993. Transport and residence times of tropospheric aerosols inferred from a global three-dimensional simulation of 210Pb. J. Geophys. Res. 98, 20573.

Bani, P., Oppenheimer, C., Tsanev, V.I., Carn, S.A., Cronin, S.J., Crimp, R., Calkins, J.A., Charley, D., Lardy, M., Roberts, T.R., 2009. Surge in sulfur and halogen degassing from Ambrym volcano, Vanuatu. Bull. Volcanol. 71 (10), 1159–1168.

Bani, P., Oppenheimer, C., Allard, P., Shinohara, H., Tsanev, V., Carn, S., Lardy, M., Garaebeti, E., 2012. First arc-scale volcanic SO_2 budget for the Vanuatu archipelago. J. Volcanol. Geotherm. Res. 211–212, 36–46.

Bobrowski, N., Hönninger, G., Galle, B., Platt, U., 2003. Detection of bromine monoxide in a volcanic plume. Nature 423, 273–276.

Boichu, M., Oppenheimer, C., Roberts, T.J., Tsanev, V., Kyle, P.R., 2011. On bromine, nitrogen oxides and ozone depletion in the tropospheric plume of Erebus volcano (Antarctica). Atmos. Environ. 45, 3856–3866.

Boucher, O., Moulin, C., Belviso, S., Aumont, O., Bopp, L., Cosme, E., von Kuhlmann, R., Lawrence, M.G., Pham, M., Reddy, M.S., Sciare, J., Venkataraman, C., 2003. DMS atmospheric concentrations and sulphate aerosol indirect radiative forcing: a sensitivity study to the DMS source representation and oxidation. Atmos. Chem. Phys. 3, 49–65. http://dx.doi.org/10.5194/acp-3-49-2003.

Bretherton, C.S., Park, S., 2009. A new moist turbulence parameterization in the Community Atmosphere Model. J. Clim. 22, 3422–3448.

Cai, W., et al., 2012. More extreme swings of the South Pacific Convergence Zone due to greenhouse warming. Nature 488, 365–370. http://dx.doi.org/10.1038/nature11358.

Carn, S.A., Krotkov, N.A., Yang, K., Hoff, R.M., Prata, A.J., Krueger, A.J., Loughlin, S.C., Levelt, P.F., 2007. Extended observations of volcanic SO_2 and sulfate aerosol in the stratosphere. Atmos. Chem. Phys. Discuss. 7, 2857–2871.

Carn, S.A., Krueger, A.J., Krotkov, N.A., Yang, Kai, Evans, Keith, 2009. Tracking volcanic sulfur dioxide clouds for aviation hazard mitigation. Nat. Hazards 51, 325–343. http://dx.doi.org/10.1007/s11069-008-9228-4.

Chapman, E.G., Gustafson Jr., W.I., Barnard, J.C., Ghan, S.J., Pekour, M.S., Fast, J.D., 2009. Coupling aerosol-cloud-radiative processes in the WRF-Chem model: investigating the radiative impact of large point sources. Atmos. Chem. Phys. 9, 945–964.

Chen, F., Dudhia, J., 2001. Coupling an advanced land-surface/ hydrology model with the Penn State/ NCAR MM5 modeling system. Part I: Model description and implementation. Mon. Weather Rev. 129, 569–585.

Chin, M., Rood, R.B., Lin, S.-J., Muller, J.F., Thomspon, A.M., 2000a. Atmospheric sulfur cycle in the global model GOCART: model description and global properties. J. Geophys. Res. 105, 24,671–24,687.

Chin, M., Savoie, D., Thornton, D., Bandy, A., Huebert, B., Bandy, A.R., Thornton, D.C., Bates, T.S., Quinn, P.K., Saltsman, E.S., De Bruyn, W.J., 2000b. Atmospheric sulfur cycle in the global model GOCART: comparison with observations. J. Geophys. Res. 105, 24,698–24,712.

Chin, M., Ginoux, P., Kinne, S., Torres, O., Holben, B.N., Duncan, B.N., Martin, R.V., Logan, J.A., Higurashi, A., Nakajima, T., 2002. Tropospheric aerosol optical thickness from the GOCART model and comparisons with satellite and sunphotometer measurements. J. Atmos. Sci. 59, 461,483.

Colarco, P.R., da Silva, A., Chin, M., Diehl, T., 2010. Online simulations of global aerosol distributions in the NASA GEOS-4 model and comparisons to satellite and ground-based aerosol optical depth. J. Geophys. Res. 115 D14207.

Collins, W., Co-authors, 2004. Description of the NCAR Community Atmosphere Model (CAM 3.0). NCAR Technical Note NCAR/TN-464+STR. NCAR, Boulder, CO.

Croft, B., Pierce, J.R., Martin, R.V., Hoose, C., Lohmann, U., 2012. Strong sensitivity of aerosol concentrations to convective wet scavenging parameterizations in a global model. Atmos. Chem. Phys. Discuss. 12, 1687–1732. http://dx.doi.org/10.5194/acpd-12-1687-2012.

Cronin, S.J., Sharp, D.S., 2002. Environmental impacts on health from continuous volcanic activity at Yasur (Tanna) and Ambrym, Vanuatu. Int. J. Environ. Health Res. 12, 109–123.

DeMore, W.B., Sander, S.P., Golden, D.M., Hampson, R.F., Kurylo, M.J., Howard, C.J., Ravishankara, A.R., Kolb, C.E., Molina, M.J., 1997. Chemical kinetics and photochemical data for use in stratospheric modeling. JPL Publ. 97–4, 1–278.

Dentener, F., Kinne, S., Bond, T., et al., 2006. Emissions of primary aerosol and precursor gases in the years, 2000 and 1750, prescribed data-sets for AeroCom. Atmos. Chem. Phys. Discuss. 6, 4321–4344.

Douglass, A.R., Stolarski, R.S., Strahan, S.E., Connell, P.S., 2004. Radicals and reservoirs in the GMI chemistry and transport model: comparison to measurements. J. Geophys. Res.-Atmos. 109, D16302. http://dx.doi.org/10.1029/2004JD004632.

Drury, E., Jacob, D.J., Spurr, R.J.D., Wang, J., Shinozuka, Y., Anderson, B.E., Clarke, A.D., Dibb, J., McNaughton, C., Weber, R., 2010. Synthesis of satellite (MODIS), aircraft (ICARTT), and surface (IMPROVE, EPA-AQS, AERONET) aerosol observations over eastern North America to improve MODIS aerosol retrievals and constrain surface aerosol concentrations and sources. J. Geophys. Res. 115. http://dx.doi.org/10.1029/2009JD012629 D14204.

Duncan, B.N., et al., 2003a. Interannual and seasonal variability of biomass burning emissions constrained by satellite observations. J. Geophys. Res. 108 (D2), 4040.

Duncan, B.N., Bey, I., Chin, M., Mickley, L.J., Fairlie, T.D., Martin, R.V., Matsueda, H., 2003b. Indonesian wildfires of 1997: impact on tropospheric chemistry. J. Geophys. Res. 108. http://dx.doi.org/10.1029/2002JD003195.

Ebmeier, S.K., Sayer, A.M., Grainger, R.G., Mather, T.A., Carboni, E., 2014. Systematic satellite observations of the impact of aerosols from passive volcanic degassing on local cloud properties. Atmos. Chem. Phys. 14 (19), 10601–10618.

Eldin, G., Ganachaud, A., Cravatte, S., Jeandel, C., 2013. Pandora Cruise Provides an Unprecedented Description of the Solomon Sea. CLIVAR Newsletter Exchanges 61 (no. 18), 24–25.

Emmons, L.K., coauthors, 2010. Description and evaluation of the Model for Ozone and Related chemical Tracers, version 4 (MOZART-4). Geosci. Model Dev. 3, 43–67.

Faloona, Ian, 2009. Sulfur processing in the marine atmospheric boundary layer: a review and critical assessment of modeling uncertainties. Atmos. Environ. 43 (18), 2841–2854.

Faloona, I.C., Conley, S.A., Blomquist, B., Clarke, A., Howell, S., Kapustin, V., Bandy, A., 2010. Sulfur dioxide in the tropical marine boundary layer: dry deposition and heterogeneous oxidation observed during the Pacific Atmospheric Sulfur Experiment. J. Atmos. Chem. 63 (1), 13–32.

Fan, T., Toon, O.B., 2011. Modeling sea-salt aerosol in a coupled climate and sectional microphysical model: mass, optical depth and number concentration. Atmos. Chem. Phys. 11, 4587–4610.

Fast, J.D., Gustafson Jr., W.I., Easter, R.C., Zaveri, R.A., Barnard, J.C., Chapman, E.G., Grell, G.A., 2006. Evolution of ozone, particulates, and aerosol direct forcing in an urban area using a new fully-coupled meteorology, chemistry, and aerosol mode. J. Geophys. Res.-Atmos. 111.

Fenn, M.A., et al., 1999. Ozone and aerosol distributions and air mass characteristics over the South Pacific during the burning season. J. Geophys. Res. 104 (D13), 16197–16212.

Fetzer, E.J., Lambrigtsen, B.H., Eldering, A., Aumann, H.H., Chahine, M.T., 2006. Biases in total precipitable water vapor climatologies from Atmospheric Infrared Sounder and Advanced Microwave Scanning Radiometer. J. Geophys. Res. 111, D09S16. http://dx.doi.org/10.1029/2005JD006598.

Forster, P., Ramaswamy, V., Artaxo, P., Berntsen, T., Betts, R., Fahey, D.W., Haywood, J., Lean, J., Lowe, D.C., Myhre, G., Nganga, J., Prinn, R., Raga, G., Schulz, M., Van Dorland, R., 2007. Changes in Atmospheric Constituents and in Radiative Forcing. In: Solomon, S., Qin, D., Manning, M., Chen, Z., Marquis, M., Averyt, K.B., Tignor, M., Miller, H.L. (Eds.), Climate Change 2007: The Physical Science BasisContribution of Working Group I to the Fourth Assessment Report of the Intergovernmental Panel on Climate Change. Cambridge University Press, Cambridge, United Kingdom and New York, NY, USA.

Freitas, S.R., Longo, K.M., Alonso, M.F., Pirre, M., Marecal, V., Grell, G., Stockler, R., Mello, R.F., Sanchez Gacita, M., 2011. PREP-CHEM-SRC 1.0: a preprocessor of trace gas and aerosol emission fields for regional and global atmospheric chemistry models. Geosci. Model Dev. 4, 419–433.

Fuelberg, H.E., Newell, R.E., Longmore, S.P., Zhu, Y., Westberg, D.J., Browell, E.V., Blake, D.R., Gregory, G.L., Sachse, G.W., 1999. A meteorological overview of the Pacific Exploratory Mission (PEM) Tropics period. J. Geophys. Res. 104 (D5), 5585–5622. http://dx.doi.org/10.1029/98JD01215.

Gassó, S., 2008. Satellite observations of the impact of weak volcanic activity on marine clouds. J. Geophys. Res.-Atmos. 113, D14S19. http://dx.doi.org/10.1029/2007JD009106.

George, R.C., Wood, R., 2010. Subseasonal variability of low cloud radiative properties over the southeast Pacific Ocean. Atmos. Chem. Phys. 10, 4047–4063.

Ginoux, P., Chin, M., Tegen, I., Prospero, J.M., Holben, B., Dubovik, O., Lin, S., 2001. Sources and distributions of dust aerosols simulated with the GOCART model. J. Geophys. Res. 106, 20225–20273.
Giorgi, F., Chameides, W.L., 1986. Rainout lifetimes of highly soluble aerosols as inferred from simulations with a general circulation model. J. Geophys. Res. 91, 14,367–14,376.
Gong, S.L., 2003. A parameterization of sea-salt aerosol source function for sub- and super-micron particles. Glob. Biogeochem. Cycles 17 (4), 1097. http://dx.doi.org/10.1029/2003GB002079.
Graf, H.-F., Feichter, J., Langmann, B., 1997. Volcanic sulfur emission: estimates of source strength and its contribution to the global sulfate distribution. J. Geophys. Res. 102, 10,727–10,738.
Gray, B., Wang, Y., Gu, D., Bandy, A., Mauldin, L., Clarke, A., Alexander, B., Davis, D.D., 2010. Sources, transport and sinks of SO_2 over the equatorial Pacific during the Pacific Atmospheric Sulfur Experiment. J. Atmos. Chem. http://dx.doi.org/10.1007/s10874-010-9177-7 (PASE special issue).
Gerlach, T.M., 2004. Volcanic sources of tropospheric ozone-depleting trace gases. Geochem. Geophys. Geosyst. 5, Q09007. http://dx.doi.org/10.1029/2004GC000747.
Grell, G.A., Peckham, S.E., Schmitz, R., McKeen, S.A., Frost, G., Skamarock, W.C., Eder, B., 2005. Fully coupled "online" chemistry within the WRF model. Atmos. Environ. 39, 6957e6975.
Haywood, J.M., Boucher, O., 2000. Estimates of the direct and indirect radiative forcing due to tropospheric aerosols: *a review*. Rev. Geophys. 38, 513–543.
Hess, M., Koepke, P., Schult, I., 1998. Optical properties of aerosols and clouds: the software package OPAC. Bull. Am. Meteorol. Soc. 79, 831–844.
Hong, S.-Y., Noh, Y., Dudhia, J., 2006. A new vertical diffusion package with an explicit treatment of entrainment processes. Mon. Weather Rev. 134, 2318–2341.
Hoppel, W.A., Caffrey, P.F., Frick, G.M., 2005. Particle deposition on water: surface source versus upwind source. J. Geophys. Res. 110, D10206. http://dx.doi.org/10.1029/2004jd005148,2005.
Hoyle, C.R., coauthors, 2011. Representation of tropical deep convection in atmospheric models—part 2: tracer transport. Atmos. Chem. Phys. 11, 8103–8131. http://dx.doi.org/10.5194/acp-11-8103-2011.
Jacob, D.J., 1986. Chemistry of OH in remote clouds and its role in the production of formic acid and peroxymonosulfate. J. Geophys. Res. 91 (D9), 9807–9826.
Jacob, D.J., Liu, H., Mari, C., Yantosca, R.M., 2000. Harvard Wet Deposition Scheme for GMI. Harvard University Atmospheric Chemistry Modeling Group (revised March 2000).
Jacobson, M.Z., 2005. Fundamentals of Atmospheric Modeling. Second ed. Cambridge University Press, New York.
Jaeglé, L., Quinn, P.K., Bates, T., Alexander, B., Lin, J.-T., 2011. Global distribution of sea-salt aerosols: new constraints from in situ and remote sensing observations. Atmos. Chem. Phys. 11, 3137–3157. http://dx.doi.org/10.5194/acp-11-3137-2011.
Janjić, Z.I., 2002. Nonsingular Implementation of the Mellor-Yamada Level 2.5 Scheme in the NCEP Meso model. NCEP Office Note 437 (61 pp.).
Jiménez, Pedro A., Dudhia, Jimy, Fidel González-Rouco, J., Navarro, Jorge, Montávez, Juan P., Garcia-Bustamante, Elena, 2012. A revised scheme for the WRF surface layer formulation. Mon. Weather Rev. 140, 898–918.
John, V.O., Soden, B.J., 2007. Temperature and humidity biases in global climate models and their impacts on climate feedbacks. Geophys. Res. Lett. 34, L18605.
Jones, T.A., Christopher, S.A., 2011. A reanalysis of MODIS fine mode fraction over ocean using OMI and daily GOCART simulations. Atmos. Chem. Phys. 11 (12), 5805–5817. http://dx.doi.org/10.5194/acp-11-5805-2011.
Jourdain, N., Marchesiello, P., Menkes, C., Lefevre, J., Vincent, E., Lengaigne, M., Chauvin, F., 2011. Mesoscale simulation of tropical cyclones in the South Pacific: climatology and interannual variability. J. Clim. 24, 3–25.
Kettle, A.J., et al., 1999. A global database of sea surface dimethylsulfide (DMS) measurements and a procedure to predict sea surface DMS as a function of latitude, longitude, and month. Glob. Biogeochem. Cycles 13 (2), 399–444.
Kittaka, C., Winker, D.M., Vaughan, M.A., Omar, A., Remer, L.A., 2011. Intercomparison of column aerosol optical depths from CALIPSO and MODIS-Aqua. Atmos. Meas. Tech. 4, 131–141.
Koren, I., Feingold, G., Remer, L.A., 2010. The invigoration of deep convective clouds over the Atlantic: aerosol effect, meteorology or retrieval artifact? Atmos. Chem. Phys. 10, 8855–8872. http://dx.doi.org/10.5194/acp-10-8855-2010 (http://dx.doi.org/10.5194/acp-10-8855-2010).
Krotkov, N.A., Carn, S.A., Krueger, A.J., Bhartia, P.K., Yang, K., 2006. Band residual difference algorithm for retrieval of SO_2 from the Aura Ozone Monitoring Instrument (OMI). IEEE Trans. Geosci. Remote Sens. 44 (5), 1259–1266. http://dx.doi.org/10.1109/TGRS.2005.861932 (AURA Special Issue).
Lana, A., Bell, T.G., Simó, R., Vallina, S.M., Ballabrera-Poy, J., Kettle, A.J., Dachs, J., Bopp, L., Saltzman, E.S., Johnson, J.E., Liss, P.S., 2011. An updated climatology of surface dimethylsulfide concentrations and emission fluxes in the global ocean. Glob. Biogeochem. Cycles 25 GB 1004.
Langmann, B., Zakšek, K., Hort, M., Duggen, S., 2010. Volcanic ash as fertiliser for the surface Ocean. Atmos. Chem. Phys. 10, 3891–3899.
Lee, C., et al., 2011. SO_2 emissions and lifetimes: estimates from inverse modeling using in situ and global, space-based (SCHIMACHY and OMI) observations. J. Geophys. Res. 116, D06304. http://dx.doi.org/10.1029/2010JD014758.
Lefèvre, J., Marchesiello, P., Jourdain, N., Menkes, C., Leroy, A., 2010. Weather regimes and orographic circulation around New Caledonia. Mar. Pollut. Bull. http://dx.doi.org/10.1016/j.marpolbul.2010.06.012.
Levelt, P.F., Dobber, M.R., Mälkki, A., Visser, H., de Vries, J., Stammes, P., Lundell, J.O.V., Saari, H., 2006. The ozone monitoring instrument. IEEE Trans. Geosci. Remote Sens. 44, 1093–1101.
Li, J., Ma, X., von Salzen, K., Dobbie, S., 2008. Parameterization of sea-salt optical properties and physics of the associated radiative forcing. Atmos. Chem. Phys. 8, 4787–4798. http://dx.doi.org/10.5194/acp-8-4787-2008.
Liang, J., Jacobson, M.Z., 1999. A study of sulfur dioxide oxidation pathways over a range of liquid water contents, pHs, and temperatures. J. Geophys. Res. 104, 13,749–13,769.
Liang, Q., Stolarski, R.S., Kawa, S.R., Nielsen, J.E., Douglass, A.R., Rodriguez, J.M., Blake, D.R., Atlas, E.L., Ott, L.E., 2010. Finding the missing stratospheric Bry: a global modeling study of CHBr3 and CH2Br2. Atmos. Chem. Phys 10, 2269–2286. http://dx.doi.org/10.5194/acp-10-2269-2010.
Lin, Yuh-Lang, Farley, Richard D., Orville, Harold D., 1983. Bulk parameterization of the snow field in a cloud model. J. Clim. Appl. Meteorol. 22, 1065–1092.
Liss, P., Merlivat, L., 1986. The role of sea–air exchange in geochemical cycling. In: Menard, P. (Ed.), chapter Air–sea gas exchange rates: Introduction and synthesis. Reidel, Dordrecht, pp. 113–127.
Liu, H., Jacob, D.J., Bey, I., Yantosca, R.M., 2001. Constraints from 210Pb and 7Be on wet deposition and transport in a global three-dimensional chemical tracer model driven by assimilated meteorological fields. J. Geophys. Res. 106 (12), 12,109–12,128.
Liu, Z., Coauthors, 2009. The CALIPSO Lidar cloud and aerosol discrimination: version 2 algorithm and initial assessment of performance. J. Atmos. Ocean. Technol. 26, 1198–1213. http://dx.doi.org/10.1175/2009JTECHA1229.1.
Martin, R.V., Jacob, D.J., Yantosca, R.M., Chin, M., Ginoux, P., 2003. Global and regional decreases in tropospheric oxidants from photochemical effects of aerosols. J. Geophys. Res. 108, 4097. http://dx.doi.org/10.1029/2002JD002622.
Matthijsen, J., Suhre, K., Bechtold, P., Rosset, R., 1997. The effect of fractional cloudiness on the oxidation of SO_2. Tellus 49B, 343–356.
McCormick, B.T., Edmonds, M., Mather, T.A., Carn, S.A., 2012. First synoptic analysis of volcanic degassing in Papua New Guinea. Geochem. Geophys. Geosyst. 13, Q03008. http://dx.doi.org/10.1029/2011GC003945.
McGonigle, A.J.S., Oppenheimer, C., Tsanev, V.I., Saunders, S., Mulina, K., Tohui, S., Bosco, J., Nahou, J., Kuduon, J., Taranu, F., 2004. sulphur dioxide fluxes from Papua New Guinea's volcanoes. J. Geophys. Res. Lett. 31, L08606. http://dx.doi.org/10.1029/2004GL019568.
Mishchenko, M.I., Dlugach, J.M., Yanovitskij, E.G., Zakharova, N.T., 1999. Bidirectional reflectance of flat, optically thick particulate laters: an efficient radiative transfer solution and applications to snow and soil surfaces. *J. Quant. Spectrosc. Radiat. Transf.* 63, 409–432.
Monahan, E.C., Spiel, D.E., Davidson, K.L., 1986. A model of marine aerosol generation via whitecaps and wave disruption. In: Monahan, E., Niocaill, G.M., Reidel, Dordrecht (Eds.), Oceanic Whitecaps and their Role in Air–sea Exchange Processes, pp. 167–174 (The Netherlands).
Mulcahy, J.P., O'Dowd, C.D., Jennings, S.G., Ceburnis, D., 2008. Significant enhancement of aerosol optical depth in marine air under high wind conditions. J. Geophys. Res. Lett. 35, L16810. http://dx.doi.org/10.1029/2008GL034303.
Nakanashi, M., Niino, H., 2004. An improved Mellor-Yamada Level-3 model with condensation physics: its design and verification. Bound.-Layer Meteorol. 112, 1–31.
Nightingale, P.D., Malin, G., Law, C.S., Watson, A.J., Liss, P.S., Liddicoat, M.I., Boutin, J., Upstill-Goddard, R., 2000. In situ evaluation of air–sea gas exchange parameterizations using novel conservative and volatile tracers. Glob. Biogeochem. Cycles 14, 373–387.
O'Dowd, C., Scannell, C., Mulcahy, J., Jennings, S.G., 2010. Wind speed influences on marine aerosol optical depth. Adv. Meteorol. 2010. http://dx.doi.org/10.1155/2010/830846 (Article ID 830846, 7 pages).
Omar, A., Won, J., Winker, D., Yoon, S., Dubovik, O., McCormick, M., 2005. Development of global aerosol models using cluster analysis of Aerosol Robotic Network (AERONET) measurements. J. Geophys. Res. 110, D10S14.
Oo, M., Holz, R., 2011. Improving the CALIOP aerosol optical depth using combined MODIS-CALIOP observations and CALIOP integrated attenuated total color ratio. J. Geophys. Res. 116, D14201. http://dx.doi.org/10.1029/2010JD014894 (15~pp.).
Oppenheimer, C., Scaillet, B., Martin, R.S., 2011. Sulfur degassing from volcanoes: source conditions, surveillance, plume chemistry and impacts. Rev. Mineral. Geochem. 73, 363–421. http://dx.doi.org/10.2138/rmg.2011.73.13.
Park, S., Bretherton, C.S., 2009. The University of Washington shallow convection and moist turbulence schemes and their impact on climate simulations with the Community Atmosphere Model. J. Clim. 22, 3449–3469.
Pleim, J.E., 2011. Comment on "Simulation of surface ozone pollution in the Central Gulf Coast Region USING WRF/Chem model: sensitivity to PBL and land surface physics". Adv. Meteorol. 2011. http://dx.doi.org/10.1155/2011/464753 (Article ID 464753, 3 pages).
Pinardi, G., Campion, R., Van Roozendael, M., Fayt, C., Van Geffen, J., Galle, B., Carn, S., Valks, P., Rix, M., Hildago, S., Bourquin, J., Garzon, G., Inguaggiato, S., Sept. 2010. Comparison of volcanic SO_2 flux measurements from satellite and from the NOVAC network. Proceedings of the 2010 EUMETSAT Meteorological Satellite Conference. EUMETSAT publication, Córdoba, Spain, pp. 20–24.
Remer, L.A., Kaufman, Y.J., Tanre, D., Mattoo, S., Chu, D.A., Martins, J.V., Li, R.R., Ichoku, C., Levy, R.C., Kleidman, R.G., Eck, T.F., Vermote, E., Holben, B.N., 2005. The MODIS aerosol algorithm, products, and validation. J. Atmos. Sci. 62 (4), 947–973.
Remer, L.A., Tanré, D., Kaufman, Y.J., Levy, R., Mattoo, S., 2006. Algorithm for Remote Sensing of Tropospheric Aerosol from MODIS: Collection 005. National Aeronautics and Space Administration (http://modis-atmos.gsfc.nasa.gov/docs/MOD04:MYD04_ATBD_C005_rev1.pdf).
Roberts, T.J., Jourdain, L., Griffiths, P.T., Pirre, M., 2014. Re-evaluating the reactive uptake of HOBr in the troposphere with implications for the marine boundary layer and volcanic plumes. Atmos. Chem. Phys. Discuss. 14, 2717–2771. http://dx.doi.org/10.5194/acpd-14-2717-2014.
Robock, A., 2000. Volcanic eruptions and climate. Rev. Geophys. 38, 191–219.
Saide, P.E., Spak, S.N., Carmichael, G.R., Mena-Carrasco, M.A., Yang, Q., Howell, S., Leon, D.C., Snider, J.R., Bandy, A.R., Collett, J.L., Benedict, K.B., de Szoeke, S.P., Hawkins, L.N., Allen, G., Crawford, I., Crosier, J., Springston, S.R., 2012. Evaluating WRF-Chem aerosol indirect effects in Southeast Pacific marine stratocumulus during VOCALS-

REx. Atmos. Chem. Phys. 12, 3045–3064. http://dx.doi.org/10.5194/acp-12-3045-2012.
Savoie, D.L., Prospero, J.M., 1989. Comparison of oceanic and continental sources of non-seasalt sulphate over the Pacific Ocean. Nature 339, 685–687.
Savoie, D.L., Prospero, J.M., Saltzman, E.S., 1989. Non-seasalt sulfate and nitrate in tradewind aerosols at Barbados: evidence for long-range transport. J. Geophys. Res. 94, 5069–5080.
Savoie, D.L., Prospero, J.M., Arimoto, R., Duce, R.A., 1994. Non-seasalt sulfate and methanesulfonate at American Samoa. J. Geophys. Res. - Atmos. 99, 3587–3596.
Schmidt, A., Carslaw, K.S., Mann, G.W., Rap, A., Pringle, K.J., Spracklen, D.V., Wilson, M., Forster, P.M., 2012. Importance of tropospheric volcanic aerosol for indirect radiative forcing of climate. Atmos. Chem. Phys. 12, 7321–7339. http://dx.doi.org/10.5194/acp-12-7321-2012.
Shinozuka, Y., Clarke, A., Howell, S., Kapustin, V., Huebert, B., 2004. Sea-salt vertical profiles over the Southern and tropical Pacific oceans: microphysics, optical properties, spatial variability, and variations with wind speed. J. Geophys. Res. 109 (D24). http://dx.doi.org/10.1029/2004JD004975.
Schumacher, Courtney, Houze, Robert A., 2003. The TRMM precipitation radar's view of shallow, isolated rain. J. Appl. Meteorol. 42, 1519–1524.
Singh, H.B., et al., 2000. Biomass burning influences on the composition of the remote South Pacific troposphere: analysis based on observations from PEM-Tropics-A. Atmos. Environ. 34, 635–644.
Sinyuk, A., Torres, O., Dubovik, O., 2003. Combined use of satellite and surface observations to infer the imaginary part of the refractive index of Saharan dust. Geophys. Res. Lett. 30 (2), 1081.
Skamarock, W.C., Klemp, J.B., Dudhia, J., Gill, D.O., Barker, D.M., Duda, M., Huang, X.-Y., Wang, W., Powers, J.G., 2008. A Description of the Advanced Research WRF Version 3. NCAR Technical note NCAR/TN-475+STR, June 2008.
Song, X., Zhang, G.J., 2009. Convection parameterization, tropical Pacific double ITCZ, and upper ocean biases in the NCAR CCSM3. Part I: Climatology and atmospheric feedback. J. Clim. 22, 4299–4315.
Spinei, E., Carn, S.A., Krotkov, N.A., Mount, G.H., Yang, K., Krueger, A., 2010. Validation of ozone monitoring instrument SO_2 measurements in the Okmok volcanic cloud over Pullman, WA, July 2008. J. Geophys. Res. 115, D00L08. http://dx.doi.org/10.1029/2009JD013492.
Stuefer, M., Freitas, S.R., Grell, G., Webley, P., Peckham, S., McKeen, S.A., 2012. Inclusion of Ash and SO_2 emissions from volcanic eruptions in WRF-CHEM: development and some applications. Geosci. Model Dev. Discuss. 5, 2571–2597. http://dx.doi.org/10.5194/gmdd-5-2571-2012.
Takemura, T., Nozawa, T., Emori, S., Nakajima, T.Y., Nakajima, T., 2005. Simulation of climate response to aerosol direct and indirect effects with aerosol transport-radiation model. J. Geophys. Res. 110, D02202. http://dx.doi.org/10.1029/2004JD005029.
Textor, et al., 2006. Analysis and quantification of the diversities of aerosol life cycles within AeroCom. Atmos. Chem. Phys. 6, 1777–1813.
Textor, et al., 2007. The effect of harmonized emissions on aerosol properties in global models an AeroCom experiment. Atmos. Chem. Phys. 7, 4489–4501.
Torres, O., Tanskanen, A., Veihelman, B., Ahn, C., Braak, R., Bhartia, P.K., Veefkind, P., Levelt, P., 2007. Aerosols and surface UV products from OMI observations: an overview. J. Geophys. Res. 112, D24S47. http://dx.doi.org/10.1029/2007JD008809.
Trenberth, K.E., 1998. Atmospheric moisture residence times and cycling: implications for rainfall rates and climate change. Clim. Chang. 39, 667–694.
Trivitayanurak, W., Palmer, P.I., Barkley, M.P., Robinson, N.H., Coe, H., Oram, D.E., 2012. The composition and variability of atmospheric aerosol over Southeast Asia during 2008. Atmos. Chem. Phys. 12, 1083–1100.
Twomey, S., 1977. The influence of pollution on the shortwave albedo of clouds. J. Atmos. Sci. 34, 1149–1152.
Vance, A., McGonigle, A.J.S., Aiuppa, A., Stith, J.L., Turnbull, K., von Glasow, R., 2010. Ozone depletion in tropospheric volcanic plumes. Geophys. Res. Lett. 37, L22802.
Vernier, J.-P., et al., 2011. Major influence of tropical volcanic eruptions on the stratospheric aerosol layer during the last decade. Geophys. Res. Lett. 38, L12807.
Vincent, E.M., Lengaigne, M., Menkes, C.E., Jourdain, N., Marchesiello, P., Madec, G., 2011. : interannual variability of the South Pacific Convergence Zone and implications for Tropical Cyclone genesis. Clim. Dyn. 36 (9), 1881–1896.
von Glasow, R., von Kuhlmann, R., Lawrence, M.G., Platt, U., Crutzen, P.J., 2004. Impact of reactive bromine chemistry in the troposphere. Atmos. Chem. Phys. 4, 2481–2497.
von Glasow, R., 2010. Atmospheric chemistry in volcanic plumes. Proc. Natl. Acad. Sci. U. S. A. 107, 6594–6599.
Wang, H., Skamarock, W.C., Feingold, G., 2009. Evaluation of scalar advection schemes in the Advanced Research WRF model using large-eddy simulations of aerosol–cloud interactions. Mon. Weather Rev. 137, 2547–2558.
Winker, D.M., Vaughan, M.A., Omar, A.H., Hu, Y., Powell, K.A., Liu, Z., Hunt, W.H., Young, S.A., 2009. Overview of the CALIPSO mission and CALIOP data processing algorithms. J. Atmos. Ocean. Technol. 26, 2310–2323. http://dx.doi.org/10.1175/2009JTECHA1281.1.
Yuan, T., Remer, L.A., Yu, H., 2011. Microphysical, macrophysical and radiative signatures of volcanic aerosols in trade wind cumulus observed by the A-Train. Atmos. Chem. Phys. 11, 7119–7132. http://dx.doi.org/10.5194/acp-11-7119-2011.
Xu, K.-M., Randall, D.A., 1996. A semi-empirical cloudiness parameterization for use in climate models. J. Atmos. Sci. 53, 3084–3102.
Yu, H., Chin, M., Winker, D.M., Omar, A.H., Liu, Z., Kittaka, C., Diehl, T., 2010. Global view of aerosol vertical distributions from CALIPSO lidar measurements and GOCART simulations: regional and seasonal variations. J. Geophys. Res. 115, D00H30. http://dx.doi.org/10.1029/2009JD013364.
Zhang, G.J., McFarlane, N.A., 1995. Sensitivity of climate simulations to the parameterization of cumulus convection in the Canadian Climate Centre general circulation model. Atmos. Ocean 33, 407–446.
Zhao, C., Liu, X., Leung, L.Y.R., Johnson, B., McFarlane, S.A., Gustafson Jr., W.I., Fast, J.D., Easter Jr., R.C., 2010. The spatial distribution of mineral dust and its shortwave radiative forcing over North Africa: modeling sensitivities to dust emissions and aerosol size treatments. Atmos. Chem. Phys. 10 (18), 8821–8838. http://dx.doi.org/10.5194/acp-10-8821-2010.